Vertically aligned $Gd_2O_2SO_4$:Ln and Gd_2O_2S:Ln luminescent films with super-hydrophobicity via a novel precursor route (Ln = Pr, Eu, Tb)

Fan Li[a], Minghui Jin[a], Zhuowei Li[a], Xuejiao Wang[b], Qi Zhu[a], Ji-Guang Li[c,*]

[a]Key Laboratory for Anisotropy and Texture of Materials (Ministry of Education) and School of Materials Science and Engineering, Shenyang, Liaoning, 110819, China

[b]College of Chemistry and Materials Engineering, Bohai University, Jinzhou, Liaoning 121007, China

[c]Research Center for Functional Materials, National Institute for Materials Science, Tsukuba, Ibaraki, 305-0044, Japan

[*]Corresponding author

Dr. Ji-Guang Li

National Institute for Materials Science

Tel: +81-29-860-4394

E-mail: li.jiguang@nims.go.jp

Abstract

Pr^{3+}, Eu^{3+} and Tb^{3+} activated Gd_2O_2S (Gd_2O_2S:Ln), either in the powder or ceramic form, are well known for their wide applications in photoluminescence (PL), cathodoluminescence (CL) and X-ray excited luminescence (XEL) due to high efficiency. The film form of Gd_2O_2S:Ln, however, has not been reported up to date to the best of our knowledge. By hydrothermally reacting $Gd(NO_3)_3$, $(NH_4)_2SO_4$ and urea, this work produced a $Gd_2(OH)_2CO_3SO_4 \cdot H_2O$ new compound (GOCSH) that was crystallized in the tetragonal system (space group *P*-42_1m) with a layered structure along the [001] crystallographic direction. Furthermore, macroscopically and microscopically uniform GOSCH:Ln films, constructed by vertical self-alignment of platelike crystallites, were successfully fabricated by applying heterogenous nucleation on quartz substrate. Taking the advantage of the exactly the same S/(Gd,Ln) molar ratio, $Gd_2O_2SO_4$:Ln and Gd_2O_2S:Ln films of the same microstructures were then derived from the GOSCH:Ln films by annealing in air and hydrogen at 800 °C, respectively, without any additional sulfurization. The mechanism of film formation and the influence of deposition/annealing temperature on film quality were discussed. Aside from luminescence, the films all have microstructure-enabled super-hydrophobicity and are transparent in the visible light region (~70-93%). The multi-functional films, particularly those of Gd_2O_2S:Ln, may find potential application in luminescence, display, scintillation and microimaging.

Keywords: Oriented film; Precursor; Gd_2O_2S; Luminescence; Super-hydrophobicity

1. Introduction

The phosphors developed by doping Gd_2O_2S with Pr^{3+}, Eu^{3+} and Tb^{3+} (Gd_2O_2S:Ln) are well known for their bright green, red and green emissions, respectively, and are finding wide applications in photoluminescence (PL), cathodoluminescence (CL) and X-ray excited luminescence (XEL), because Gd_2O_2S has the advantage of wide bandgap (~4.6-4.8 eV), high radiation harness (theoretical density ~7.34 g/cm^3), low phonon energy (~520 cm^{-1}), satisfactory stability and efficient excitation absorption [1, 2]. The most matured and commercialized technology to synthesize Gd_2O_2S:Ln and other rare-earth (RE) oxysulfides (RE_2O_2S) is flux reaction, which involves reacting an RE oxide/carbonate with elemental sulfur/sodium thiosulfate ($Na_2S_2O_3$) in an alkali carbonate/halide flux at 1200-1300 ºC for several hours, followed by acid washing [3]. The technique has the advantage of well crystallized particles (micron level) but raises environmental concern because of its toxic byproducts (such as H_2S and SO_x gases). Because of the high melting point of Gd_2O_2S (~2200 ºC) and the large particle size/low activity of the powder, the fabrication of Gd_2O_2S:Ln ceramic scintillator, which is being widely applied for X-ray computed tomography (X-CT), requires harsh sintering conditions, such as a temperature as high as ~1750 ºC for atmosphere-controlled sintering and typically ~1300-1500 ºC and meanwhile tens to hundreds MPa of an applied pressure for pressure assisted sintering [4, 5]. Sulfidizing a precursor with H_2S or CS_2 gas [6, 7] or combustion with thiourea as the sulfur source [8] may produce nanocrystalline RE_2O_2S, but is difficult to control over phase/chemical purity since sulfur is much less affinitive than oxygen toward RE. Aside from three-dimensional bulks, thin-film scintillators are drawing remarkable attention over the recent years for device miniaturization and for X-ray or electron microimaging with high spatial sub-micrometer resolution [9-11].

Up to date, thin-film scintillators have been successfully fabricated by gas phase condensation and/or liquid phase epitaxy in moten salt for CsI:Tl and Ln^{3+} (Ln = Ce, Pr, Eu, Tb) activated RE_2O_3 sesquioxide, $REAlO_3$ perovskite, $RE_3Al_5O_{12}$ garnet and RE_2SiO_5 orthorsilicate, where RE^{3+} is typical of Y^{3+}, Gd^{3+} or Lu^{3+} [9-11]. Our thorough literature survey, however, indicated that Gd_2O_2S:Ln has not been prepared in the thin-film form due to its special composition. Pulsed laser deposition (PLD), for example, was attempted for Gd_2O_2S deposition, but the film product contained an oxide impurity [12].

The recent appearance of $RE_2(OH)_4SO_4{\cdot}nH_2O$ layered hydroxide (SO_4^{2-}-LREH; RE = La-Lu lanthanide or Y) provided a unique opportunity for wide-spectrum green synthesis of RE_2O_2S [13, 14]. This is because the compound is readily obtainable by titrating an aqueous solution containing RE^{3+} and SO_4^{2-} with ammonium hydroxide to a certain pH value followed by hydrothermal crystallization, and the compound directly dehydrates to RE_2O_2S upon being heated in a reducing atmosphere such as hydrogen ($RE_2(OH)_4SO_4{\cdot}nH_2O + 4H_2 \rightarrow RE_2O_2S + (6+n)H_2O$) [13, 14]. Such a technical route, unfortunately, cannot be directly applied to film fabrication since titration, like most other precipitation reactions, is featured by localized fast nucleation of the solid phase in an uncontrollable manner, and one cannot confine nucleation to a designated place such as the substrate for film growth. Nevertheless, it is well documented in the literature that employing an ion-reservoir is effective for nucleation control, where the reservoir releases the precipitation-participating cation or anion in a controllable way under a certain condition such as heating [15, 16]. One classic example of great success is the urea-based homogeneous precipitation of amorphous $RE(OH)CO_3{\cdot}nH_2O$, where the OH^- and CO_3^{2-} anions were released by the *in situ* hydrolysis of urea above ~83 °C [17, 18]. The slow supply of anions allows spontaneous nucleation to occur via one-single burst in the

whole reaction system, and $RE(OH)CO_3{\cdot}nH_2O$ monospheres can then be generated via subsequent uniform growth of the nuclei [15, 19].

In view of the above, we conducted hydrothermal reaction for the $Gd(NO)_3$-$(NH_4)_2SO_4$-urea ternary system in this work, and obtained a $Gd_2(OH)_2CO_3SO_4{\cdot}nH_2O$ new compound (GOCSH) with chemical composition midway between those of the aforesaid $RE_2(OH)_4SO_4{\cdot}nH_2O$ (SO_4^{2-}-LREH) and $RE(OH)CO_3{\cdot}nH_2O$ (that is, $RE_2(OH)_2(CO_3)_2{\cdot}2nH_2O$). Preliminary analysis of crystal structure indicated that the compound was crystallized in the tetragonal system (space group *P*-42$_1$*m*) with a layered structure along the [001] crystallographic direction. More importantly, macro-/microscopically uniform GOSCH:Ln films consisting of vertically aligned platelike crystallites were successfully obtained by applying heterogenous nucleation on quartz substrate, which were then transformed into $Gd_2O_2SO_4$:Ln and Gd_2O_2S:Ln films of the same microstructure by subsequent annealing in air and hydrogen, respectively. The spectral features of the doped Ln ions were analyzed in detail, and further investigation found that all the films have microstructure-enabled super-hydrophobicity (water contact angle above 150°) and are transparent in the visible light region (~70-93%). The multi-functional films, especially those of Gd_2O_2S:Ln, were expected to have potential application for luminescence, display, scintillation and microimaging. In the following sections, we report the detailed synthesis and characterization of the materials.

2. Experimental Section

2.1. Reactants and synthesis

The 99.99% pure RE oxides of Pr_6O_{11}, Eu_2O_3, Gd_2O_3 and Tb_4O_7 were provided by Huizhou Ruier Rare-Chem. Hi-Tech. Co. Ltd (Huizhou, China), and analytical grade ammonium

sulfate ($(NH_4)_2SO_4$), urea ($CO(NH_2)_2$) and nitric acid (HNO_3, 65-68 wt%) were purchased from Sinopharm Chemical Reagent Co. Ltd (Shanghai, China). Ultrapure water (resistivity > 18 MΩ·cm) was used throughout the experiments. The nitrate solution of RE^{3+} was prepared by dissolving the corresponding oxide with a proper amount of nitric acid, followed by dilution.

For the synthesis of precursor powder, an aqueous solution (60 mL) containing 3 mmol of Gd^{3+}, 2 mmol of $(NH_4)_2SO_4$ and 2 mmol of $CO(NH_2)_2$ was transferred into a Teflon-lined stainless steel autoclave of 100 mL capacity, followed by hydrothermal reaction at 140 °C for 12 h in a preheated electric oven. After natural cooling to room temperature, the precipitate was collected via centrifugation, washed with water 3 times and ethanol twice, and then dried at 60 °C for 12 h. For the preparation of precursor films, the aforesaid solution was preheated at ~85 °C until pH reached ~5.8 before hydrothermal treatment. Such an operation was found vital to the growth of a uniform film, as it may allow the precipitation-participating OH^- and CO_3^{2-} anions, released via the hydrolysis of urea, to accumulate to a critical concentration level for fast heterogeneous nucleation. The quartz substrate (2.5 cm×7.5 cm×0.1 cm) for film growth was ultrasonically cleaned with water and ethanol for 5 min sequentially, dried with blowing air, and was then immersed into the pretreated reactant solution at an inclination angle of ~65° in the autoclave. After hydrothermal reaction at a predetermined temperature for 12 h, the substrate was taken out of the autoclave, washed with water and ethanol in turn, and then dried with blowing air. The precursor films separately doped with 1 at.% of Pr^{3+}, 5 at.% of Eu^{3+} and 2 at.% of Tb^{3+} were produced by the above procedures, where the doping levels were taken according to previous reports [6, 20, 21]. $Gd_2O_2SO_4$:Ln films (Ln = Pr, Eu, Tb) were derived by annealing their precursor films in stagnant air at 800 °C for 1 h, and

Gd_2O_2S:Ln films were obtained by annealing the above $Gd_2O_2SO_4$:Ln films in flowing H_2 (100 mL/min) at 800 °C for another 1 h. In both the cases, a heating rate of 8 °C/min was used for the ramp stage of heating.

2.2. Characterization

The elemental contents of the precursor powder were determined for Gd via inductively coupled plasma (ICP) mass spectrometry (detection limit 0.01wt%; Model iCAP Q, Thermo Fisher Scientific, Waltham, USA) and for N, C and S via the inert gas fusion-infrared absorption/thermal conductivity technique (detection limit 0.01wt%; Elementar varioEL cube, Langenselbold, Germany), and the powder for analysis was pre-dried at 60 °C for 24 h. Phase identification was performed via X-ray diffractometry (XRD, Bragg measurement; SmartLab, Rigaku, Tokyo, Japan) using nickel-filtered Cu-Kα radiation (λ= 0.15406 nm) under 40 kV/200 mA, a Model D/teX Ultra line detector and a scanning speed of 4° 2θ/min. The XRD data (Bragg measurement) for structure analysis with TOPAS 4.2 software were collected from powder sample with the above equipment via step-scan over the 2θ range of 5-110°, using a step width of 0.02° and a counting time of 10 s per step. Fourier transform infrared spectroscopy (FTIR, Nicolet iS5, Thermo Fisher Scientific) was conducted using the standard KBr pellet method. Product morphology and microstructure were analyzed by field-emission scanning electron microscopy (FE-SEM, Model JSM-7001F, JEOL, Tokyo) under an acceleration voltage of 15 kV and transmission electron microscopy (TEM, Model JEM-2000FX, JEOL) under 200 kV. Thermogravimetry/differential thermal analysis (TG/DTA, Model SETSYS Evolution-16, Setaram, France) was performed at a constant heating rate of 10 °C/min in flowing simulated air (50 mL/min). Surface wettability of the films was measured on an automatic contact angle goniometer (Model SL200B, KINO, New

York, USA) at ambient temperature. The transmittance spectra of the films were recorded on a Model UV-3600 Plus instrument (Shimadzu, Kyoto, Japan) equipped with a Φ150 mm integrating sphere. Photoluminescence was analyzed with an FP-8600 fluorospectrophotometer (JASCO, Tokyo) equipped with a Φ60 mm integrating sphere (Model ISF-834, JASCO), a 150 W xenon lamp for excitation, a slit width of 5 nm and a scan speed of 100 nm/min for both excitation and emission. The spectral response of the spectrophotometer was corrected with a Rhodamine-B solution (5.5 $g \cdot L^{-1}$ in ethylene glycol) and a standard light source unit (ECS-333, JASCO) for the ranges of 220-600 nm and 350-850 nm, respectively. The fluorescence decay of Eu^{3+} and Tb^{3+} was analyzed with the FP-8600 instrument, while that of Pr^{3+} was measured with a DeltaFlex modular fluorescence lifetime system (HORIBA Scientific, Jobin Yvon IBH Ltd., Scotland) using NanoLED-250 (λ = 249 nm, 1.2 ns pulse duration) for excitation.

3. Results and discussion

3.1 Characterization of the precursor powder

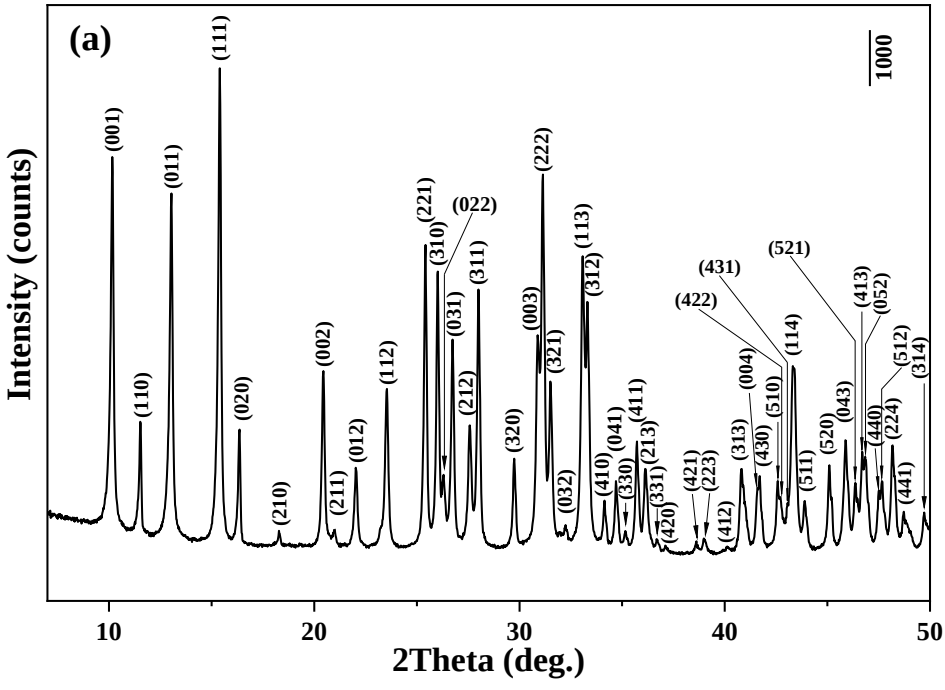

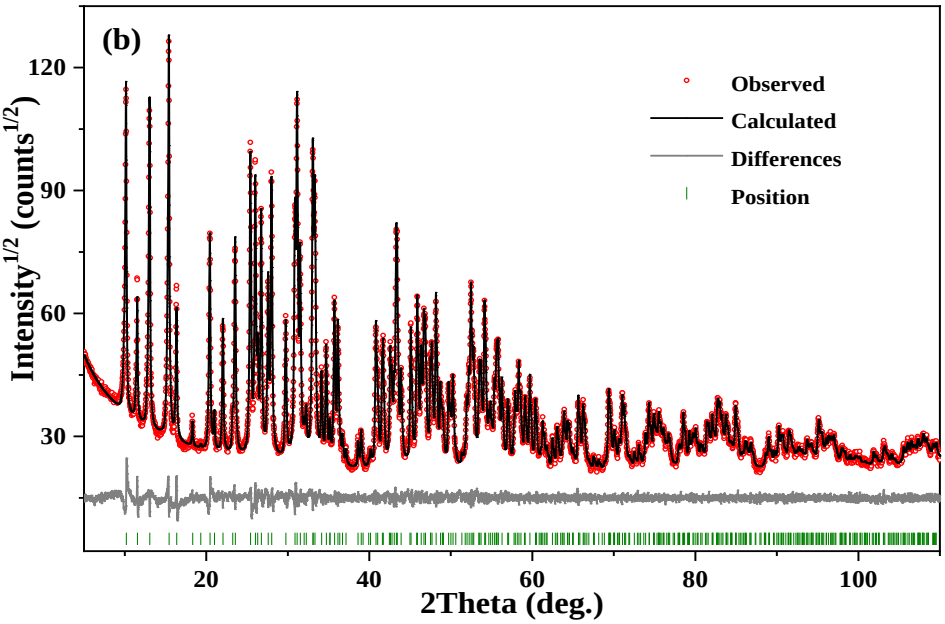

Fig. 1. Indexation of the XRD pattern of precursor powder for 2θ = 5-50° (a) and the results of Pawley refinement of the XRD pattern (b).

XRD analysis indicated that the precursor powder is highly crystalline, as evidenced by the sharp reflections in Fig. 1. Our careful survey, however, showed that the XRD pattern cannot be indexed with any of the Gd-containing compounds in the JCPDS database or literature. FTIR analysis was thus conducted to understand the chemical species contained in this powder, and the results (Fig. 2a) clearly revealed the vibrations arising from OH^- at ~3553 cm^{-1} (O–H stretching, ν_1) [22], from H_2O molecules at ~3420 cm^{-1} (O–H stretching, ν_1)/1645 cm^{-1} (H–O–H bending, ν_2) [22, 23], from CO_3^{2-} at ~840 cm^{-1} (ν_2, weak) and in the regions of ~1390-1590 cm^{-1} (ν_3, strong)/670-808 cm^{-1} (ν_4, medium strong) [22, 24], and from SO_4^{2-} at ~1010 cm^{-1} (ν_1) and in the regions of ~1025-1270 cm^{-1} (ν_3)/583-645 cm^{-1} (ν_4) [22]. With the results of FTIR and in view that the reaction system also contains NH_4^+ (from ammonium sulfate and urea) and NO_3^- (from Gd nitrate), we performed chemical analysis for the Gd, C, S and N key elements and found that the powder contains ~60.82 (±0.01) wt % of Gd, 2.29 (±0.01) wt % of C, 6.20 (±0.01) wt % of S and none of N, which correspond to a Gd:C:S

molar ratio of 2.00:1.01:1.00. The absence of N rules out the potential interference of NO_3^- or NH_4^+ with our assignment of the ν_3 vibration of CO_3^{2-} (~1390-1590 cm^{-1}). Based on the results of chemical analysis and by considering molecular neutrality, the product can thus be deduced to be $Gd_2(OH)_2CO_3SO_4 \cdot nH_2O$, where the number of molecular water (*n* value) was calculated from the formula with the content of Gd to be ~1.0. FE-SEM observation showed that the powder mainly contains hollow spheroids (~3-10 μm in diameter) of interlaced flakes (Fig. 2b), and a closer view (Fig. 2b, the inset) indicated that the edge length of each flake is close to ~2 micrometers while the thickness is a few tens of nanometers.

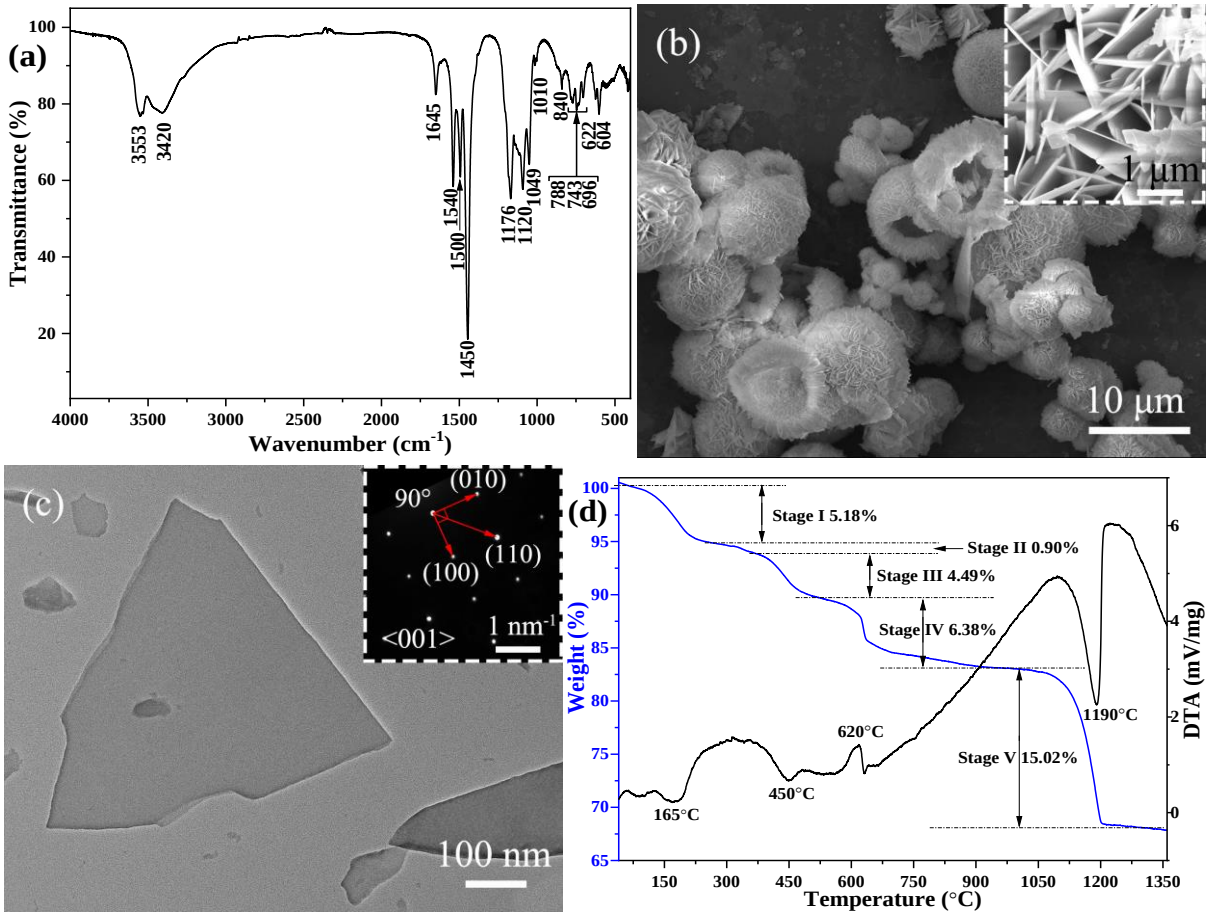

Fig. 2. FTIR spectrum (a), FE-SEM morphology (b), TEM morphology (c) and TG/DTA curves (d) of the precursor powder. The inset in (b) is a closer view and that in (c) is the SAED pattern.

The above results of composition and morphology analysis let us recall the $RE_2(OH)_4SO_4 \cdot nH_2O$ layered hydroxide (SO_4^{2-}-LREH, *n*~0-2.0) reported in recent years [14,

25]. This is because the chemical formula of SO_4^{2-}-LREH can be transformed to the formula of this work if two out of the four OH^- were replaced with one CO_3^{2-}, and the SO_4^{2-}-LREH also tends to crystallize as platelike crystals owing to its layered structure. Furthermore, the XRD pattern in Fig. 1 showed diffractions with *d*-spacing values of ~0.870 nm (2θ ~10.19°) and 0.435 nm (one half of 0.870 nm, 2θ ~20.40°) in the low-angle region. It was thus speculated that the product of this work is a phase-pure compound of layered crystal structure. We used multiple algorithms, including ITO [26], DICVOL [27] and TREOR [28], to index a preliminary cell, and the results all showed that the tetragonal cell with approximate dimensions of a = 10.8211 Å and c = 8.6812 Å has the highest credibility. When indexing the XRD pattern with this cell, all of the diffraction peaks can be well corresponded (Fig. 1a, Table S1). The systematic appearance of 00l diffractions further verified that this $Gd_2(OH)_2CO_3SO_4{\cdot}H_2O$ (GOCSH) new compound indeed has a layered crystal structure, which is built up via repetitive stacking along the [001] crystallographic direction. The Pawley refinement was carried out with potential space groups through TOPAS 4.2 software [29], among which the $P\text{-}42_1m$ (No. 113) one showed the highest degree of fit (Fig. 1b, Table 1). Selected area electron diffraction (SAED) from an individual platelike object, disintegrated from the hollow spheres (Fig. 2b) via ultrasonication, yielded a set of well-arranged spots (Fig. 2c and the inset), where the measured *d* spacings of ~5.43/5.44 and 7.67 Å can be assigned to (010)/(100) and (110) planes according to the results of theoretical analysis of the XRD pattern (Table S1), respectively. Furthermore, the (010)/(100) dihedral angle was measured from the SAED pattern to be ~90°, in compliance with the tetragonal structure determined for GOCSH. The results thus indicate that each of the microplates found

via SEM (Fig. 2b) and TEM (Fig. 2c) is single crystalline and was developed by 2D growth perpendicular to the [001] direction (*c*-axis). The layered crystal structure of SO_4^{2-}-LREH presents repetition of the hydroxide main layer, constructed by REO_9 polyhedrons, and interlayer SO_4^{2-} along the [001] direction [30]. While we speculated that the CO_3^{2-} and SO_4^{2-} anions of $Gd_2(OH)_2CO_3SO_4 \cdot H_2O$ assume a similar manner of occurrence, the determination of coordination sphere, atomic position and atomic occupancy is yet underway with the XRD data acquired via synchrotron irradiation.

Table 1. The Results of structure refinement for the $Gd_2(OH)_2CO_3SO_4 \cdot H_2O$ compound.

crystal system	tetragonal
space group	*P*-42$_1$*m*
lattice constant $a = b$ (Å)	10.8153(1)
lattice constant c (Å)	8.6762(1)
cell volume V (Å^3)	1014.8613(3)
R_{wp} (%)	5.05
R_{exp} (%)	2.66
R_p (%)	3.73
χ^2	1.90
R_B (%)	0.26

In Table 1, R_{wp}, R_{exp}, R_p, R_B and χ^2 (defined as R_{wp}/R_{exp}) denote weighted profile reliability factor, expected reliability factor; pattern reliability factor, Bragg reliability factor and goodness of fitting factor of the Rietveld structure refinement, respectively.

The thermal behavior of GOCSH was studied via TG/DTA, and the results are shown in Fig. 2d. It is seen that thermal decomposition proceeds via five distinct stages with a total weight of ~32 wt%, which is very close to the value (~31 wt%) calculated from the $Gd_2(OH)_2CO_3SO_4 \cdot H_2O$ formula. The first stage (Stage I, up to ~260 °C), with an endotherm at ~165 °C, should be caused by the removal of adsorbed/hydration water [25]. Stage Ⅱ to Stage Ⅳ (~260-1000 °C) exhibited a behavior very similar to the sequential and stepwise removal of OH^- and CO_3^{2-} from $Gd(OH)CO_3$ [31]. Stage Ⅴ (~1000-1200 °C), on the other

hand, well corresponds to the desulfuration of $Gd_2O_2SO_4$ to form Gd_2O_3 according to the thermal behavior of SO_4^{2-}-LGdH [32]. To better understand the course of thermal decomposition/phase evolution, XRD (Fig. S1a) and FTIR (Fig. S1b) analyses were conducted on the powders calcined at some typical temperatures determined according to the TG curve. It is seen that the 335 °C product has the same XRD pattern of GOCSH (Fig. S1a) but obviously reduced intensity of OH^- vibration (Fig. S1b), which implies that either dehydration (Stage I, Fig. 2d) or partial dehydroxylation (Stage Ⅱ, Fig. 2d) did not alter the crystal structure to a large extent. A similar phenomenon was also observed for $NH_4Y(MoO_4)_2{\cdot}2H_2O$ [33] and $NaLu(WO_4)_2{\cdot}2H_2O$ [34], and suggests that the water molecules of GOCSH reside at the outer layer of the coordination sphere and are only loosely accommodated. When the temperature reached 450 °C, OH^- absorption and the ν_4 vibration of CO_3^{2-} disappeared while the triple-split ν_3 vibration of CO_3^{2-} became a two-split state. This indicates that the Stage Ⅲ of weight loss corresponds to a synchronous removal of residual OH^- and a part of CO_3^{2-} (endotherm at ~450 °C) and is in line with the decomposition process of most hydroxyl carbonates [31, 35, 36]. It is also due to the dehydroxylation and partial decarbonation that the initial structure of GOCSH collapsed and an amorphous phase was resulted at 450 °C (Fig. S1a). The 620 °C product hardly showed the characteristic vibration of CO_3^{2-}, indicating that stage Ⅳ mainly corresponds to the removal of residual CO_3^{2-}. Meanwhile, each of the ν_3 and ν_4 vibrations of SO_4^{2-} was split into three separate peaks, which is typical of SO_4^{2-} chelating as a trans-bidentate ligand as in $RE_2O_2SO_4$ [25]. This conforms to the crystallization of $Gd_2O_2SO_4$ (exotherm at ~620 °C), as revealed by the corresponding XRD pattern (Fig. S1a). The 1190 °C product only showed Gd–O vibration at

~548 cm^{-1} [22], conforming to desulfuration in Stage V (endotherm at ~1190 °C) and the crystallization of cubic Gd_2O_3 (Fig. S1a). From the above discussion and the weight loss observed for each stage (Fig. 2d), the procedure of GOCSH decomposition can be detailed as follows: (1) $Gd_2(OH)_2CO_3SO_4{\cdot}H_2O \rightarrow Gd_2(OH)_2CO_3SO_4 + H_2O$ (Stage I, up to ~260 °C); (2) $Gd_2(OH)_2CO_3SO_4 \rightarrow Gd_2O_{0.14}(OH)_{1.72}CO_3SO_4 + 0.14H_2O$ (Stage II, ~260-370 °C); (3) $Gd_2O_{0.14}(OH)_{1.72}CO_3SO_4 \rightarrow Gd_2O_{1.25}(CO_3)_{0.75}SO_4 + 0.86H_2O + 0.25CO_2$ (Stage III; ~370-530 °C); (4) $Gd_2O_{1.25}(CO_3)_{0.75}SO_4 \rightarrow Gd_2O_2SO_4 + 0.75CO_2$ (Stage IV; ~530-1000 °C); (5) $Gd_2O_2SO_4 \rightarrow Gd_2O_3 + SO_3$ (Stage V; above 1000 °C). Noteworthy from Fig. S1a is that $Gd_2O_2SO_4$ can be transformed from GOCSH in a wide range of temperature (~620-900 °C), which makes it possible to controllably derive Gd_2O_2S by further annealing in hydrogen.

3.2 Characterization of the precursor films

Fig. 3a shows the XRD patterns of the GOCSH and GOCSH:Ln films formed via 12 h of deposition at 110 °C, with that of the GOCSH powder included for comparison. It is seen that the diffraction patterns conform well to that of the GOCSH powder in each case and the doped Ln^{3+} ions did not affect phase purity. Compared with the powder product, however, the films all showed significantly stronger (110) and (020) diffractions relative to the (001) one. This implies that the films similarly have a preferred orientation, which allowed the (110) and (020) planes to be significantly more exposed to the incident X-ray. In view that both (110) and (020) are perpendicular to (001) in the tetragonal structure of GOCSH, it can thus be concluded that the [001] crystallographic direction of the GOCSH crystallites is parallel to the surface of the quartz substrate. It is interesting to note that such an orientation is just opposite to that of the films self-assembled from the platelike crystallites of $RE_2(OH)_5A{\cdot}nH_2O$ layered

hydroxide (A^--LREH; A^- = NO_3^- or Cl^-) or the nanosheets exfoliated from A^--LREH crystallites, where the objects are lying flat on the substrate and have strong [001] orientation [37-39].

FE-SEM observation indicates that all the film products of Fig. 3a are almost identical in morphology and, therefore, that of GOCSH is shown in Fig. 3b for example. It is evident that the film has a porous and macroscopically uniform microstructure formed by interlacing of vertically aligned GOCSH platelets, in agreement with the crystallite orientation predicted from the XRD patterns (Fig. 3a). Observation under higher magnification (Fig. 3b, the inset) found that the mean edge length and thickness of the flakes are ~2.0 μm and ~170 nm, respectively, and the pore size of the porous structure is up to ~1 μm (average size ~ 0.7 μm). Cross-sectional observation of the film (Fig. 3c) intuitively showed vertical growth of the GOCSH flakes and a film thickness of ~2 μm.

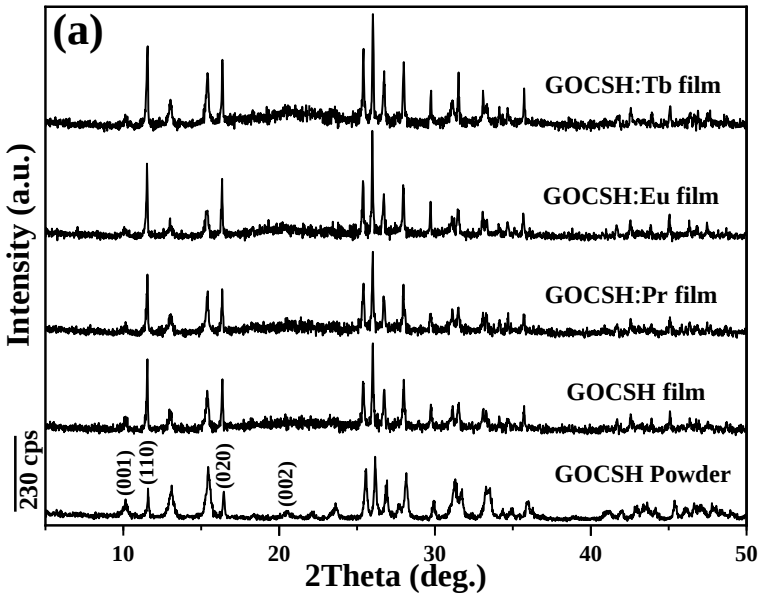

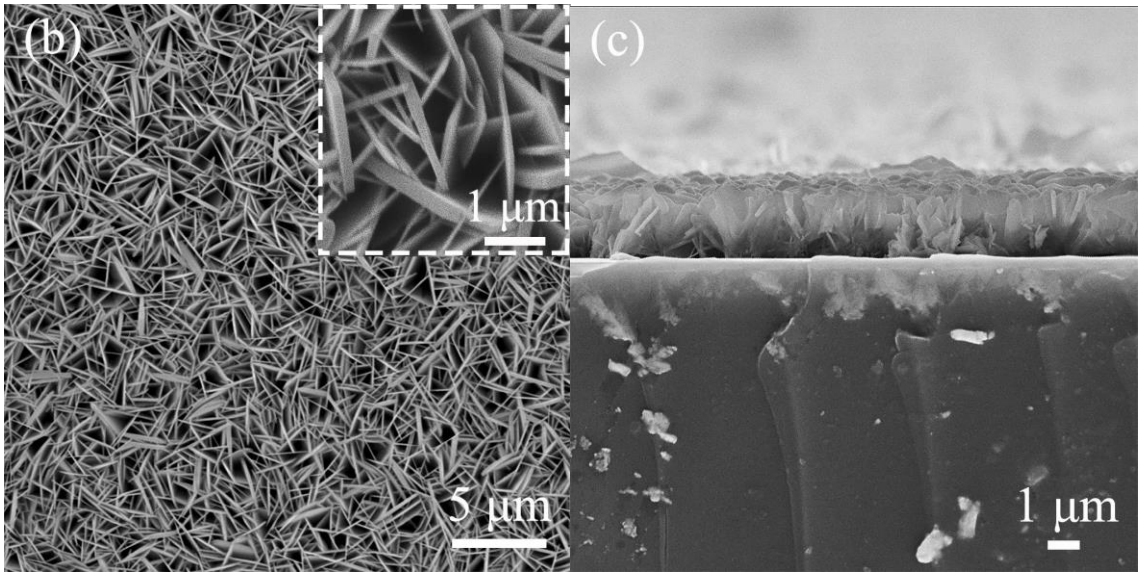

Fig. 3. XRD patterns of the precursor films deposited at 110 °C, with that of the GOCSH powder included for comparison (a), and FE-SEM morphologies of the GOCSH film observed from the surface (b) and cross section (c). The inset in (b) is a closer view.

To understand the mechanism of film formation, we tracked the time-course morphology development of the GOCSH film via FE-SEM and found a typical process of heterogeneous nucleation and crystallite growth (Fig. 4a-d). After only 30 min of reaction, the surface of the substrate has been sparsely distributed with flower-like clusters of GOCSH flakes (Fig. 4a). The rapid formation of such clusters may be explained by considering that heterogeneous nucleation at the high-energy site provided by the substrate would make the surrounding environment also be in a high-energy state for further nucleation due to the creation of a new interface. As a consequence, nucleation continues at around each of the formed nuclei, leading to the formation of a cluster. The increasing number of clusters and increasing size of the existing clusters with prolongation of the deposition reaction would eventually cause the adjacent clusters to merge, and thus a film covering the whole substrate surface was formed (Fig. 4b-d). The vertical growth of GOCSH flakes (Fig. 3b) is primarily driven by two factors. One is minimization of surface free energy. The (001) crystal plane of GOCSH, where Gd is

accommodated, has the lowest surface energy as in the cases of A^{-}-LREH and SO_4^{2-}-LREH [30, 40, 41], which makes crystal growth along the [001] direction the hardest to proceed according to the Wulff theorem. This is the primary reason for the two-dimensional (2D) development of GOCSH crystallites with exposed (001) facets. Clearly, vertical growth helps to maximize the exposure of low energy (001) and meanwhile minimize the exposure of high energy (*hk*0) planes. Secondly, the consumption by nucleation and crystallite growth tends to deplete the solutes (Gd^{3+}, SO_4^{2-}, OH^{-} and CO_3^{2-}) at the site where these events take place, and further growth needs mass transfer. In this regard, the directional diffusion of solutes toward the growth forefront (substrate direction) may have guided the GOCSH crystallites to develop vertically.

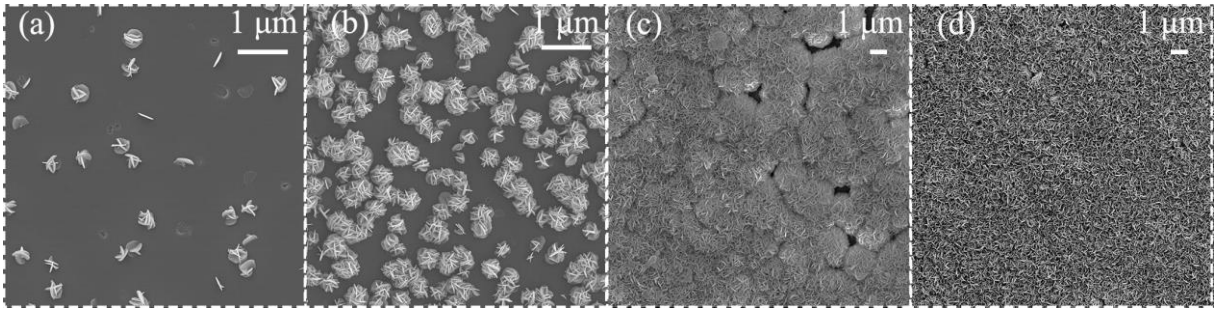

Fig. 4. FE-SEM morphologies of the GOCSH films after deposition at 110 °C for 30 min (a), 60 min (b), 90 min (c) and 120 min (d).

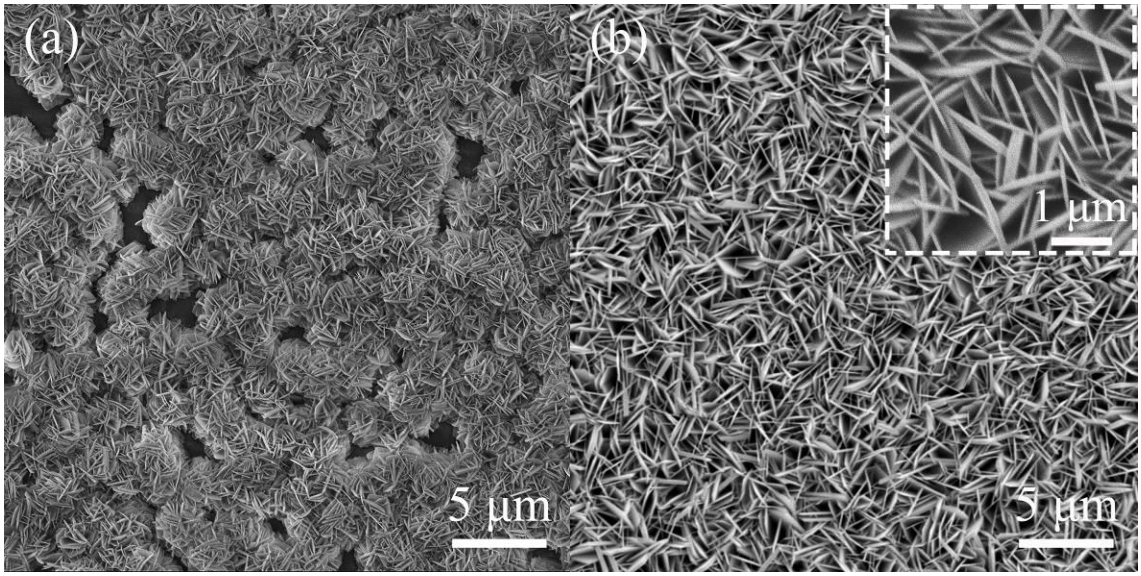

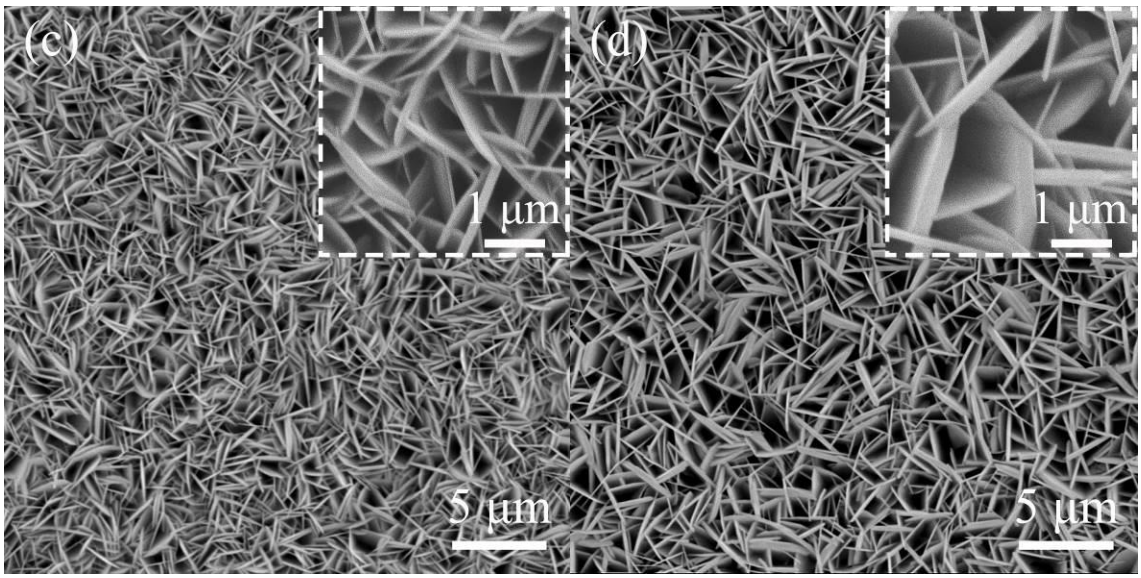

Fig. 5. FE-SEM morphologies of the GOCSH films prepared at 100 ℃ (a), 120 ℃ (b), 130 ℃ (c) and 140 ℃ (d). The insets in (b), (c) and (d) are closer views.

It was also found via FE-SEM that deposition temperature significantly affects the integrity and microstructure of the film, aside from the size of the individual GOCSH crystallites. It is seen form Fig. 5a that the 100 °C film is featured by large voids and incomplete integration of adjacent clusters, which is owing to low nucleation density and insufficient cluster growth. Additionally, the GOCSH platelets were averaged to be ~1 μm and 100 nm in edge length and thickness, respectively. Macroscopically uniform and continuous films were resulted by deposition in the range of 110-140 °C, among which the 110 °C (Fig. 3b), 120 °C (Fig. 5b) and 130 °C (Fig. 5c) ones showed high similarities in terms of pore size (~0.7 μm in average) and dimension of the GOCSH platelets (lateral size ~2.0 μm, thickness ~170 nm). Larger pores (~1.0 μm) and GOCSH crystallites (edge size ~3.0 μm, thickness ~240 nm) were observed for the 140 °C film (Fig. 5d) and this is mainly due to enhanced Ostwald ripening, through which smaller GOCSH crystallites disappeared to create bigger pores and meanwhile larger crystallites grew up at the expense of the smaller ones. Noteworthy is that overgrowth of the GOCSH flakes would weaken film adhesion to the substrate and the film tends to fall off. Therefore, the Ln^{3+} doped GOCSH films were all prepared by 110 °C deposition (Fig. 3a).

3.3 Characterization of the $Gd_2O_2SO_4$:Ln and Gd_2O_2S:Ln films

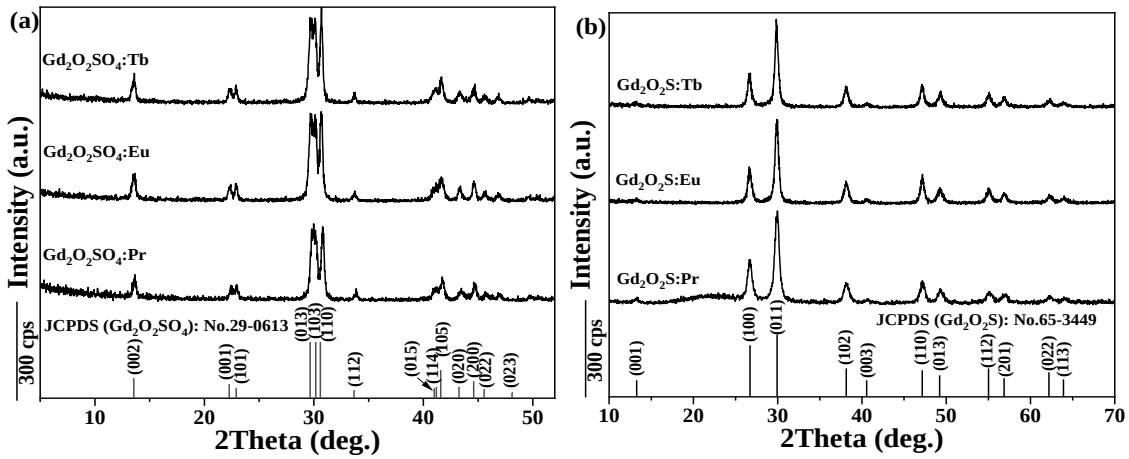

Fig. 6. XRD patterns of the products obtained by annealing the GOCSH:Ln films at 800 °C in air (part a) and in H_2 (part b).

XRD analysis (Fig. 6a) indicated that the products obtained by annealing the GOCSH:Ln films in air at 800 °C well conform to the orthorhombic $Gd_2O_2SO_4$ standard (JCPDS No. 29–0613), which is consistent with the course of phase evolution shown in Fig. S1a. Further annealing the $Gd_2O_2SO_4$:Ln products in flowing hydrogen at 800 °C for another 1 h produced Gd_2O_2S:Ln (Fig. 6b), since in each case the diffraction peaks can be fully indexed with those of the hexagonal Gd_2O_2S standard (space group *P*-3*m*1; JCPDS No. 65–3449).

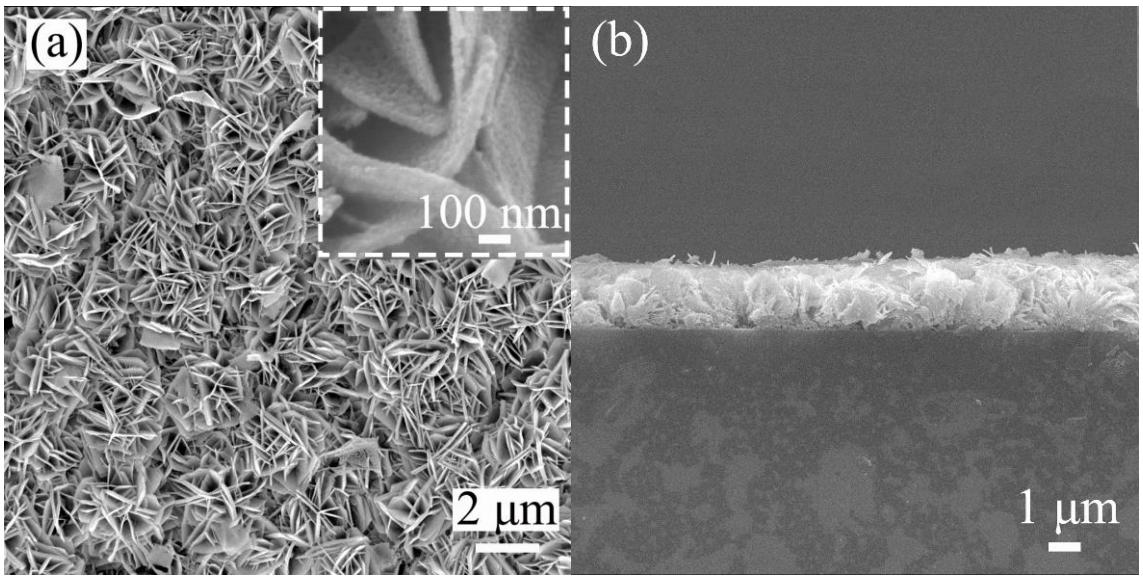

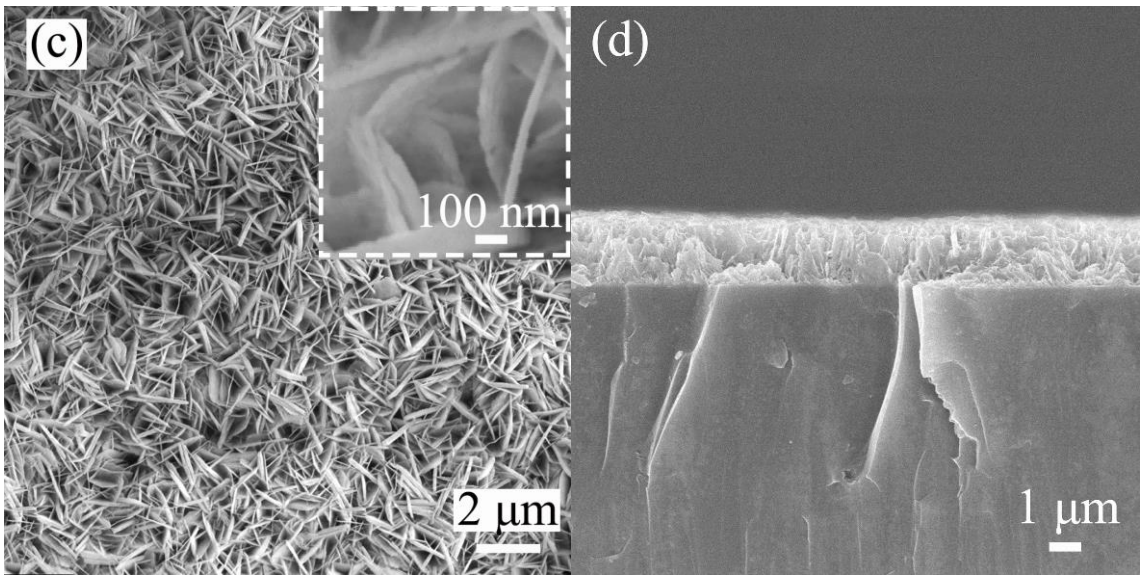

Fig. 7. FE-SEM morphologies of the 800 °C annealed $Gd_2O_2SO_4$:Eu (a, b) and Gd_2O_2S:Pr (c, d) films, where the insets in (a) and (c) are closer views.

Fig. 7 shows the FE-SEM microstructures of the calcination products, with $Gd_2O_2SO_4$:Eu (Fig. 7a,b) and Gd_2O_2S:Pr (Fig. 7c,d) as typical examples. It is seen from either surface view (Fig. 7a,c) or cross-section view (Fig. 7b,d) that they well preserved the structural features of the GOCSH film (Fig. 3b,c). Owing to the mass loss (release of H_2O and CO_2) and nucleation of new phase in the parent phase during annealing, however, each of the original GOSCH:Ln flakes (single crystalline) was transformed into a polycrystalline aggregate (Fig. 7a,c, the insets). GOSCH, $Gd_2O_2SO_4$ and Gd_2O_2S present high structural similarities and are all layered along the *c*-axis, with the anions (SO_4^{2-}, CO_3^{2-}, S^{2-}) sandwiched between the main layers built up of Gd-O polyhedrons [42, 43]. This allows phase transformation to proceed in a quasi-topotactic way [37, 44], which helps to maintain the morphology of the individual flake and the film through minimization of mass diffusion and phase-transition stress. Broadening analysis of the XRD peaks (Fig. 6) with Scherrer formula [45] found average crystallite sizes of ~28 and 15 nm for all the $Gd_2O_2SO_4$:Ln and Gd_2O_2S:Ln films annealed at 800 °C, respectively, irrespectively of the type and content of Ln. Though high-temperature

annealing helps to improve product crystallinity for a better luminescence, the Gd_2O_2S:Ln films obtained at 900 and 1000 °C have macropores/cracks and tend to peel off from the substrate due to the shrinkage stress arising from sintering/densification (Fig. S2).

3.4 Optical properties of the $Gd_2O_2SO_4$:Ln and Gd_2O_2S:Ln films

Fig. 8 shows the PLE and PL spectra of the $Gd_2O_2SO_4$:Eu and $Gd_2O_2SO_4$:Tb films. For $Gd_2O_2SO_4$:Eu (Fig. 8a), the PLE spectrum obtained by monitoring the red emission at 617 nm contains a broad and strong band at ~275 nm and also a few negligibly weak sharp peaks in the longer wavelength region for the intra-4f^6 transition of Eu^{3+}. The broad band should be overlapped from O^{2-}-Eu^{3+}charge transfer (CT, excitation of electrons from the 2*p* orbital of O to the 4*f* orbital of Eu) and the $^8S_{7/2} \rightarrow {}^6I_J$ excitation transition of Gd^{3+} [46], as the latter clearly appeared in the PLE of $Gd_2O_2SO_4$:Tb (Fig. 8b). The PL spectrum obtained under 275 nm excitation exhibited the typical $^5D_0 \rightarrow {}^7F_J$ (J = 0-4) emissions of Eu^{3+}, with the $^5D_0 \rightarrow {}^7F_2$ red one (~617 nm) being the most prominent. For $Gd_2O_2SO_4$:Tb (Fig. 8b), the PLE spectrum recorded by monitoring the 545 nm green emission showed four sharp bands in the ~200-350 nm region, with the ~209 nm one for host excitation, the 228 nm dominant one for spin-allowed $4f^8 \rightarrow 4f^75d^1$ intra-configurational transition of Tb^{3+}, and the ~275 and 312 nm ones for $^8S_{7/2} \rightarrow {}^6I_J$ and $^8S_{7/2} \rightarrow {}^6P_J$ intra-$4f^7$ transitions of Gd^{3+}, respectively. Under 228 nm excitation, the film showed luminescence via transition from the $^5D_3$ and $^5D_4$ excited states to ^7F_J (J = 3–6) ground multiplets of Tb^{3+}, as labeled in the figure, with the $^5D_4 \rightarrow {}^7F_5$ green emission at ~545 nm being overwhelmingly strong. The Eu^{3+} and Tb^{3+} doped $Gd_2O_2SO_4$ films were analyzed from their PL spectra to have quantum yields (QYs) of ~32.5 and 20.2% and Commission Internationale de L'Eclairage (CIE) chromaticity coordinates of around (0.650, 0.350) and (0.287, 0.482), respectively. The red (Eu^{3+}) and green (Tb^{3+}) luminescence can be

seen from the CIE diagram (Fig. S3a) and digital pictures (Fig. 8, the insets). Fluorescence decay analysis found that the main luminescence of Eu^{3+} (λ_{em} = 617 nm, λ_{ex} = 275 nm) and Tb^{3+} (λ_{em} = 545 nm, λ_{ex} = 228 nm) both decreased in a single exponential manner and has lifetime values of 1.77±0.01 ms and 2.82±0.02 ms, respectively (Fig. S4a). No data, however, are available from the literature for quantum yield and lifetime comparison. Noteworthy is that the $Gd_2O_2SO_4$:Pr film is hardly luminescent. In view that Pr^{3+} is even slightly less oxidizable than Tb^{3+} in either solution or crystal [47], the possible oxidation by calcination in air was ruled out. It was thus believed that the quenching of Pr^{3+} luminescence is due to placement of the $4f^15d^1$ excited energy level of Pr^{3+}, which is sensitive to crystal field and lattice covalency [48], in the conduction band of $Gd_2O_2SO_4$.

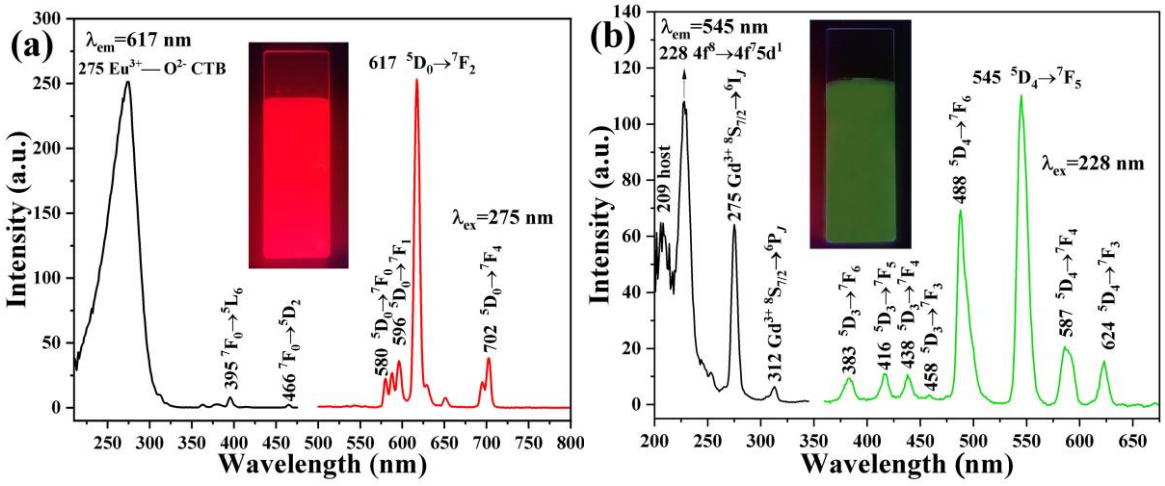

Fig. 8. PLE (left) and PL (right) spectra of the $Gd_2O_2SO_4$:Eu (a) and $Gd_2O_2SO_4$:Tb (b) films. The insets are digital photographs taken for the appearance of luminescence under 254 nm UV irradiation.

Fig. 9 shows the photoluminescence of the Gd_2O_2S:Ln films. From the PLE spectra taken by monitoring the strongest emission of the corresponding activator ion, which is ~513 nm for Pr^{3+}, ~626 nm for Eu^{3+} and ~545 nm for Tb^{3+}, it is seen that the $4f^2 \rightarrow 4f^15d^1$ inter-configurational transition of Pr^{3+} at ~302 nm (Fig. 9a), O^{2-}/S^{2-}-Eu^{3+} CT (simultaneous excitation of O 2*p* and S 3*p* electrons to the 4*f* orbital of Eu) at ~329 nm (Fig. 9b) and the

low-spin $4f^8 \rightarrow 4f^75d^1$ inter-configurational transition of Tb^{3+} at ~286 nm (Fig. 9c) are the most efficient excitation sources. Besides, the $^8S_{7/2} \rightarrow {}^6I_J$ excitation of Gd^{3+} (~275 nm) appeared in each of the excitation spectra, indicating the presence of energy transfer from Gd^{3+} to the activator ions [49-51]. In view that the bandgap energy of Gd_2O_2S is ~4.6-4.8 eV (~258-270 nm), the ~268 nm peak in the PLE of Pr^{3+} can then be assigned to host excitation (Fig. 9a). Such a peak should also exist in the other two cases but is not clearly identifiable owing to spectral overlapping. It is seen by comparing the PLE spectra of Fig. 8 and Fig. 9 that the CT band of Eu^{3+} and the $4f^8 \rightarrow 4f^75d^1$ transition of Tb^{3+} in Gd_2O_2S were significantly re-shifted, which is owing to increased lattice covalency by partially replacing O ligands (electronegativity χ=3.44) with remarkably less electronegative S (χ=2.58) for Gd coordination (GdO_6 trigonal prism in $Gd_2O_2SO_4$ and mono-capped GdO_4S_3 polyhedron in Gd_2O_2S) [42, 43]. Under excitation with the aforementioned wavelengths, the three films produced sharp green (Pr^{3+}, ~513 nm), red (Eu^{3+}, ~626 nm), and green (Tb^{3+}, ~545 nm) emissions, as seen from the photographs taken for the appearance of luminescence (Fig. 9d). In each case, the other emissions are arising from intra-4*f* transitions of the activator ion, as labelled in the corresponding PL spectrum. The Gd_2O_2S:Pr, Gd_2O_2S:Eu, and Gd_2O_2S:Tb films were analyzed from their PL spectra to have QYs of ~24.7, 22.3, and 27.9% and CIE color coordinates (Fig. S3b) of about (0.147, 0.567), (0.644, 0.352) and (0.306, 0.562), respectively. The QY of Gd_2O_2S:Pr film is close to the 25.1% reported for its powder form [52], and those of Gd_2O_2S:Eu and Gd_2O_2S:Tb are remarkably larger than the values reported for the $(Gd_{0.975}Eu_{0.025})_2O_2S$ (~7.7%) and $(Gd_{0.975}Tb_{0.025})_2O_2S$ (~14.6%) powders obtained by sulfurization of solvothermal precursors in a N_2/S atmosphere [53]. The dominant

luminescence of the Gd_2O_2S:Ln films was also found to decay single-exponentially (Fig. S4b,c), and has a lifetime of 2.66±0.02 μs for Pr^{3+} (λ_{em} = 513 nm, λ_{ex} = 249 nm), 0.67±0.01 ms for Eu^{3+} (λ_{em} = 626 nm, λ_{ex} = 329 nm) and 1.21±0.01 ms for Tb^{3+} (λ_{em} = 545 nm, λ_{ex} = 286 nm). The values are in reasonable agreement with those reported for the corresponding Gd_2O_2S:Ln powders, which are ~2.36-6.73 μs for Pr^{3+} [52, 54], ~0.45-0.7 ms for Eu^{3+} [43, 53, 55] and ~0.78-1.34 ms for Tb^{3+} [53, 56].

Eu^{3+} occupies the low-symmetric C_1 and C_{3v} sites of Gd^{3+} in $Gd_2O_2SO_4$ and Gd_2O_2S, respectively, and therefore the parity forbidden $^5D_0 \rightarrow {}^7F_2$ electric dipole transition is stronger than the parity allowed $^5D_0 \rightarrow {}^7F_1$ magnetic dipole transition in both the cases [57]. The $I(^5D_0 \rightarrow {}^7F_2)/I(^5D_0 \rightarrow {}^7F_1)$ intensity ratio, however, is different for the two types of films, which is ~7.00 for $Gd_2O_2SO_4$:Eu and ~8.52 for Gd_2O_2S:Eu. In view that C_1 is lower than C_{3v} and the two films have almost identical structures, the lager intensity ratio of Gd_2O_2S:Eu may thus mainly be due to smaller grain size (~15 nm, ~28 nm for $Gd_2O_2SO_4$:Eu), which makes more Eu^{3+} reside at lower-symmetric interface sites. Meanwhile, the $^5D_3 \rightarrow {}^7F_J$ emission of Tb^{3+} in Gd_2O_2S is much weaker than that in $Gd_2O_2SO_4$, as seen from the $(^5D_4 \rightarrow {}^7F_5)/(^5D_3 \rightarrow {}^7F_5)$ intensity ratio, which is ~32.6 for the former and ~8.6 for the latter. Analysis of the average separation distance (R) of Tb^{3+} with the equation $R \approx 2[3V/(4\pi xN)]^{1/3}$ [58] found a value of ~1.74 nm for $Gd_2O_2SO_4$ and ~1.59 nm for Gd_2O_2S, where V is the volume of the unit cell (~220.5 $Å^3$ for $Gd_2O_2SO_4$ and ~85.7 $Å^3$ for Gd_2O_2S), x is the content of Tb^{3+} (x = 0.02), and N is the number of Gd^{3+} sites in the unit cell (N = 4 for $Gd_2O_2SO_4$ and N = 2 for Gd_2O_2S). It can thus be said that the remarkably larger $(^5D_4 \rightarrow {}^7F_5)/(^5D_3 \rightarrow {}^7F_5)$ ratio of Gd_2O_2S:Tb may mainly be due to more pronounced cross-relaxation via $Tb^{3+}(^5D_3) + Tb^{3+}(^7F_6) \rightarrow Tb^{3+}(^5D_4) +$

Tb^{3+}($^7F_0$) by the smaller *R* value, which reduced the emission from $^5D_3$ and meanwhile enhanced the emission from $^5D_4$.

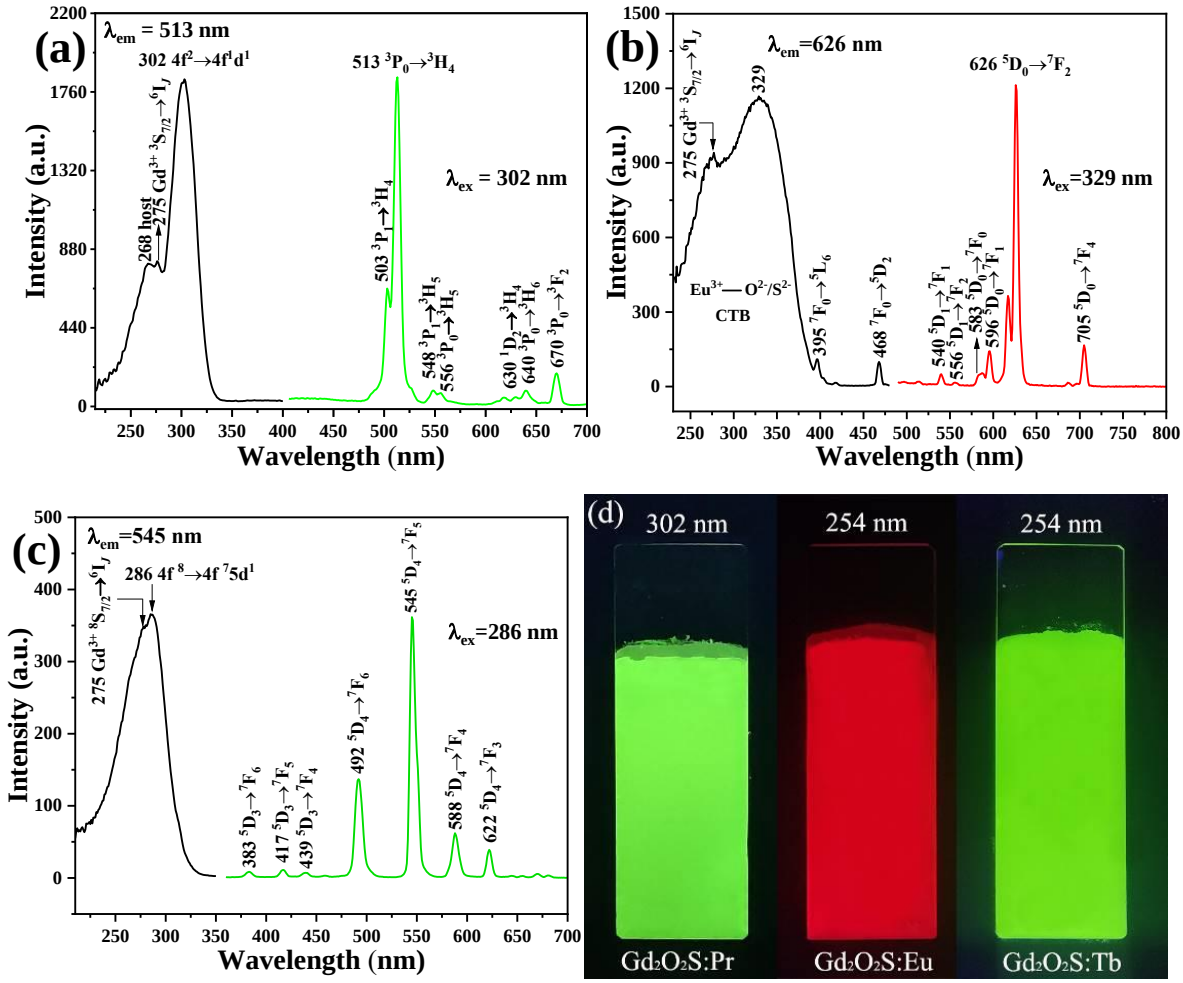

Fig. 9. PLE (left) and PL (right) spectra of the Gd_2O_2S:Pr (a), Gd_2O_2S:Eu (b) and Gd_2O_2S:Tb (c) films. Part (d) is a digital photograph showing the appearance of film luminescence under UV irradiation.

Fig. 10a illustrates the transmittance spectra of representative films in the 200-700 nm spectral region, together with that of the quartz substrate. For GOCSH, the absorption band in the ~240-350 nm region (centered at ~275 nm) should mainly be caused by the $^8S_{7/2} \rightarrow {}^6I_J$ and $^8S_{7/2} \rightarrow {}^6P_J$ transitions of Gd^{3+}, which take place at ~275 and 312 nm, respectively (Fig. 8b), although light scattering by the film itself may also contribute to the band. All the other films showed significantly stronger light absorption in the range of ~240-400 nm, owing to excitation transitions of the doped activator ions and host absorption, and the absorption

profiles are in accordance with their respective PLE spectra (Fig. 8 and Fig. 9a-c). It is also seen from Fig. 10a that all the films are similarly transparent at each wavelength in the visible light region (400-700 nm), which is ~70% at 400 nm and ~93% at 700 nm. The extent of light transmission can be perceived from the photograph shown in Fig. 10b. $Gd_2O_2SO_4$ and Gd_2O_2S would be fully transparent to visible light since the energy of the 400 nm light (~3.1 eV) is remarkably smaller than their bandgap energies. The lower transmittance of these two types of films than bare quartz is thus mainly caused by microstructure-induced light scattering, and the better transparency at a longer wavelength is owing to less scattering of the incident light. This should also be the case for the GOCSH film. The quite similar visible light transmission further imply that the three types of films are close to each other in macro-/microstructure, irrelevant of calcination, conforming to the results of FE-SEM observation (Fig. 3b and Fig. 7).

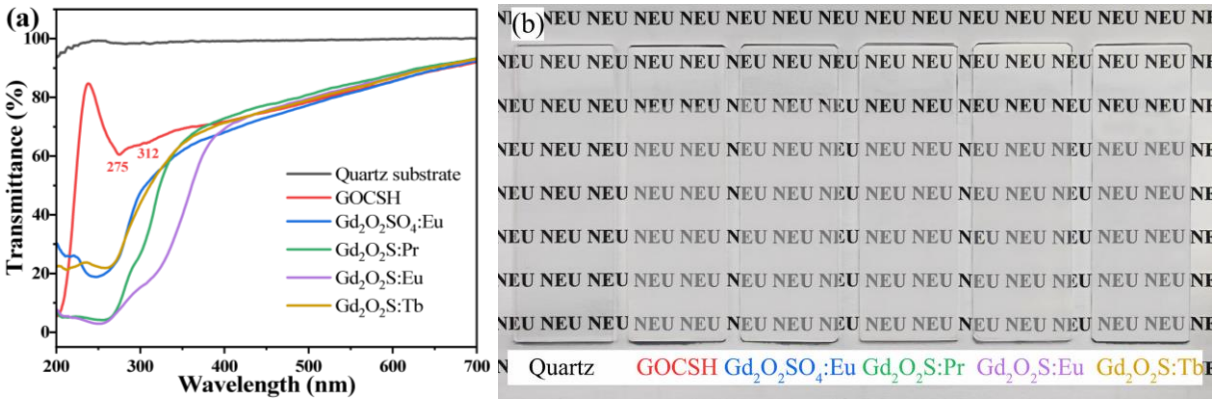

Fig. 10. Transmittance spectra of the typical films and bare quartz (a) and a photograph showing the appearance of light transmission (b).

3.5 Surface wettability of the films

The wettability of a solid surface highly depends on the chemical composition and geometrical feature of the surface, and deliberately creating a micro-/nanostructured porous surface is well known to be an efficient way to achieve super-hydrophobicity [59, 60]. In view

of their morphological structures revealed by FE-SEM (Fig. 3b and Fig. 7), the GOSCH, $Gd_2O_2SO_4$:Eu and Gd_2O_2S:Ln typical films were tested for water wettability and the results are shown in Fig. 11. It is clear that all the films are superhydrophobic, since the water droplet (4 μL) was formed as a sphere on film surface with a contact angle (CA) greater than 150°. In view that RE_2O_2S is generally weaker than its oxide counterpart against water vapor, particularly acidic and alkaline ones, such a water-repellant property may allow a longer stability of Ln^{3+} luminescence. Super-hydrophobicity may be attributed to the roughness of the surface sufficiently amplifying the inherent hydrophobicity of a material according to the Wenzel equation [59], and meanwhile the air trapped in the porous microstructure of the surface may contribute to super-hydrophobicity by increasing the air/liquid interface according to the Cassie-Baxter equation [60]. The latter may have played an essential role in this work, since none of the above compounds is intrinsically hydrophobic.

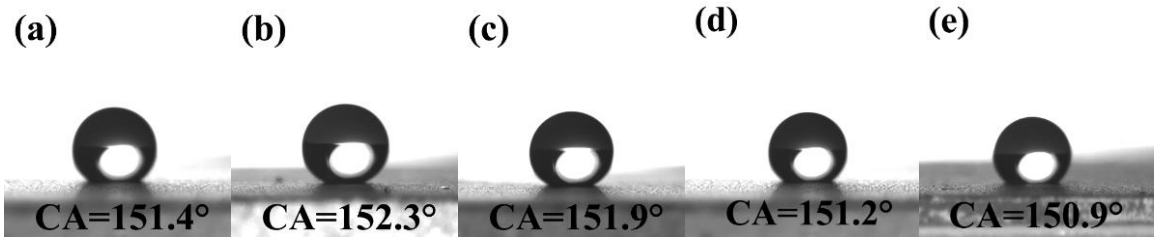

Fig. 11. Water wettability test of the films, with parts (a)-(e) for GOCSH, $Gd_2O_2SO_4$:Eu, Gd_2O_2S:Pr, Gd_2O_2S:Eu and Gd_2O_2S:Tb, respectively.

4. Conclusion

A $Gd_2(OH)_2CO_3SO_4 \cdot H_2O$ (GOCSH) new co*m*pound was obtained in this work via hydrothermally reacting $Gd(NO_3)_3$, $(NH_4)_2SO_4$ and urea, which was found to crystallize in the tetragonal system (space group *P*-42$_1$*m*) with a layered structure along the *c*-axis. With such a reaction system, applying heterogeneous nucleation on quartz substrate produced macro-/microscopically uniform GOSCH:Ln films via vertical self-alignment of platelike

crystallites, and the optimal temperature for film deposition is 110-130 °C. Owing to the exactly the same S/(Gd,Ln) molar ratio, $Gd_2O_2SO_4$:Ln and Gd_2O_2S:Ln films of similar morphological structures were successfully transformed from the GOSCH:Ln films by subsequent annealing in air and hydrogen at 800 °C, respectively, without additional sulfurization. Aside from luminescence, the films have microstructure-induced super-hydrophobicity and are transparent (~70-93%) in the visible light region. The multi-functional films, particularly those of Gd_2O_2S:Ln, may find potential application for luminescence, display, scintillation and micro-imaging.

Acknowledgements

This work was supported in part by the National Natural Science Foundation of China (Grant No. 51972047 and 52172112).

References

[1] C. Greskovich, S. Duclos, Ceramic scintillators, Annu. Rev. Mater. Sci., 27 (1997) 69-88.
[2] B. Ortega-Berlanga, L. Betancourt-Mendiola, C. del Angel-Olarte, L. Hernández-Adame, S. Rosales-Mendoza, G. Palestino, An overview of gadolinium-based oxide and oxysulfide particles: Synthesis, properties, and biomedical applications, Crystals, 11 (2021) 1094.
[3] S. Shionoya, W.M. Yen, H. Yamamoto, Phosphor Handbook, CRC Press, New York, 2018.
[4] W. Wang, H. Kou, S. Liu, Y. Shi, J. Li, Y. Li, X. Feng, Y. Pan, J. Guo, Comparison of the optical and scintillation properties of Gd_2O_2S:Pr,Ce ceramics fabricated by hot pressing and pressureless sintering, Opt. Mater., 42 (2015) 199-203.
[5] M. Yoshida, M. Nakagawa, H. Fujii, F. Kawaguchi, H. Yamada, Y. Ito, H. Takeuchi, T. Hayakawa, Y. Tsukuda, Application of Gd_2O_2S ceramic scintillator for X-ray solid state detector in X-ray CT, Jpn. J. Appl. Phys., 27 (1988) L1572-L1575.
[6] S.A. Osseni, S. Lechevallier, M. Verelst, C. Dujardin, J. Dexpert-Ghys, D. Neumeyer, M. Leclercq, H. Baaziz, D. Cussac, V. Santran, R. Mauricot, New nanoplatform based on $Gd_2O_2S:Eu^{3+}$ core: synthesis, characterization and use for in vitro bio-labelling, J. Mater. Chem., 21 (2011) 18365.
[7] V.V. Bakovets, A.V. Sotnikov, I.V. Korolkov, Kinetics of phase formation in the Ln-O-S (Ln = La, Gd, Y) systems during oxide sulfidation in ammonium thiocyanate vapor, J. Am.

Ceram. Soc., 100 (2017) 1320-1329.
[8] Z. Fu, Y. Geng, H. Chen, S. Zhou, H.K. Yang, J.H. Jeong, Combustion synthesis and luminescent properties of the Eu^{3+}-doped yttrium oxysulfide nanocrystalline, Opt. Mater., 31 (2008) 58-62.
[9] F. Riva, Development of new thin film scintillators for high-resolution X-ray imaging, in, Université de Lyon, 2016.
[10] M. Nikl, Nanocomposite, ceramic, and thin film scintillators, Jenny Stanford Publishing, New York, 2016.
[11] P. Lecoq, A. Gektin, M. Korzhik, Inorganic scintillators for detector systems: Physical principles and crystal engineering, Springer, Berlin, Germany, 2017.
[12] J.J. Dolo, H.C. Swart, J.J. Terblans, E. Coetsee, O.M. Ntwaeaborwa, B.F. Dejene, X-ray photoelectron spectroscopy analysis for undegraded and degraded $Gd_2O_2S:Tb^{3+}$ phosphor thin films, Phys. B, 407 (2012) 1586-1590.
[13] X. Wang, M.S. Molokeev, Q. Zhu, J.-G. Li, Controlled hydrothermal crystallization of anhydrous $Ln_2(OH)_4SO_4$ (Ln=Eu–Lu, Y) as a new family of layered rare earth metal hydroxides, Chem. Eur. J., 23 (2017) 16034-16043.
[14] X. Wang, J.-G. Li, M.S. Molokeev, X. Wang, W. Liu, Q. Zhu, H. Tanaka, K. Suzuta, B.-N. Kim, Y. Sakka, Hydrothermal crystallization of a $Ln_2(OH)_4SO_4{\cdot}nH_2O$ layered compound for a wide range of Ln (Ln = La–Dy), thermolysis, and facile transformation into oxysulfate and oxysulfide phosphors, RSC Adv., 7 (2017) 13331-13339.
[15] T. Sugimoto, Preparation of monodispersed colloidal particles, Adv. Colloid Interface Sci., 28 (1987) 65-108.
[16] E. Matijević, Production of monodispersed colloidal particles, Annu. Rev. Mater. Sci., 15 (2003) 483-516.
[17] E. Matijević, W.P. Hsu, Preparation and properties of monodispersed colloidal particles of lanthanide compounds: I. Gadolinium, europium, terbium, samarium, and cerium(III), J. Colloid Interface Sci., 118 (1987) 506-523.
[18] J.-G. Li, X. Li, X. Sun, T. Ishigaki, Monodispersed Colloidal Spheres for Uniform $Y_2O_3:Eu^{3+}$ Red-Phosphor Particles and Greatly Enhanced Luminescence by Simultaneous Gd^{3+} Doping, J. Phys. Chem. C, 112 (2008) 11707-11716.
[19] E. Matijević, Preparation and properties of uniform size colloids, Chem. Mater., 5 (1993) 412-426.
[20] Y. Zhou, F. Li, X. Wang, Q. Zhu, X. Li, X. Sun, J.-G. Li, Facile synthesis of $Gd_2O_2SO_4$:Tb and Gd_2O_2S:Tb green phosphor nanopowders of unimodal size distribution and photoluminescence, Adv. Powder Technol., 32 (2021) 1911-1919.
[21] Z. Luo, F. Li, Q. Zhu, X. Sun, J.-G. Li, Low-temperature green synthesis of nanocrystalline $La_2O_2S:Pr^{3+}$ powders and investigation of photoluminescence, J. Mater. Res. Technol., 17 (2022) 2540-2549.
[22] J.A. Gadsden, Infrared spectra of minerals and related inorganic compounds, Butterworth, London, 1975.
[23] F. Li, J.-G. Li, Q. Zhu, EDTA-promoted aliovalent Eu^{3+} doping of $Sr_5(PO_4)_3F$ apatite, growth behavior and luminescence, Opt. Mater., 101 (2020) 109765.
[24] H. Qin, X. Zhang, H. Liu, Y. Sang, J. Wang, Mechanism of ammonium sulfate regulation effect on microstructure of Y_2O_3 nanopowders via urea precipitation method,

CrystEngComm, 15 (2013) 5076.
[25] J. Liang, R. Ma, F. Geng, Y. Ebina, T. Sasaki, $Ln_2(OH)_4SO_4 \cdot nH_2O$ (Ln = Pr to Tb; $n \sim 2$): A new family of layered rare-earth hydroxides rigidly pillared by sulfate ions, Chem. Mater., 22 (2010) 6001-6007.
[26] J.W. Visser, A fully automatic program for finding the unit cell from powder data, J. Appl. Crystallogr., 2 (1969) 89-95.
[27] A. Boultif, D. Louër, Indexing of powder diffraction patterns for low-symmetry lattices by the successive dichotomy method, J. Appl. Crystallogr., 24 (1991) 987-993.
[28] P.-E. Werner, L. Eriksson, M. Westdahl, TREOR, a semi-exhaustive trial-and-error powder indexing program for all symmetries, J. Appl. Crystallogr., 18 (1985) 367-370.
[29] G. Pawley, Unit-cell refinement from powder diffraction scans, J. Appl. Crystallogr., 14 (1981) 357-361.
[30] F. Geng, R. Ma, Y. Matsushita, J. Liang, Y. Michiue, T. Sasaki, Structural study of a series of layered rare-earth hydroxide sulfates, Inorg. Chem., 50 (2011) 6667-6672.
[31] M. Hämmer, H.A. Höppe, Crystalline orthorhombic $Ln[CO_3][OH]$ (Ln=La, Pr, Nd, Sm, Eu, Gd) compounds hydrothermally synthesised with CO_2 from air as carbonate source, Z. Naturforsch., 74 (2019) 59-70.
[32] Z. Luo, F. Li, Q. Zhu, X. Li, X. Sun, J.-G. Li, Sulfidization-free synthesis of well dispersed $(Gd,La)_2O_2S:Pr^{3+}$ nanopowders and the effect of La^{3+} on structure and luminescence, J. Mater. Res. Technol., 18 (2022) 4216-4227.
[33] Z. Xu, Q. Zhu, X. Sun, J.-G. Li, A novel precursor route for $Y_2Mo_4O_{15}:Yb^{3+},Ho^{3+}$ phosphor and investigation of up-conversion luminescence, Adv. Powder Technol., 32 (2021) 1276-1286.
[34] X. Shi, J.-G. Li, X. Wang, Q. Zhu, B.N. Kim, X. Sun, Facile hydrothermal crystallization of $NaLn(WO_4)_2$ (Ln=La-Lu, and Y), phase/ morphology evolution, and photoluminescence, Sci. Technol. Adv. Mat., 18 (2017) 741-754.
[35] D. Sordelet, M. Akinc, Preparation of spherical, monosized Y_2O_3 precursor particles, J. Colloid Interface Sci., 122 (1988) 47-59.
[36] B. Aiken, W.P. Hsu, E. Matijević, Preparation and properties of monodispersed colloidal particles of lanthanide compounds: III, yttrium(III) and mixed yttrium(III)/cerium(III) systems, J. Am. Ceram. Soc., 71 (1988) 845-853.
[37] L. Hu, R. Ma, T.C. Ozawa, T. Sasaki, Synthesis of a solid solution series of layered $Eu_xGd_{1-x}(OH)_{2.5}Cl_{0.5} \cdot 0.9H_2O$ and its transformation into $(Eu_xGd_{1-x})_2O_3$ with enhanced photoluminescence properties, Inorg. Chem., 49 (2010) 2960-2968.
[38] L. Hu, R. Ma, T.C. Ozawa, F. Geng, N. Iyi, T. Sasaki, Oriented films of layered rare-earth hydroxide crystallites self-assembled at the hexane/water interface, Chem. Commun. , (2008) 4897-4899.
[39] Q. Zhu, J.-G. Li, C. Zhi, R. Ma, T. Sasaki, J.X. Xu, C.H. Liu, X.D. Li, X.D. Sun, Y. Sakka, Nanometer-thin layered hydroxide platelets of $(Y_{0.95}Eu_{0.05})_2(OH)_5NO_3 \cdot xH_2O$: exfoliation-free synthesis, self-assembly, and the derivation of dense oriented oxide films of high transparency and greatly enhanced luminescence, J. Mater. Chem. C, 21 (2011) 6903-6908.
[40] F. Geng, Y. Matsushita, R. Ma, H. Xin, M. Tanaka, F. Izumi, N. Iyi, T. Sasaki, General synthesis and structural evolution of a layered family of $Ln_8(OH)_{20}Cl_4 \cdot nH_2O$ (Ln = Nd, Sm,

Eu, Gd, Tb, Dy, Ho, Er, Tm, and Y), J. Am. Chem. Soc., 130 (2008) 16344-16350.
[41] X. Wu, J.-G. Li, Q. Zhu, W. Liu, J. Li, X. Li, X. Sun, Y. Sakka, One-step freezing temperature crystallization of layered rare-earth hydroxide ($Ln_2(OH)_5NO_3{\cdot}nH_2O$) nanosheets for a wide spectrum of Ln (Ln = Pr-Er, and Y), anion exchange with fluorine and sulfate, and microscopic coordination probed via photoluminescence, J. Mater. Chem. C, 3 (2015) 3428-3437.
[42] M. Machida, K. Kawamura, K. Ito, K. Ikeue, Large-capacity oxygen storage by lanthanide oxysulfate/oxysulfide systems, Chem. Mater., 17 (2005) 1487-1492.
[43] X. Wang, J.-G. Li, M.S. Molokeev, Q. Zhu, X. Li, X. Sun, Layered hydroxyl sulfate: Controlled crystallization, structure analysis, and green derivation of multi-color luminescent $(La,RE)_2O_2SO_4$ and $(La,RE)_2O_2S$ phosphors (RE = Pr, Sm, Eu, Tb, and Dy), Chem. Eng. J., 302 (2016) 577-586.
[44] L. Hu, R. Ma, T.C. Ozawa, T. Sasaki, Oriented monolayer film of Gd_2O_3:0.05Eu crystallites: quasi-topotactic transformation of the hydroxide film and drastic enhancement of photoluminescence properties, Angew. Chem. Int. Ed. , 48 (2009) 3846-3849.
[45] P. Scherrer, Estimation of the size and internal structure of colloidal particles by means of röntgen, Göttinger Nachrichten Math. Phys., 2 (1918) 96-100.
[46] J.-G. Li, X. Li, X. Sun, T. Ikegami, T. Ishigaki, Uniform colloidal spheres for $(Y_{1-x}Gd_x)_2O_3$ (x = 0–1): Formation mechanism, compositional impacts, and physicochemical properties of the oxides, Chem. Mater., 20 (2008) 2274-2281.
[47] T.P. Gompa, A. Ramanathan, N.T. Rice, H.S. La Pierre, The chemical and physical properties of tetravalent lanthanides: Pr, Nd, Tb, and Dy, Dalton. Trans., 49 (2020) 15945-15987.
[48] A.M. Srivastava, Aspects of Pr^{3+} luminescence in solids, J. Lumin., 169 (2016) 445-449.
[49] G. Blasse, G.J. Dirksen, Long-range energy transfer from Gd^{3+} to Pr^{3+}, J. Solid State Chem., 73 (1988) 599-602.
[50] Y. Sun, H. Zou, B. Zhang, X. Zhou, Y. Song, K. Zheng, Z. Shi, Y. Sheng, Luminescent properties and energy transfer of Gd^{3+}/Eu^{3+} co-doped cubic $CaCO_3$, J. Lumin., 178 (2016) 307-313.
[51] Y.-C. Li, Y.-H. Chang, Y.-S. Chang, Y.-J. Lin, C.-H. Laing, Luminescence and energy transfer properties of Gd^{3+} and Tb^{3+} in $LaAlGe_2O_7$, J. Phys. Chem. C, 111 (2007) 10682-10688.
[52] X. Wang, X. Wang, Z. Wang, Q. Zhu, G. Zhu, C. Wang, S. Xin, J.-G. Li, Photo/cathodoluminescence and stability of Gd_2O_2S:Tb,Pr green phosphor hexagons calcined from layered hydroxide sulfate, J. Am. Ceram. Soc., 101 (2018) 5477-5486.
[53] Y. Song, H. You, Y. Huang, M. Yang, Y. Zheng, L. Zhang, N. Guo, Highly uniform and monodisperse $Gd_2O_2S:Ln^{3+}$ (Ln = Eu, Tb) submicrospheres: Solvothermal synthesis and luminescence properties, Inorg. Chem., 49 (2010) 11499-11504.
[54] H. Yamada, A. Suzuki, Y. Uchida, M. Yoshida, H. Yamamoto, Y. Tsukuda, A scintillator Gd_2O_2S:Pr ,Ce ,F for X-ray computed tomography, J. Electrochem. Soc., 136 (1989) 2713-2716.
[55] X. Wang, J.-G. Li, Q. Zhu, X. Li, X. Sun, Y. Sakka, Facile and green synthesis of $(La_{0.95}Eu_{0.05})_2O_2S$ red phosphors with sulfate-ion pillared layered hydroxides as a new type of precursor: controlled hydrothermal processing, phase evolution and photoluminescence, Sci.

Technol. Adv. Mater., 15 (2014) 014204.
[56] X. Wang, Q. Meng, M. Li, X. Wang, Z. Wang, Q. Zhu, J.-G. Li, A low temperature approach for photo/cathodoluminescent Gd_2O_2S:Tb (GOS:Tb) nanophosphors, J. Am. Ceram. Soc., 102 (2019) 3296-3306.
[57] G. Blasse, G.J. Dirksen, F. Zonnevijlle, The luminescence of some lanthanide decatung-states and other polytungstates, J. Inorg. Nucl. Chem., 43 (1981) 2847-2853.
[58] G. Blasse, Energy transfer between inequivalent Eu^{2+} ions, J. Solid State Chem., 62 (1986) 207-211.
[59] R.N. Wenzel, Resistance of solid surfaces to wetting by water, Ind. Eng. Chem., 28 (1936) 988-994.
[60] A.B.D. Cassie, S. Baxter, Wettability of porous surfaces, Trans. Faraday Soc., 40 (1944) 546-551.

Vertically aligned $Gd_2O_2SO_4$:Ln and Gd_2O_2S:Ln luminescent films with super-hydrophobicity via a novel precursor route (Ln = Pr, Eu, Tb)

Fan Li[a], Minghui Jin[a], Zhuowei Li[a], Xuejiao Wang[b], Qi Zhu[a], Ji-Guang Li[c,*]

[a]Key Laboratory for Anisotropy and Texture of Materials (Ministry of Education) and School of Materials Science and Engineering, Shenyang, Liaoning, 110819, China

[b]College of Chemistry and Materials Engineering, Bohai University, Jinzhou, Liaoning 121007, China

[c]Research Center for Functional Materials, National Institute for Materials Science, Tsukuba, Ibaraki, 305-0044, Japan

[*]Corresponding author

Dr. Ji-Guang Li

National Institute for Materials Science

Tel: +81-29-860-4394

E-mail: li.jiguang@nims.go.jp

Abstract

Pr^{3+}, Eu^{3+} and Tb^{3+} activated Gd_2O_2S (Gd_2O_2S:Ln), either in the powder or ceramic form, are well known for their wide applications in photoluminescence (PL), cathodoluminescence (CL) and X-ray excited luminescence (XEL) due to high efficiency. The film form of Gd_2O_2S:Ln, however, has not been reported up to date to the best of our knowledge. By hydrothermally reacting $Gd(NO_3)_3$, $(NH_4)_2SO_4$ and urea, this work produced a $Gd_2(OH)_2CO_3SO_4 \cdot H_2O$ new compound (GOCSH) that was crystallized in the tetragonal system (space group $P\text{-}42_1m$) with a layered structure along the [001] crystallographic direction. Furthermore, macroscopically and microscopically uniform GOSCH:Ln films, constructed by vertical self-alignment of platelike crystallites, were successfully fabricated by applying heterogenous nucleation on quartz substrate. Taking the advantage of the exactly the same S/(Gd,Ln) molar ratio, $Gd_2O_2SO_4$:Ln and Gd_2O_2S:Ln films of the same microstructures were then derived from the GOSCH:Ln films by annealing in air and hydrogen at 800 °C, respectively, without any additional sulfurization. The mechanism of film formation and the influence of deposition/annealing temperature on film quality were discussed. Aside from luminescence, the films all have microstructure-enabled super-hydrophobicity and are transparent in the visible light region (~70-93%). The multi-functional films, particularly those of Gd_2O_2S:Ln, may find potential application in luminescence, display, scintillation and microimaging.

***Keywords**:* Oriented film; Precursor; Gd_2O_2S; Luminescence; Super-hydrophobicity

1. Introduction

The phosphors developed by doping Gd_2O_2S with Pr^{3+}, Eu^{3+} and Tb^{3+} (Gd_2O_2S:Ln) are well known for their bright green, red and green emissions, respectively, and are finding wide applications in photoluminescence (PL), cathodoluminescence (CL) and X-ray excited luminescence (XEL), because Gd_2O_2S has the advantage of wide bandgap (~4.6-4.8 eV), high radiation harness (theoretical density ~7.34 g/cm^3), low phonon energy (~520 cm^{-1}), satisfactory stability and efficient excitation absorption [1, 2]. The most matured and commercialized technology to synthesize Gd_2O_2S:Ln and other rare-earth (RE) oxysulfides (RE_2O_2S) is flux reaction, which involves reacting an RE oxide/carbonate with elemental sulfur/sodium thiosulfate ($Na_2S_2O_3$) in an alkali carbonate/halide flux at 1200-1300 ºC for several hours, followed by acid washing [3]. The technique has the advantage of well crystallized particles (micron level) but raises environmental concern because of its toxic byproducts (such as H_2S and SO_x gases). Because of the high melting point of Gd_2O_2S (~2200 ºC) and the large particle size/low activity of the powder, the fabrication of Gd_2O_2S:Ln ceramic scintillator, which is being widely applied for X-ray computed tomography (X-CT), requires harsh sintering conditions, such as a temperature as high as ~1750 ºC for atmosphere-controlled sintering and typically ~1300-1500 ºC and meanwhile tens to hundreds MPa of an applied pressure for pressure assisted sintering [4, 5]. Sulfidizing a precursor with H_2S or CS_2 gas [6, 7] or combustion with thiourea as the sulfur source [8] may produce nanocrystalline RE_2O_2S, but is difficult to control over phase/chemical purity since sulfur is much less affinitive than oxygen toward RE. Aside from three-dimensional bulks, thin-film scintillators are drawing remarkable attention over the recent years for device miniaturization and for X-ray or electron microimaging with high spatial sub-micrometer resolution [9-11].

Up to date, thin-film scintillators have been successfully fabricated by gas phase condensation and/or liquid phase epitaxy in moten salt for CsI:Tl and Ln^{3+} (Ln = Ce, Pr, Eu, Tb) activated RE_2O_3 sesquioxide, $REAlO_3$ perovskite, $RE_3Al_5O_{12}$ garnet and RE_2SiO_5 orthorsilicate, where RE^{3+} is typical of Y^{3+}, Gd^{3+} or Lu^{3+} [9-11]. Our thorough literature survey, however, indicated that Gd_2O_2S:Ln has not been prepared in the thin-film form due to its special composition. Pulsed laser deposition (PLD), for example, was attempted for Gd_2O_2S deposition, but the film product contained an oxide impurity [12].

The recent appearance of $RE_2(OH)_4SO_4{\cdot}nH_2O$ layered hydroxide (SO_4^{2-}-LREH; RE = La-Lu lanthanide or Y) provided a unique opportunity for wide-spectrum green synthesis of RE_2O_2S [13, 14]. This is because the compound is readily obtainable by titrating an aqueous solution containing RE^{3+} and SO_4^{2-} with ammonium hydroxide to a certain pH value followed by hydrothermal crystallization, and the compound directly dehydrates to RE_2O_2S upon being heated in a reducing atmosphere such as hydrogen ($RE_2(OH)_4SO_4{\cdot}nH_2O + 4H_2 \rightarrow RE_2O_2S + (6+n)H_2O$) [13, 14]. Such a technical route, unfortunately, cannot be directly applied to film fabrication since titration, like most other precipitation reactions, is featured by localized fast nucleation of the solid phase in an uncontrollable manner, and one cannot confine nucleation to a designated place such as the substrate for film growth. Nevertheless, it is well documented in the literature that employing an ion-reservoir is effective for nucleation control, where the reservoir releases the precipitation-participating cation or anion in a controllable way under a certain condition such as heating [15, 16]. One classic example of great success is the urea-based homogeneous precipitation of amorphous $RE(OH)CO_3{\cdot}nH_2O$, where the OH^- and CO_3^{2-} anions were released by the *in situ* hydrolysis of urea above ~83 °C [17, 18]. The slow supply of anions allows spontaneous nucleation to occur via one-single burst in the

whole reaction system, and $RE(OH)CO_3 \cdot nH_2O$ monospheres can then be generated via subsequent uniform growth of the nuclei [15, 19].

In view of the above, we conducted hydrothermal reaction for the $Gd(NO)_3$-$(NH_4)_2SO_4$-urea ternary system in this work, and obtained a $Gd_2(OH)_2CO_3SO_4 \cdot nH_2O$ new compound (GOCSH) with chemical composition midway between those of the aforesaid $RE_2(OH)_4SO_4 \cdot nH_2O$ (SO_4^{2-}-LREH) and $RE(OH)CO_3 \cdot nH_2O$ (that is, $RE_2(OH)_2(CO_3)_2 \cdot 2nH_2O$). Preliminary analysis of crystal structure indicated that the compound was crystallized in the tetragonal system (space group *P*-42$_1$*m*) with a layered structure along the [001] crystallographic direction. More importantly, macro-/microscopically uniform GOSCH:Ln films consisting of vertically aligned platelike crystallites were successfully obtained by applying heterogenous nucleation on quartz substrate, which were then transformed into $Gd_2O_2SO_4$:Ln and Gd_2O_2S:Ln films of the same microstructure by subsequent annealing in air and hydrogen, respectively. The spectral features of the doped Ln ions were analyzed in detail, and further investigation found that all the films have microstructure-enabled super-hydrophobicity (water contact angle above 150°) and are transparent in the visible light region (~70-93%). The multi-functional films, especially those of Gd_2O_2S:Ln, were expected to have potential application for luminescence, display, scintillation and microimaging. In the following sections, we report the detailed synthesis and characterization of the materials.

2. Experimental Section

2.1. Reactants and synthesis

The 99.99% pure RE oxides of Pr_6O_{11}, Eu_2O_3, Gd_2O_3 and Tb_4O_7 were provided by Huizhou Ruier Rare-Chem. Hi-Tech. Co. Ltd (Huizhou, China), and analytical grade ammonium

sulfate ($(NH_4)_2SO_4$), urea ($CO(NH_2)_2$) and nitric acid (HNO_3, 65-68 wt%) were purchased from Sinopharm Chemical Reagent Co. Ltd (Shanghai, China). Ultrapure water (resistivity > 18 MΩ·cm) was used throughout the experiments. The nitrate solution of RE^{3+} was prepared by dissolving the corresponding oxide with a proper amount of nitric acid, followed by dilution.

For the synthesis of precursor powder, an aqueous solution (60 mL) containing 3 mmol of Gd^{3+}, 2 mmol of $(NH_4)_2SO_4$ and 2 mmol of $CO(NH_2)_2$ was transferred into a Teflon-lined stainless steel autoclave of 100 mL capacity, followed by hydrothermal reaction at 140 °C for 12 h in a preheated electric oven. After natural cooling to room temperature, the precipitate was collected via centrifugation, washed with water 3 times and ethanol twice, and then dried at 60 °C for 12 h. For the preparation of precursor films, the aforesaid solution was preheated at ~85 °C until pH reached ~5.8 before hydrothermal treatment. Such an operation was found vital to the growth of a uniform film, as it may allow the precipitation-participating OH^- and CO_3^{2-} anions, released via the hydrolysis of urea, to accumulate to a critical concentration level for fast heterogeneous nucleation. The quartz substrate (2.5 cm×7.5 cm×0.1 cm) for film growth was ultrasonically cleaned with water and ethanol for 5 min sequentially, dried with blowing air, and was then immersed into the pretreated reactant solution at an inclination angle of ~65° in the autoclave. After hydrothermal reaction at a predetermined temperature for 12 h, the substrate was taken out of the autoclave, washed with water and ethanol in turn, and then dried with blowing air. The precursor films separately doped with 1 at.% of Pr^{3+}, 5 at.% of Eu^{3+} and 2 at.% of Tb^{3+} were produced by the above procedures, where the doping levels were taken according to previous reports [6, 20, 21]. $Gd_2O_2SO_4$:Ln films (Ln = Pr, Eu, Tb) were derived by annealing their precursor films in stagnant air at 800 °C for 1 h, and

Gd_2O_2S:Ln films were obtained by annealing the above $Gd_2O_2SO_4$:Ln films in flowing H_2 (100 mL/min) at 800 °C for another 1 h. In both the cases, a heating rate of 8 °C/min was used for the ramp stage of heating.

2.2. Characterization

The elemental contents of the precursor powder were determined for Gd via inductively coupled plasma (ICP) mass spectrometry (detection limit 0.01wt%; Model iCAP Q, Thermo Fisher Scientific, Waltham, USA) and for N, C and S via the inert gas fusion-infrared absorption/thermal conductivity technique (detection limit 0.01wt%; Elementar varioEL cube, Langenselbold, Germany), and the powder for analysis was pre-dried at 60 °C for 24 h. Phase identification was performed via X-ray diffractometry (XRD, Bragg measurement; SmartLab, Rigaku, Tokyo, Japan) using nickel-filtered Cu-Kα radiation (λ= 0.15406 nm) under 40 kV/200 mA, a Model D/teX Ultra line detector and a scanning speed of 4° 2θ/min. The XRD data (Bragg measurement) for structure analysis with TOPAS 4.2 software were collected from powder sample with the above equipment via step-scan over the 2θ range of 5-110°, using a step width of 0.02° and a counting time of 10 s per step. Fourier transform infrared spectroscopy (FTIR, Nicolet iS5, Thermo Fisher Scientific) was conducted using the standard KBr pellet method. Product morphology and microstructure were analyzed by field-emission scanning electron microscopy (FE-SEM, Model JSM-7001F, JEOL, Tokyo) under an acceleration voltage of 15 kV and transmission electron microscopy (TEM, Model JEM-2000FX, JEOL) under 200 kV. Thermogravimetry/differential thermal analysis (TG/DTA, Model SETSYS Evolution-16, Setaram, France) was performed at a constant heating rate of 10 °C/min in flowing simulated air (50 mL/min). Surface wettability of the films was measured on an automatic contact angle goniometer (Model SL200B, KINO, New

York, USA) at ambient temperature. The transmittance spectra of the films were recorded on a Model UV-3600 Plus instrument (Shimadzu, Kyoto, Japan) equipped with a Φ150 mm integrating sphere. Photoluminescence was analyzed with an FP-8600 fluorospectrophotometer (JASCO, Tokyo) equipped with a Φ60 mm integrating sphere (Model ISF-834, JASCO), a 150 W xenon lamp for excitation, a slit width of 5 nm and a scan speed of 100 nm/min for both excitation and emission. The spectral response of the spectrophotometer was corrected with a Rhodamine-B solution (5.5 $g \cdot L^{-1}$ in ethylene glycol) and a standard light source unit (ECS-333, JASCO) for the ranges of 220-600 nm and 350-850 nm, respectively. The fluorescence decay of Eu^{3+} and Tb^{3+} was analyzed with the FP-8600 instrument, while that of Pr^{3+} was measured with a DeltaFlex modular fluorescence lifetime system (HORIBA Scientific, Jobin Yvon IBH Ltd., Scotland) using NanoLED-250 (λ = 249 nm, 1.2 ns pulse duration) for excitation.

3. Results and discussion

3.1 Characterization of the precursor powder

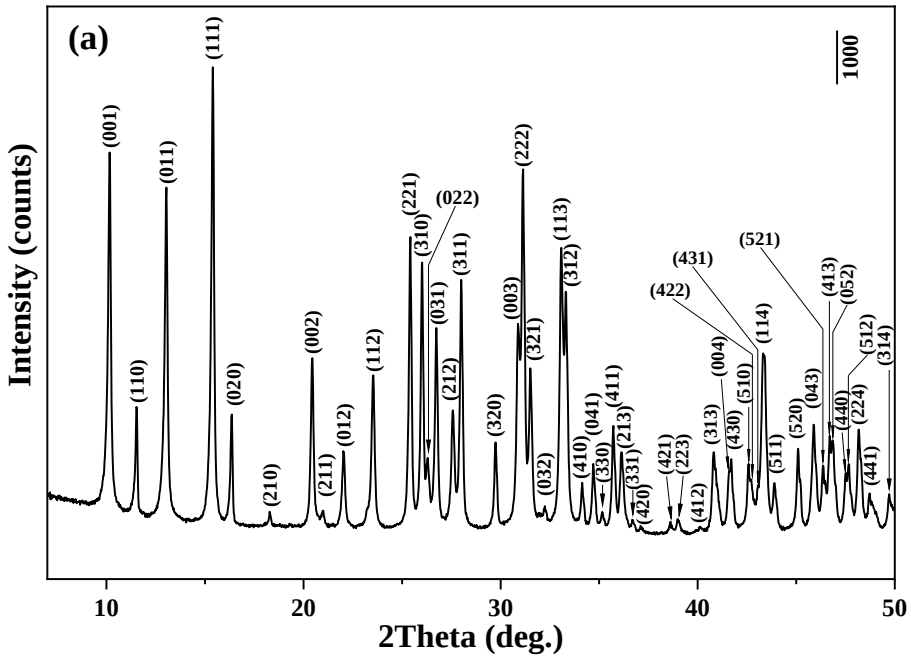

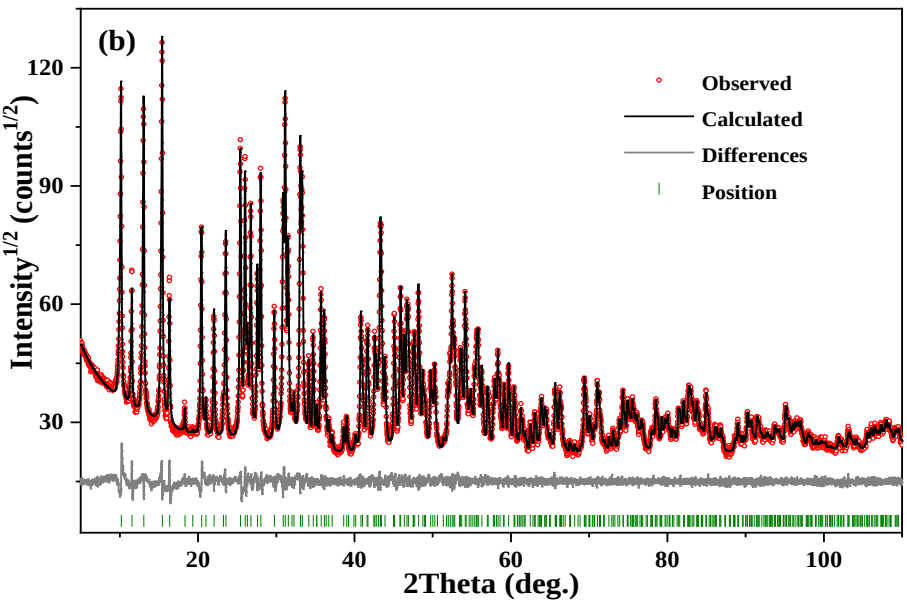

Fig. 1. Indexation of the XRD pattern of precursor powder for 2θ = 5-50° (a) and the results of Pawley refinement of the XRD pattern (b).

XRD analysis indicated that the precursor powder is highly crystalline, as evidenced by the sharp reflections in Fig. 1. Our careful survey, however, showed that the XRD pattern cannot be indexed with any of the Gd-containing compounds in the JCPDS database or literature. FTIR analysis was thus conducted to understand the chemical species contained in this powder, and the results (Fig. 2a) clearly revealed the vibrations arising from OH^- at ~3553 cm^{-1} (O–H stretching, ν_1) [22], from H_2O molecules at ~3420 cm^{-1} (O–H stretching, ν_1)/1645 cm^{-1} (H–O–H bending, ν_2) [22, 23], from CO_3^{2-} at ~840 cm^{-1} (ν_2, weak) and in the regions of ~1390-1590 cm^{-1} (ν_3, strong)/670-808 cm^{-1} (ν_4, medium strong) [22, 24], and from SO_4^{2-} at ~1010 cm^{-1} (ν_1) and in the regions of ~1025-1270 cm^{-1} (ν_3)/583-645 cm^{-1} (ν_4) [22]. With the results of FTIR and in view that the reaction system also contains NH_4^+ (from ammonium sulfate and urea) and NO_3^- (from Gd nitrate), we performed chemical analysis for the Gd, C, S and N key elements and found that the powder contains ~60.82 (±0.01) wt % of Gd, 2.29 (±0.01) wt % of C, 6.20 (±0.01) wt % of S and none of N, which correspond to a Gd:C:S

molar ratio of 2.00:1.01:1.00. The absence of N rules out the potential interference of NO_3^- or NH_4^+ with our assignment of the ν_3 vibration of CO_3^{2-} (~1390-1590 cm^{-1}). Based on the results of chemical analysis and by considering molecular neutrality, the product can thus be deduced to be $Gd_2(OH)_2CO_3SO_4 \cdot nH_2O$, where the number of molecular water (*n* value) was calculated from the formula with the content of Gd to be ~1.0. FE-SEM observation showed that the powder mainly contains hollow spheroids (~3-10 μm in diameter) of interlaced flakes (Fig. 2b), and a closer view (Fig. 2b, the inset) indicated that the edge length of each flake is close to ~2 micrometers while the thickness is a few tens of nanometers.

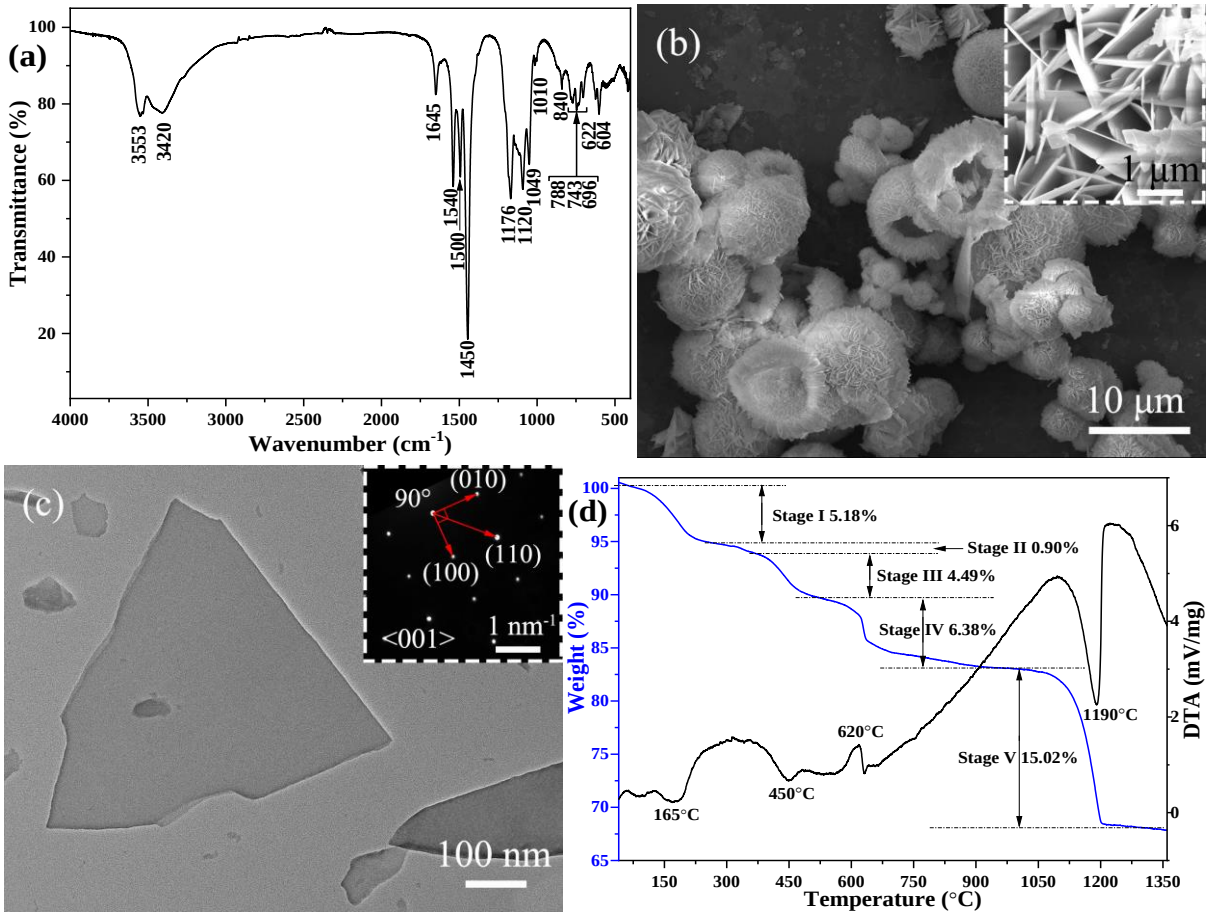

Fig. 2. FTIR spectrum (a), FE-SEM morphology (b), TEM morphology (c) and TG/DTA curves (d) of the precursor powder. The inset in (b) is a closer view and that in (c) is the SAED pattern.

The above results of composition and morphology analysis let us recall the $RE_2(OH)_4SO_4 \cdot nH_2O$ layered hydroxide (SO_4^{2-}-LREH, *n*~0-2.0) reported in recent years [14,

25]. This is because the chemical formula of SO_4^{2-}-LREH can be transformed to the formula of this work if two out of the four OH^- were replaced with one CO_3^{2-}, and the SO_4^{2-}-LREH also tends to crystallize as platelike crystals owing to its layered structure. Furthermore, the XRD pattern in Fig. 1 showed diffractions with *d*-spacing values of ~0.870 nm (2θ ~10.19°) and 0.435 nm (one half of 0.870 nm, 2θ ~20.40°) in the low-angle region. It was thus speculated that the product of this work is a phase-pure compound of layered crystal structure. We used multiple algorithms, including ITO [26], DICVOL [27] and TREOR [28], to index a preliminary cell, and the results all showed that the tetragonal cell with approximate dimensions of a = 10.8211 Å and c = 8.6812 Å has the highest credibility. When indexing the XRD pattern with this cell, all of the diffraction peaks can be well corresponded (Fig. 1a, Table S1). The systematic appearance of 00*l* diffractions further verified that this $Gd_2(OH)_2CO_3SO_4{\cdot}H_2O$ (GOCSH) new compound indeed has a layered crystal structure, which is built up via repetitive stacking along the [001] crystallographic direction. The Pawley refinement was carried out with potential space groups through TOPAS 4.2 software [29], among which the $P\text{-}42_1m$ (No. 113) one showed the highest degree of fit (Fig. 1b, Table 1). Selected area electron diffraction (SAED) from an individual platelike object, disintegrated from the hollow spheres (Fig. 2b) via ultrasonication, yielded a set of well-arranged spots (Fig. 2c and the inset), where the measured *d* spacings of ~5.43/5.44 and 7.67 Å can be assigned to (010)/(100) and (110) planes according to the results of theoretical analysis of the XRD pattern (Table S1), respectively. Furthermore, the (010)/(100) dihedral angle was measured from the SAED pattern to be ~90°, in compliance with the tetragonal structure determined for GOCSH. The results thus indicate that each of the microplates found

via SEM (Fig. 2b) and TEM (Fig. 2c) is single crystalline and was developed by 2D growth perpendicular to the [001] direction (*c*-axis). The layered crystal structure of SO_4^{2-}-LREH presents repetition of the hydroxide main layer, constructed by REO_9 polyhedrons, and interlayer SO_4^{2-} along the [001] direction [30]. While we speculated that the CO_3^{2-} and SO_4^{2-} anions of $Gd_2(OH)_2CO_3SO_4 \cdot H_2O$ assume a similar manner of occurrence, the determination of coordination sphere, atomic position and atomic occupancy is yet underway with the XRD data acquired via synchrotron irradiation.

Table 1. The Results of structure refinement for the $Gd_2(OH)_2CO_3SO_4 \cdot H_2O$ compound.

crystal system	tetragonal
space group	*P*-42$_1$*m*
lattice constant $a = b$ (Å)	10.8153(1)
lattice constant c (Å)	8.6762(1)
cell volume V (Å^3)	1014.8613(3)
R_{wp} (%)	5.05
R_{exp} (%)	2.66
R_p (%)	3.73
χ^2	1.90
R_B (%)	0.26

In Table 1, R_{wp}, R_{exp}, R_p, R_B and χ^2 (defined as R_{wp}/R_{exp}) denote weighted profile reliability factor, expected reliability factor; pattern reliability factor, Bragg reliability factor and goodness of fitting factor of the Rietveld structure refinement, respectively.

The thermal behavior of GOCSH was studied via TG/DTA, and the results are shown in Fig. 2d. It is seen that thermal decomposition proceeds via five distinct stages with a total weight of ~32 wt%, which is very close to the value (~31 wt%) calculated from the $Gd_2(OH)_2CO_3SO_4 \cdot H_2O$ formula. The first stage (Stage I, up to ~260 °C), with an endotherm at ~165 °C, should be caused by the removal of adsorbed/hydration water [25]. Stage Ⅱ to Stage Ⅳ (~260-1000 °C) exhibited a behavior very similar to the sequential and stepwise removal of OH^- and CO_3^{2-} from $Gd(OH)CO_3$ [31]. Stage Ⅴ (~1000-1200 °C), on the other

hand, well corresponds to the desulfuration of $Gd_2O_2SO_4$ to form Gd_2O_3 according to the thermal behavior of SO_4^{2-}-LGdH [32]. To better understand the course of thermal decomposition/phase evolution, XRD (Fig. S1a) and FTIR (Fig. S1b) analyses were conducted on the powders calcined at some typical temperatures determined according to the TG curve. It is seen that the 335 °C product has the same XRD pattern of GOCSH (Fig. S1a) but obviously reduced intensity of OH^- vibration (Fig. S1b), which implies that either dehydration (Stage I, Fig. 2d) or partial dehydroxylation (Stage Ⅱ, Fig. 2d) did not alter the crystal structure to a large extent. A similar phenomenon was also observed for $NH_4Y(MoO_4)_2{\cdot}2H_2O$ [33] and $NaLu(WO_4)_2{\cdot}2H_2O$ [34], and suggests that the water molecules of GOCSH reside at the outer layer of the coordination sphere and are only loosely accommodated. When the temperature reached 450 °C, OH^- absorption and the ν_4 vibration of CO_3^{2-} disappeared while the triple-split ν_3 vibration of CO_3^{2-} became a two-split state. This indicates that the Stage Ⅲ of weight loss corresponds to a synchronous removal of residual OH^- and a part of CO_3^{2-} (endotherm at ~450 °C) and is in line with the decomposition process of most hydroxyl carbonates [31, 35, 36]. It is also due to the dehydroxylation and partial decarbonation that the initial structure of GOCSH collapsed and an amorphous phase was resulted at 450 °C (Fig. S1a). The 620 °C product hardly showed the characteristic vibration of CO_3^{2-}, indicating that stage Ⅳ mainly corresponds to the removal of residual CO_3^{2-}. Meanwhile, each of the ν_3 and ν_4 vibrations of SO_4^{2-} was split into three separate peaks, which is typical of SO_4^{2-} chelating as a trans-bidentate ligand as in $RE_2O_2SO_4$ [25]. This conforms to the crystallization of $Gd_2O_2SO_4$ (exotherm at ~620 °C), as revealed by the corresponding XRD pattern (Fig. S1a). The 1190 °C product only showed Gd–O vibration at

~548 cm^{-1} [22], conforming to desulfuration in Stage V (endotherm at ~1190 °C) and the crystallization of cubic Gd_2O_3 (Fig. S1a). From the above discussion and the weight loss observed for each stage (Fig. 2d), the procedure of GOCSH decomposition can be detailed as follows: (1) $Gd_2(OH)_2CO_3SO_4{\cdot}H_2O \rightarrow Gd_2(OH)_2CO_3SO_4 + H_2O$ (Stage I, up to ~260 °C); (2) $Gd_2(OH)_2CO_3SO_4 \rightarrow Gd_2O_{0.14}(OH)_{1.72}CO_3SO_4 + 0.14H_2O$ (Stage II, ~260-370 °C); (3) $Gd_2O_{0.14}(OH)_{1.72}CO_3SO_4 \rightarrow Gd_2O_{1.25}(CO_3)_{0.75}SO_4 + 0.86H_2O + 0.25CO_2$ (Stage III; ~370-530 °C); (4) $Gd_2O_{1.25}(CO_3)_{0.75}SO_4 \rightarrow Gd_2O_2SO_4 + 0.75CO_2$ (Stage IV; ~530-1000 °C); (5) $Gd_2O_2SO_4 \rightarrow Gd_2O_3 + SO_3$ (Stage V; above 1000 °C). Noteworthy from Fig. S1a is that $Gd_2O_2SO_4$ can be transformed from GOCSH in a wide range of temperature (~620-900 °C), which makes it possible to controllably derive Gd_2O_2S by further annealing in hydrogen.

3.2 Characterization of the precursor films

Fig. 3a shows the XRD patterns of the GOCSH and GOCSH:Ln films formed via 12 h of deposition at 110 °C, with that of the GOCSH powder included for comparison. It is seen that the diffraction patterns conform well to that of the GOCSH powder in each case and the doped Ln^{3+} ions did not affect phase purity. Compared with the powder product, however, the films all showed significantly stronger (110) and (020) diffractions relative to the (001) one. This implies that the films similarly have a preferred orientation, which allowed the (110) and (020) planes to be significantly more exposed to the incident X-ray. In view that both (110) and (020) are perpendicular to (001) in the tetragonal structure of GOCSH, it can thus be concluded that the [001] crystallographic direction of the GOCSH crystallites is parallel to the surface of the quartz substrate. It is interesting to note that such an orientation is just opposite to that of the films self-assembled from the platelike crystallites of $RE_2(OH)_5A{\cdot}nH_2O$ layered

hydroxide (A^--LREH; A^- = NO_3^- or Cl^-) or the nanosheets exfoliated from A^--LREH crystallites, where the objects are lying flat on the substrate and have strong [001] orientation [37-39].

FE-SEM observation indicates that all the film products of Fig. 3a are almost identical in morphology and, therefore, that of GOCSH is shown in Fig. 3b for example. It is evident that the film has a porous and macroscopically uniform microstructure formed by interlacing of vertically aligned GOCSH platelets, in agreement with the crystallite orientation predicted from the XRD patterns (Fig. 3a). Observation under higher magnification (Fig. 3b, the inset) found that the mean edge length and thickness of the flakes are ~2.0 μm and ~170 nm, respectively, and the pore size of the porous structure is up to ~1 μm (average size ~ 0.7 μm). Cross-sectional observation of the film (Fig. 3c) intuitively showed vertical growth of the GOCSH flakes and a film thickness of ~2 μm.

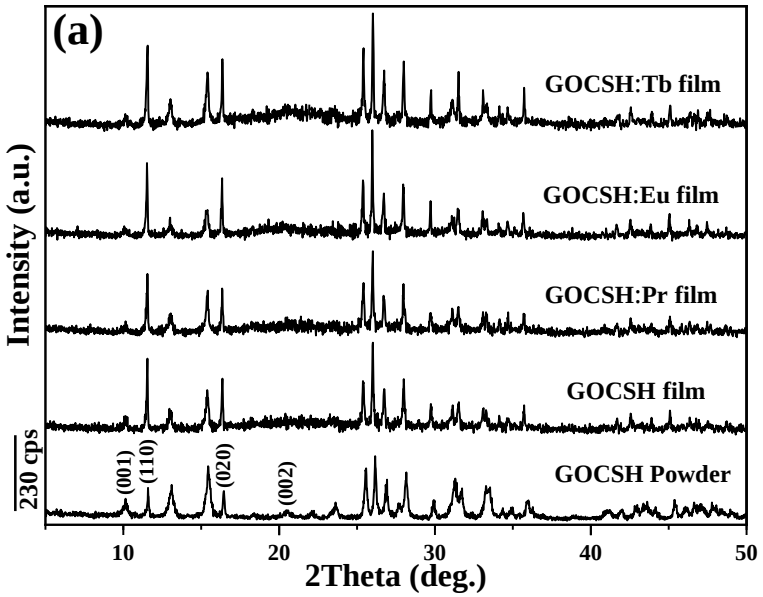

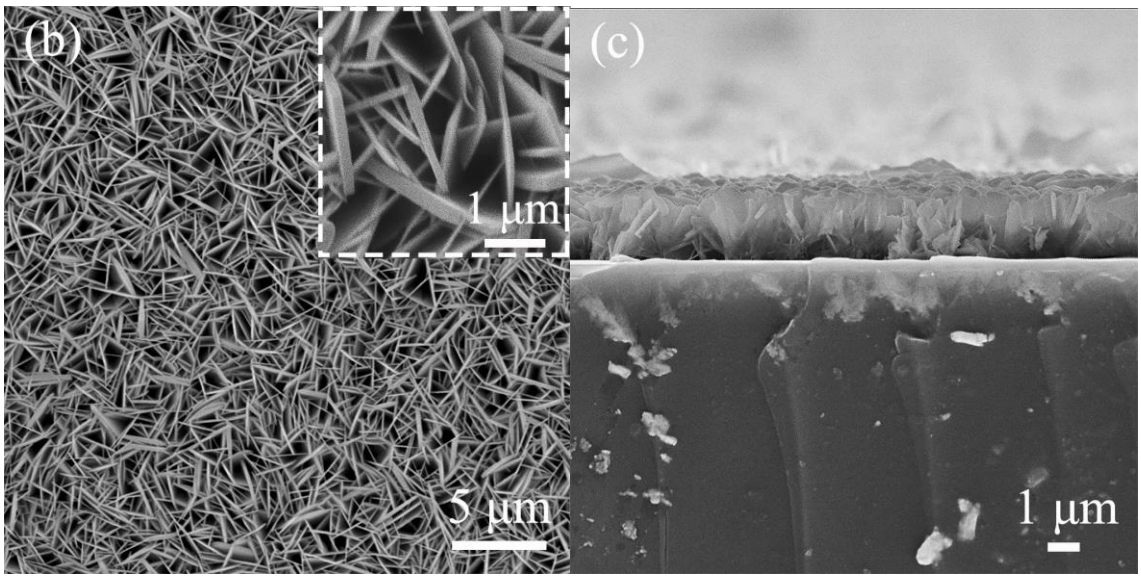

Fig. 3. XRD patterns of the precursor films deposited at 110 °C, with that of the GOCSH powder included for comparison (a), and FE-SEM morphologies of the GOCSH film observed from the surface (b) and cross section (c). The inset in (b) is a closer view.

To understand the mechanism of film formation, we tracked the time-course morphology development of the GOCSH film via FE-SEM and found a typical process of heterogeneous nucleation and crystallite growth (Fig. 4a-d). After only 30 min of reaction, the surface of the substrate has been sparsely distributed with flower-like clusters of GOCSH flakes (Fig. 4a). The rapid formation of such clusters may be explained by considering that heterogeneous nucleation at the high-energy site provided by the substrate would make the surrounding environment also be in a high-energy state for further nucleation due to the creation of a new interface. As a consequence, nucleation continues at around each of the formed nuclei, leading to the formation of a cluster. The increasing number of clusters and increasing size of the existing clusters with prolongation of the deposition reaction would eventually cause the adjacent clusters to merge, and thus a film covering the whole substrate surface was formed (Fig. 4b-d). The vertical growth of GOCSH flakes (Fig. 3b) is primarily driven by two factors. One is minimization of surface free energy. The (001) crystal plane of GOCSH, where Gd is

accommodated, has the lowest surface energy as in the cases of A^{-}-LREH and SO_4^{2-}-LREH [30, 40, 41], which makes crystal growth along the [001] direction the hardest to proceed according to the Wulff theorem. This is the primary reason for the two-dimensional (2D) development of GOCSH crystallites with exposed (001) facets. Clearly, vertical growth helps to maximize the exposure of low energy (001) and meanwhile minimize the exposure of high energy (*hk*0) planes. Secondly, the consumption by nucleation and crystallite growth tends to deplete the solutes (Gd^{3+}, SO_4^{2-}, OH^{-} and CO_3^{2-}) at the site where these events take place, and further growth needs mass transfer. In this regard, the directional diffusion of solutes toward the growth forefront (substrate direction) may have guided the GOCSH crystallites to develop vertically.

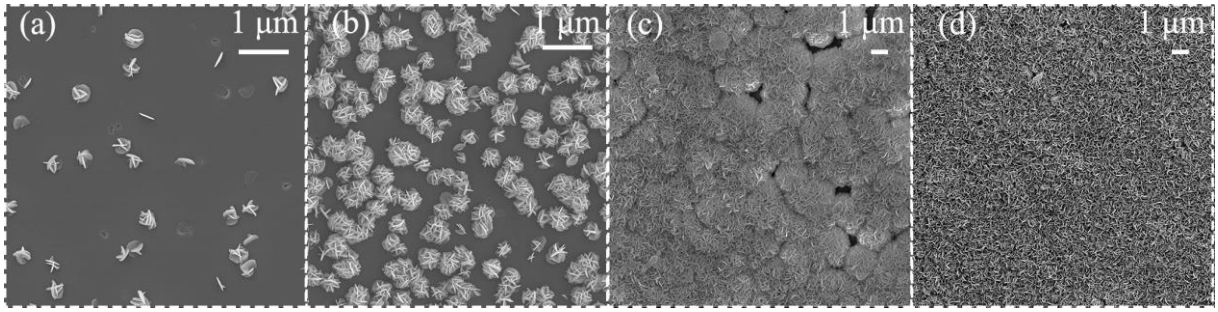

Fig. 4. FE-SEM morphologies of the GOCSH films after deposition at 110 °C for 30 min (a), 60 min (b), 90 min (c) and 120 min (d).

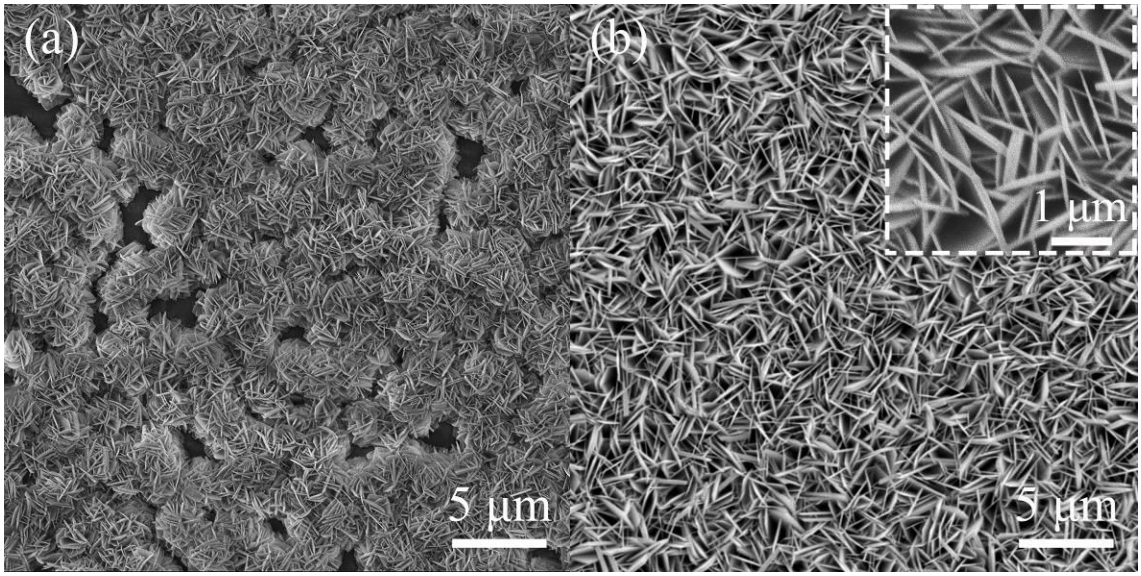

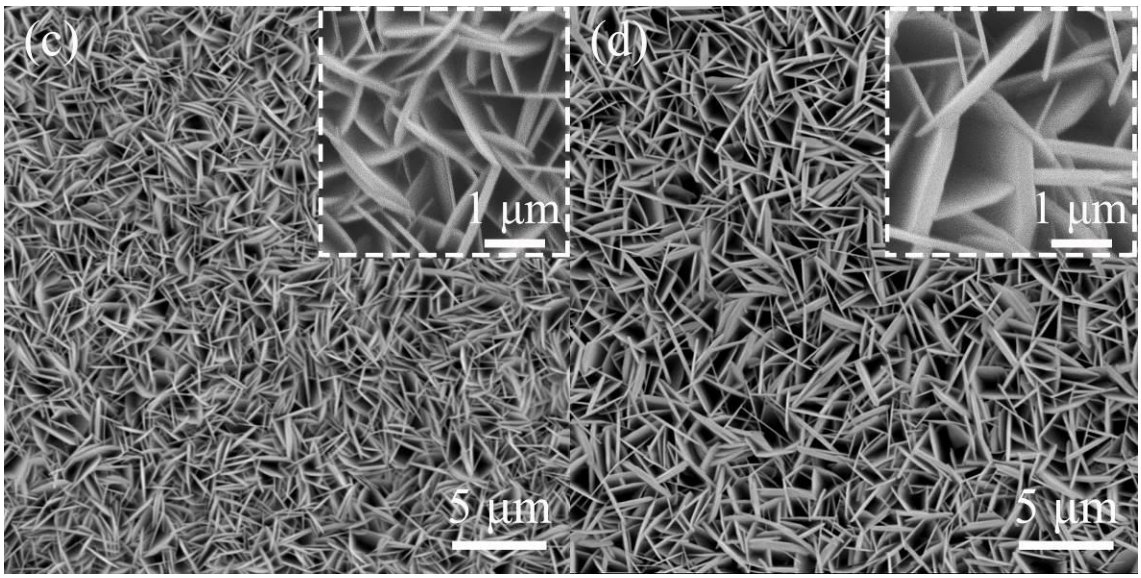

Fig. 5. FE-SEM morphologies of the GOCSH films prepared at 100 ℃ (a), 120 ℃ (b), 130 ℃ (c) and 140 ℃ (d). The insets in (b), (c) and (d) are closer views.

It was also found via FE-SEM that deposition temperature significantly affects the integrity and microstructure of the film, aside from the size of the individual GOCSH crystallites. It is seen form Fig. 5a that the 100 °C film is featured by large voids and incomplete integration of adjacent clusters, which is owing to low nucleation density and insufficient cluster growth. Additionally, the GOCSH platelets were averaged to be ~1 μm and 100 nm in edge length and thickness, respectively. Macroscopically uniform and continuous films were resulted by deposition in the range of 110-140 °C, among which the 110 °C (Fig. 3b), 120 °C (Fig. 5b) and 130 °C (Fig. 5c) ones showed high similarities in terms of pore size (~0.7 μm in average) and dimension of the GOCSH platelets (lateral size ~2.0 μm, thickness ~170 nm). Larger pores (~1.0 μm) and GOCSH crystallites (edge size ~3.0 μm, thickness ~240 nm) were observed for the 140 °C film (Fig. 5d) and this is mainly due to enhanced Ostwald ripening, through which smaller GOCSH crystallites disappeared to create bigger pores and meanwhile larger crystallites grew up at the expense of the smaller ones. Noteworthy is that overgrowth of the GOCSH flakes would weaken film adhesion to the substrate and the film tends to fall off. Therefore, the Ln^{3+} doped GOCSH films were all prepared by 110 °C deposition (Fig. 3a).

3.3 Characterization of the $Gd_2O_2SO_4$:Ln and Gd_2O_2S:Ln films

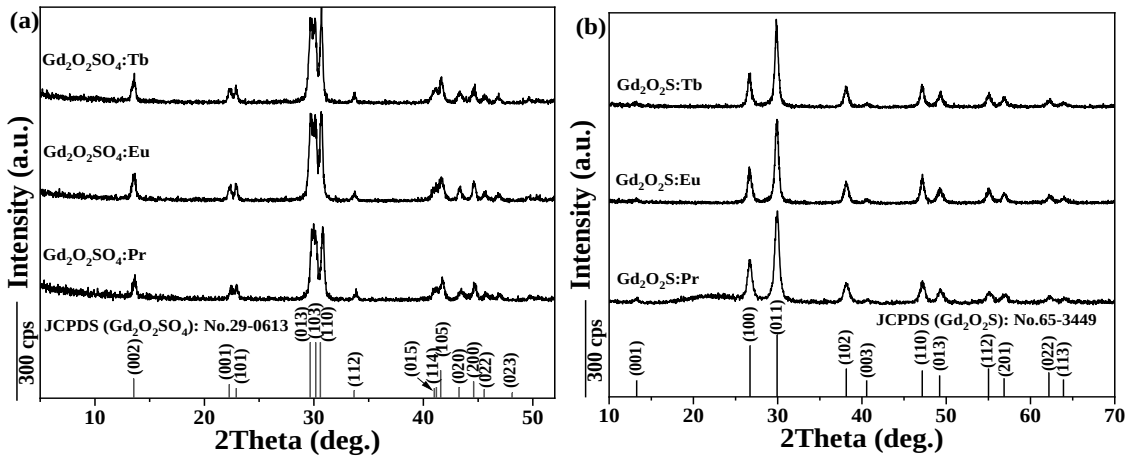

Fig. 6. XRD patterns of the products obtained by annealing the GOCSH:Ln films at 800 °C in air (part a) and in H_2 (part b).

XRD analysis (Fig. 6a) indicated that the products obtained by annealing the GOCSH:Ln films in air at 800 °C well conform to the orthorhombic $Gd_2O_2SO_4$ standard (JCPDS No. 29–0613), which is consistent with the course of phase evolution shown in Fig. S1a. Further annealing the $Gd_2O_2SO_4$:Ln products in flowing hydrogen at 800 °C for another 1 h produced Gd_2O_2S:Ln (Fig. 6b), since in each case the diffraction peaks can be fully indexed with those of the hexagonal Gd_2O_2S standard (space group *P*-3*m*1; JCPDS No. 65–3449).

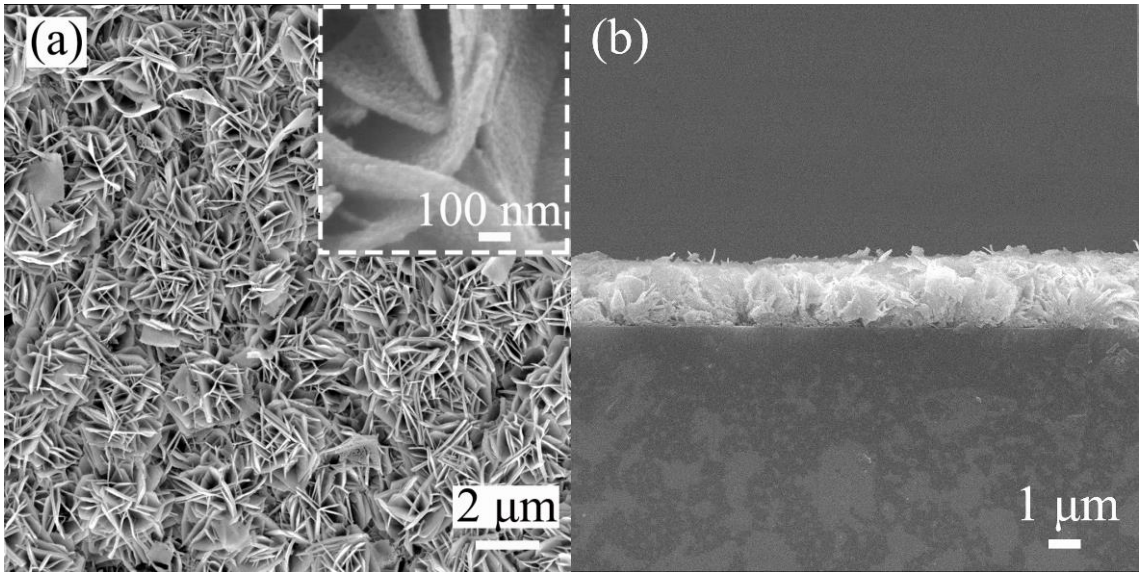

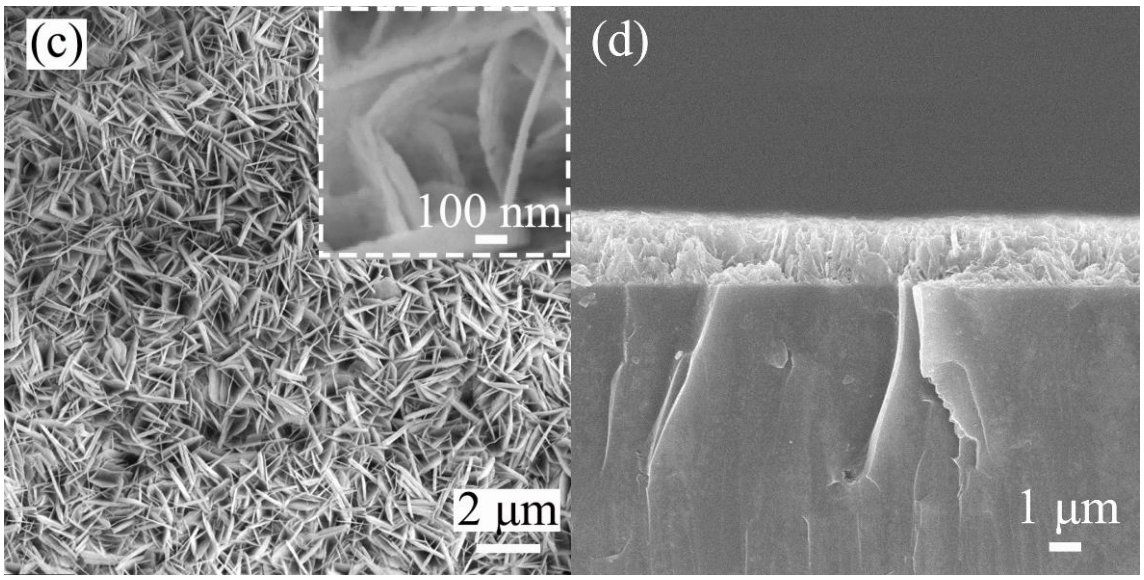

Fig. 7. FE-SEM morphologies of the 800 °C annealed $Gd_2O_2SO_4$:Eu (a, b) and Gd_2O_2S:Pr (c, d) films, where the insets in (a) and (c) are closer views.

Fig. 7 shows the FE-SEM microstructures of the calcination products, with $Gd_2O_2SO_4$:Eu (Fig. 7a,b) and Gd_2O_2S:Pr (Fig. 7c,d) as typical examples. It is seen from either surface view (Fig. 7a,c) or cross-section view (Fig. 7b,d) that they well preserved the structural features of the GOCSH film (Fig. 3b,c). Owing to the mass loss (release of H_2O and CO_2) and nucleation of new phase in the parent phase during annealing, however, each of the original GOSCH:Ln flakes (single crystalline) was transformed into a polycrystalline aggregate (Fig. 7a,c, the insets). GOSCH, $Gd_2O_2SO_4$ and Gd_2O_2S present high structural similarities and are all layered along the *c*-axis, with the anions (SO_4^{2-}, CO_3^{2-}, S^{2-}) sandwiched between the main layers built up of Gd-O polyhedrons [42, 43]. This allows phase transformation to proceed in a quasi-topotactic way [37, 44], which helps to maintain the morphology of the individual flake and the film through minimization of mass diffusion and phase-transition stress. Broadening analysis of the XRD peaks (Fig. 6) with Scherrer formula [45] found average crystallite sizes of ~28 and 15 nm for all the $Gd_2O_2SO_4$:Ln and Gd_2O_2S:Ln films annealed at 800 °C, respectively, irrespectively of the type and content of Ln. Though high-temperature

annealing helps to improve product crystallinity for a better luminescence, the Gd_2O_2S:Ln films obtained at 900 and 1000 °C have macropores/cracks and tend to peel off from the substrate due to the shrinkage stress arising from sintering/densification (Fig. S2).

3.4 Optical properties of the $Gd_2O_2SO_4$:Ln and Gd_2O_2S:Ln films

Fig. 8 shows the PLE and PL spectra of the $Gd_2O_2SO_4$:Eu and $Gd_2O_2SO_4$:Tb films. For $Gd_2O_2SO_4$:Eu (Fig. 8a), the PLE spectrum obtained by monitoring the red emission at 617 nm contains a broad and strong band at ~275 nm and also a few negligibly weak sharp peaks in the longer wavelength region for the intra-4f^6 transition of Eu^{3+}. The broad band should be overlapped from O^{2-}-Eu^{3+}charge transfer (CT, excitation of electrons from the 2*p* orbital of O to the 4*f* orbital of Eu) and the $^8S_{7/2} \rightarrow {}^6I_J$ excitation transition of Gd^{3+} [46], as the latter clearly appeared in the PLE of $Gd_2O_2SO_4$:Tb (Fig. 8b). The PL spectrum obtained under 275 nm excitation exhibited the typical $^5D_0 \rightarrow {}^7F_J$ (J = 0-4) emissions of Eu^{3+}, with the $^5D_0 \rightarrow {}^7F_2$ red one (~617 nm) being the most prominent. For $Gd_2O_2SO_4$:Tb (Fig. 8b), the PLE spectrum recorded by monitoring the 545 nm green emission showed four sharp bands in the ~200-350 nm region, with the ~209 nm one for host excitation, the 228 nm dominant one for spin-allowed $4f^8 \rightarrow 4f^75d^1$ intra-configurational transition of Tb^{3+}, and the ~275 and 312 nm ones for $^8S_{7/2} \rightarrow {}^6I_J$ and $^8S_{7/2} \rightarrow {}^6P_J$ intra-$4f^7$ transitions of Gd^{3+}, respectively. Under 228 nm excitation, the film showed luminescence via transition from the $^5D_3$ and $^5D_4$ excited states to ^7F_J (J = 3–6) ground multiplets of Tb^{3+}, as labeled in the figure, with the $^5D_4 \rightarrow {}^7F_5$ green emission at ~545 nm being overwhelmingly strong. The Eu^{3+} and Tb^{3+} doped $Gd_2O_2SO_4$ films were analyzed from their PL spectra to have quantum yields (QYs) of ~32.5 and 20.2% and Commission Internationale de L'Eclairage (CIE) chromaticity coordinates of around (0.650, 0.350) and (0.287, 0.482), respectively. The red (Eu^{3+}) and green (Tb^{3+}) luminescence can be

seen from the CIE diagram (Fig. S3a) and digital pictures (Fig. 8, the insets). Fluorescence decay analysis found that the main luminescence of Eu^{3+} (λ_{em} = 617 nm, λ_{ex} = 275 nm) and Tb^{3+} (λ_{em} = 545 nm, λ_{ex} = 228 nm) both decreased in a single exponential manner and has lifetime values of 1.77±0.01 ms and 2.82±0.02 ms, respectively (Fig. S4a). No data, however, are available from the literature for quantum yield and lifetime comparison. Noteworthy is that the $Gd_2O_2SO_4$:Pr film is hardly luminescent. In view that Pr^{3+} is even slightly less oxidizable than Tb^{3+} in either solution or crystal [47], the possible oxidation by calcination in air was ruled out. It was thus believed that the quenching of Pr^{3+} luminescence is due to placement of the $4f^15d^1$ excited energy level of Pr^{3+}, which is sensitive to crystal field and lattice covalency [48], in the conduction band of $Gd_2O_2SO_4$.

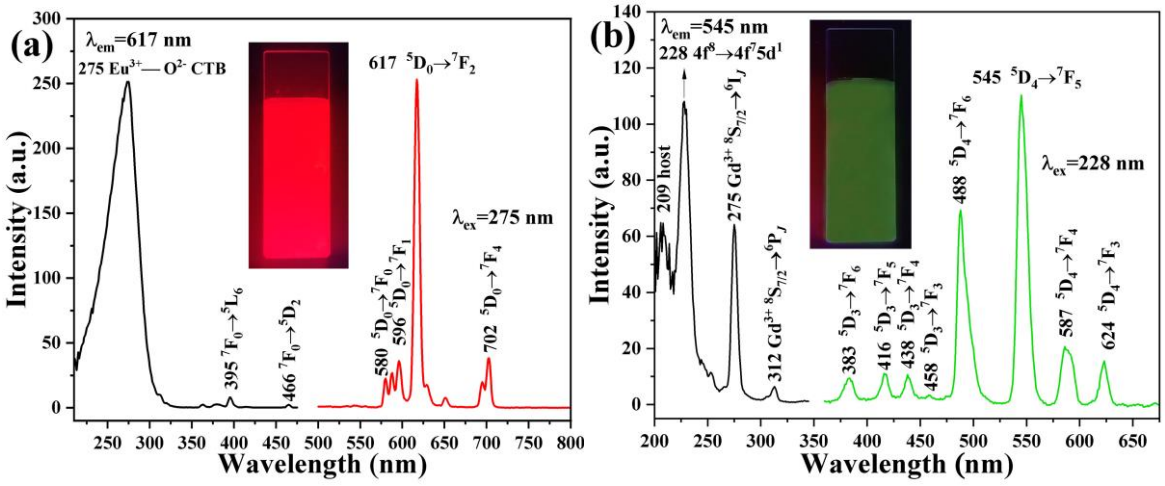

Fig. 8. PLE (left) and PL (right) spectra of the $Gd_2O_2SO_4$:Eu (a) and $Gd_2O_2SO_4$:Tb (b) films. The insets are digital photographs taken for the appearance of luminescence under 254 nm UV irradiation.

Fig. 9 shows the photoluminescence of the Gd_2O_2S:Ln films. From the PLE spectra taken by monitoring the strongest emission of the corresponding activator ion, which is ~513 nm for Pr^{3+}, ~626 nm for Eu^{3+} and ~545 nm for Tb^{3+}, it is seen that the $4f^2 \rightarrow 4f^1d^1$ inter-configurational transition of Pr^{3+} at ~302 nm (Fig. 9a), O^{2-}/S^{2-}-Eu^{3+} CT (simultaneous excitation of O 2*p* and S 3*p* electrons to the 4*f* orbital of Eu) at ~329 nm (Fig. 9b) and the

low-spin $4f^8 \rightarrow 4f^75d^1$ inter-configurational transition of Tb^{3+} at ~286 nm (Fig. 9c) are the most efficient excitation sources. Besides, the $^8S_{7/2} \rightarrow {}^6I_J$ excitation of Gd^{3+} (~275 nm) appeared in each of the excitation spectra, indicating the presence of energy transfer from Gd^{3+} to the activator ions [49-51]. In view that the bandgap energy of Gd_2O_2S is ~4.6-4.8 eV (~258-270 nm), the ~268 nm peak in the PLE of Pr^{3+} can then be assigned to host excitation (Fig. 9a). Such a peak should also exist in the other two cases but is not clearly identifiable owing to spectral overlapping. It is seen by comparing the PLE spectra of Fig. 8 and Fig. 9 that the CT band of Eu^{3+} and the $4f^8 \rightarrow 4f^75d^1$ transition of Tb^{3+} in Gd_2O_2S were significantly re-shifted, which is owing to increased lattice covalency by partially replacing O ligands (electronegativity χ=3.44) with remarkably less electronegative S (χ=2.58) for Gd coordination (GdO_6 trigonal prism in $Gd_2O_2SO_4$ and mono-capped GdO_4S_3 polyhedron in Gd_2O_2S) [42, 43]. Under excitation with the aforementioned wavelengths, the three films produced sharp green (Pr^{3+}, ~513 nm), red (Eu^{3+}, ~626 nm), and green (Tb^{3+}, ~545 nm) emissions, as seen from the photographs taken for the appearance of luminescence (Fig. 9d). In each case, the other emissions are arising from intra-4*f* transitions of the activator ion, as labelled in the corresponding PL spectrum. The Gd_2O_2S:Pr, Gd_2O_2S:Eu, and Gd_2O_2S:Tb films were analyzed from their PL spectra to have QYs of ~24.7, 22.3, and 27.9% and CIE color coordinates (Fig. S3b) of about (0.147, 0.567), (0.644, 0.352) and (0.306, 0.562), respectively. The QY of Gd_2O_2S:Pr film is close to the 25.1% reported for its powder form [52], and those of Gd_2O_2S:Eu and Gd_2O_2S:Tb are remarkably larger than the values reported for the $(Gd_{0.975}Eu_{0.025})_2O_2S$ (~7.7%) and $(Gd_{0.975}Tb_{0.025})_2O_2S$ (~14.6%) powders obtained by sulfurization of solvothermal precursors in a N_2/S atmosphere [53]. The dominant

luminescence of the Gd_2O_2S:Ln films was also found to decay single-exponentially (Fig. S4b,c), and has a lifetime of 2.66±0.02 μs for Pr^{3+} (λ_{em} = 513 nm, λ_{ex} = 249 nm), 0.67±0.01 ms for Eu^{3+} (λ_{em} = 626 nm, λ_{ex} = 329 nm) and 1.21±0.01 ms for Tb^{3+} (λ_{em} = 545 nm, λ_{ex} = 286 nm). The values are in reasonable agreement with those reported for the corresponding Gd_2O_2S:Ln powders, which are ~2.36-6.73 μs for Pr^{3+} [52, 54], ~0.45-0.7 ms for Eu^{3+} [43, 53, 55] and ~0.78-1.34 ms for Tb^{3+} [53, 56].

Eu^{3+} occupies the low-symmetric C_1 and C_{3v} sites of Gd^{3+} in $Gd_2O_2SO_4$ and Gd_2O_2S, respectively, and therefore the parity forbidden $^5D_0 \rightarrow {}^7F_2$ electric dipole transition is stronger than the parity allowed $^5D_0 \rightarrow {}^7F_1$ magnetic dipole transition in both the cases [57]. The $I(^5D_0 \rightarrow {}^7F_2)/I(^5D_0 \rightarrow {}^7F_1)$ intensity ratio, however, is different for the two types of films, which is ~7.00 for $Gd_2O_2SO_4$:Eu and ~8.52 for Gd_2O_2S:Eu. In view that C_1 is lower than C_{3v} and the two films have almost identical structures, the lager intensity ratio of Gd_2O_2S:Eu may thus mainly be due to smaller grain size (~15 nm, ~28 nm for $Gd_2O_2SO_4$:Eu), which makes more Eu^{3+} reside at lower-symmetric interface sites. Meanwhile, the $^5D_3 \rightarrow {}^7F_J$ emission of Tb^{3+} in Gd_2O_2S is much weaker than that in $Gd_2O_2SO_4$, as seen from the $(^5D_4 \rightarrow {}^7F_5)/(^5D_3 \rightarrow {}^7F_5)$ intensity ratio, which is ~32.6 for the former and ~8.6 for the latter. Analysis of the average separation distance (R) of Tb^{3+} with the equation $R \approx 2[3V/(4\pi xN)]^{1/3}$ [58] found a value of ~1.74 nm for $Gd_2O_2SO_4$ and ~1.59 nm for Gd_2O_2S, where V is the volume of the unit cell (~220.5 $Å^3$ for $Gd_2O_2SO_4$ and ~85.7 $Å^3$ for Gd_2O_2S), x is the content of Tb^{3+} (x = 0.02), and N is the number of Gd^{3+} sites in the unit cell (N = 4 for $Gd_2O_2SO_4$ and N = 2 for Gd_2O_2S). It can thus be said that the remarkably larger $(^5D_4 \rightarrow {}^7F_5)/(^5D_3 \rightarrow {}^7F_5)$ ratio of Gd_2O_2S:Tb may mainly be due to more pronounced cross-relaxation via $Tb^{3+}(^5D_3) + Tb^{3+}(^7F_6) \rightarrow Tb^{3+}(^5D_4) +$

Tb^{3+}($^7F_0$) by the smaller *R* value, which reduced the emission from $^5D_3$ and meanwhile enhanced the emission from $^5D_4$.

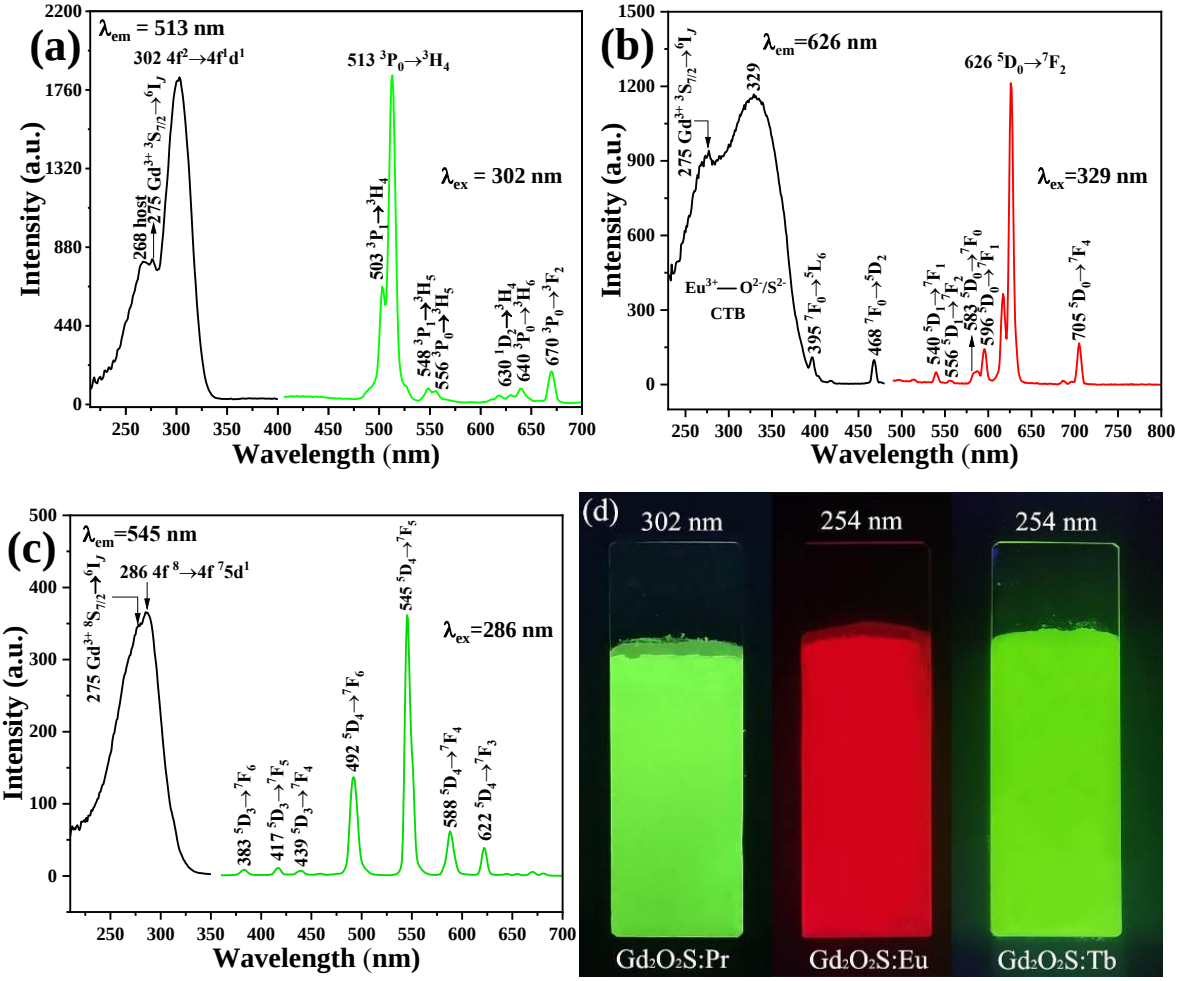

Fig. 9. PLE (left) and PL (right) spectra of the Gd_2O_2S:Pr (a), Gd_2O_2S:Eu (b) and Gd_2O_2S:Tb (c) films. Part (d) is a digital photograph showing the appearance of film luminescence under UV irradiation.

Fig. 10a illustrates the transmittance spectra of representative films in the 200-700 nm spectral region, together with that of the quartz substrate. For GOCSH, the absorption band in the ~240-350 nm region (centered at ~275 nm) should mainly be caused by the $^8S_{7/2} \rightarrow {}^6I_J$ and $^8S_{7/2} \rightarrow {}^6P_J$ transitions of Gd^{3+}, which take place at ~275 and 312 nm, respectively (Fig. 8b), although light scattering by the film itself may also contribute to the band. All the other films showed significantly stronger light absorption in the range of ~240-400 nm, owing to excitation transitions of the doped activator ions and host absorption, and the absorption

profiles are in accordance with their respective PLE spectra (Fig. 8 and Fig. 9a-c). It is also seen from Fig. 10a that all the films are similarly transparent at each wavelength in the visible light region (400-700 nm), which is ~70% at 400 nm and ~93% at 700 nm. The extent of light transmission can be perceived from the photograph shown in Fig. 10b. $Gd_2O_2SO_4$ and Gd_2O_2S would be fully transparent to visible light since the energy of the 400 nm light (~3.1 eV) is remarkably smaller than their bandgap energies. The lower transmittance of these two types of films than bare quartz is thus mainly caused by microstructure-induced light scattering, and the better transparency at a longer wavelength is owing to less scattering of the incident light. This should also be the case for the GOCSH film. The quite similar visible light transmission further imply that the three types of films are close to each other in macro-/microstructure, irrelevant of calcination, conforming to the results of FE-SEM observation (Fig. 3b and Fig. 7).

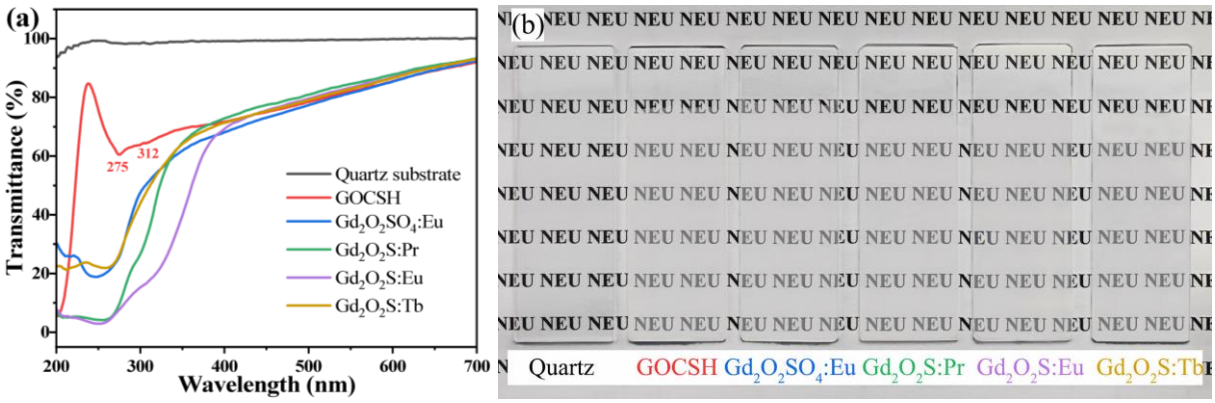

Fig. 10. Transmittance spectra of the typical films and bare quartz (a) and a photograph showing the appearance of light transmission (b).

3.5 Surface wettability of the films

The wettability of a solid surface highly depends on the chemical composition and geometrical feature of the surface, and deliberately creating a micro-/nanostructured porous surface is well known to be an efficient way to achieve super-hydrophobicity [59, 60]. In view

of their morphological structures revealed by FE-SEM (Fig. 3b and Fig. 7), the GOSCH, $Gd_2O_2SO_4$:Eu and Gd_2O_2S:Ln typical films were tested for water wettability and the results are shown in Fig. 11. It is clear that all the films are superhydrophobic, since the water droplet (4 μL) was formed as a sphere on film surface with a contact angle (CA) greater than 150°. In view that RE_2O_2S is generally weaker than its oxide counterpart against water vapor, particularly acidic and alkaline ones, such a water-repellant property may allow a longer stability of Ln^{3+} luminescence. Super-hydrophobicity may be attributed to the roughness of the surface sufficiently amplifying the inherent hydrophobicity of a material according to the Wenzel equation [59], and meanwhile the air trapped in the porous microstructure of the surface may contribute to super-hydrophobicity by increasing the air/liquid interface according to the Cassie-Baxter equation [60]. The latter may have played an essential role in this work, since none of the above compounds is intrinsically hydrophobic.

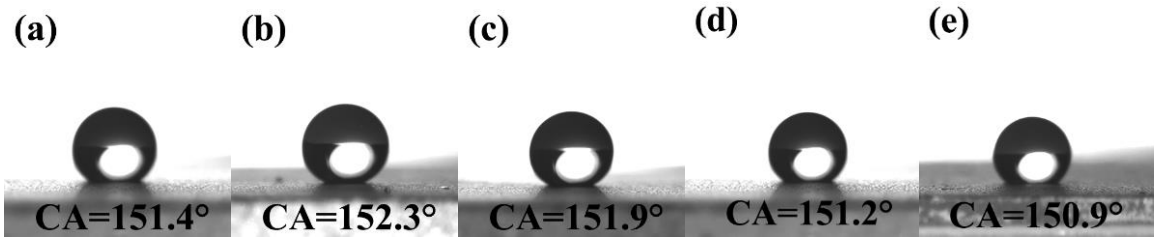

Fig. 11. Water wettability test of the films, with parts (a)-(e) for GOCSH, $Gd_2O_2SO_4$:Eu, Gd_2O_2S:Pr, Gd_2O_2S:Eu and Gd_2O_2S:Tb, respectively.

4. Conclusion

A $Gd_2(OH)_2CO_3SO_4 \cdot H_2O$ (GOCSH) new co*m*pound was obtained in this work via hydrothermally reacting $Gd(NO_3)_3$, $(NH_4)_2SO_4$ and urea, which was found to crystallize in the tetragonal system (space group *P*-42$_1$*m*) with a layered structure along the *c*-axis. With such a reaction system, applying heterogeneous nucleation on quartz substrate produced macro-/microscopically uniform GOSCH:Ln films via vertical self-alignment of platelike

crystallites, and the optimal temperature for film deposition is 110-130 °C. Owing to the exactly the same S/(Gd,Ln) molar ratio, $Gd_2O_2SO_4$:Ln and Gd_2O_2S:Ln films of similar morphological structures were successfully transformed from the GOSCH:Ln films by subsequent annealing in air and hydrogen at 800 °C, respectively, without additional sulfurization. Aside from luminescence, the films have microstructure-induced super-hydrophobicity and are transparent (~70-93%) in the visible light region. The multi-functional films, particularly those of Gd_2O_2S:Ln, may find potential application for luminescence, display, scintillation and micro-imaging.

Acknowledgements

This work was supported in part by the National Natural Science Foundation of China (Grant No. 51972047 and 52172112).

References

[1] C. Greskovich, S. Duclos, Ceramic scintillators, Annu. Rev. Mater. Sci., 27 (1997) 69-88.
[2] B. Ortega-Berlanga, L. Betancourt-Mendiola, C. del Angel-Olarte, L. Hernández-Adame, S. Rosales-Mendoza, G. Palestino, An overview of gadolinium-based oxide and oxysulfide particles: Synthesis, properties, and biomedical applications, Crystals, 11 (2021) 1094.
[3] S. Shionoya, W.M. Yen, H. Yamamoto, Phosphor Handbook, CRC Press, New York, 2018.
[4] W. Wang, H. Kou, S. Liu, Y. Shi, J. Li, Y. Li, X. Feng, Y. Pan, J. Guo, Comparison of the optical and scintillation properties of Gd_2O_2S:Pr,Ce ceramics fabricated by hot pressing and pressureless sintering, Opt. Mater., 42 (2015) 199-203.
[5] M. Yoshida, M. Nakagawa, H. Fujii, F. Kawaguchi, H. Yamada, Y. Ito, H. Takeuchi, T. Hayakawa, Y. Tsukuda, Application of Gd_2O_2S ceramic scintillator for X-ray solid state detector in X-ray CT, Jpn. J. Appl. Phys., 27 (1988) L1572-L1575.
[6] S.A. Osseni, S. Lechevallier, M. Verelst, C. Dujardin, J. Dexpert-Ghys, D. Neumeyer, M. Leclercq, H. Baaziz, D. Cussac, V. Santran, R. Mauricot, New nanoplatform based on $Gd_2O_2S:Eu^{3+}$ core: synthesis, characterization and use for in vitro bio-labelling, J. Mater. Chem., 21 (2011) 18365.
[7] V.V. Bakovets, A.V. Sotnikov, I.V. Korolkov, Kinetics of phase formation in the Ln-O-S (Ln = La, Gd, Y) systems during oxide sulfidation in ammonium thiocyanate vapor, J. Am.

Ceram. Soc., 100 (2017) 1320-1329.
[8] Z. Fu, Y. Geng, H. Chen, S. Zhou, H.K. Yang, J.H. Jeong, Combustion synthesis and luminescent properties of the Eu^{3+}-doped yttrium oxysulfide nanocrystalline, Opt. Mater., 31 (2008) 58-62.
[9] F. Riva, Development of new thin film scintillators for high-resolution X-ray imaging, in, Université de Lyon, 2016.
[10] M. Nikl, Nanocomposite, ceramic, and thin film scintillators, Jenny Stanford Publishing, New York, 2016.
[11] P. Lecoq, A. Gektin, M. Korzhik, Inorganic scintillators for detector systems: Physical principles and crystal engineering, Springer, Berlin, Germany, 2017.
[12] J.J. Dolo, H.C. Swart, J.J. Terblans, E. Coetsee, O.M. Ntwaeaborwa, B.F. Dejene, X-ray photoelectron spectroscopy analysis for undegraded and degraded $Gd_2O_2S:Tb^{3+}$ phosphor thin films, Phys. B, 407 (2012) 1586-1590.
[13] X. Wang, M.S. Molokeev, Q. Zhu, J.-G. Li, Controlled hydrothermal crystallization of anhydrous $Ln_2(OH)_4SO_4$ (Ln=Eu–Lu, Y) as a new family of layered rare earth metal hydroxides, Chem. Eur. J., 23 (2017) 16034-16043.
[14] X. Wang, J.-G. Li, M.S. Molokeev, X. Wang, W. Liu, Q. Zhu, H. Tanaka, K. Suzuta, B.-N. Kim, Y. Sakka, Hydrothermal crystallization of a $Ln_2(OH)_4SO_4{\cdot}nH_2O$ layered compound for a wide range of Ln (Ln = La–Dy), thermolysis, and facile transformation into oxysulfate and oxysulfide phosphors, RSC Adv., 7 (2017) 13331-13339.
[15] T. Sugimoto, Preparation of monodispersed colloidal particles, Adv. Colloid Interface Sci., 28 (1987) 65-108.
[16] E. Matijević, Production of monodispersed colloidal particles, Annu. Rev. Mater. Sci., 15 (2003) 483-516.
[17] E. Matijević, W.P. Hsu, Preparation and properties of monodispersed colloidal particles of lanthanide compounds: I. Gadolinium, europium, terbium, samarium, and cerium(III), J. Colloid Interface Sci., 118 (1987) 506-523.
[18] J.-G. Li, X. Li, X. Sun, T. Ishigaki, Monodispersed Colloidal Spheres for Uniform $Y_2O_3:Eu^{3+}$ Red-Phosphor Particles and Greatly Enhanced Luminescence by Simultaneous Gd^{3+} Doping, J. Phys. Chem. C, 112 (2008) 11707-11716.
[19] E. Matijević, Preparation and properties of uniform size colloids, Chem. Mater., 5 (1993) 412-426.
[20] Y. Zhou, F. Li, X. Wang, Q. Zhu, X. Li, X. Sun, J.-G. Li, Facile synthesis of $Gd_2O_2SO_4$:Tb and Gd_2O_2S:Tb green phosphor nanopowders of unimodal size distribution and photoluminescence, Adv. Powder Technol., 32 (2021) 1911-1919.
[21] Z. Luo, F. Li, Q. Zhu, X. Sun, J.-G. Li, Low-temperature green synthesis of nanocrystalline $La_2O_2S:Pr^{3+}$ powders and investigation of photoluminescence, J. Mater. Res. Technol., 17 (2022) 2540-2549.
[22] J.A. Gadsden, Infrared spectra of minerals and related inorganic compounds, Butterworth, London, 1975.
[23] F. Li, J.-G. Li, Q. Zhu, EDTA-promoted aliovalent Eu^{3+} doping of $Sr_5(PO_4)_3F$ apatite, growth behavior and luminescence, Opt. Mater., 101 (2020) 109765.
[24] H. Qin, X. Zhang, H. Liu, Y. Sang, J. Wang, Mechanism of ammonium sulfate regulation effect on microstructure of Y_2O_3 nanopowders via urea precipitation method,

CrystEngComm, 15 (2013) 5076.
[25] J. Liang, R. Ma, F. Geng, Y. Ebina, T. Sasaki, $Ln_2(OH)_4SO_4 \cdot nH_2O$ (Ln = Pr to Tb; $n \sim 2$): A new family of layered rare-earth hydroxides rigidly pillared by sulfate ions, Chem. Mater., 22 (2010) 6001-6007.
[26] J.W. Visser, A fully automatic program for finding the unit cell from powder data, J. Appl. Crystallogr., 2 (1969) 89-95.
[27] A. Boultif, D. Louër, Indexing of powder diffraction patterns for low-symmetry lattices by the successive dichotomy method, J. Appl. Crystallogr., 24 (1991) 987-993.
[28] P.-E. Werner, L. Eriksson, M. Westdahl, TREOR, a semi-exhaustive trial-and-error powder indexing program for all symmetries, J. Appl. Crystallogr., 18 (1985) 367-370.
[29] G. Pawley, Unit-cell refinement from powder diffraction scans, J. Appl. Crystallogr., 14 (1981) 357-361.
[30] F. Geng, R. Ma, Y. Matsushita, J. Liang, Y. Michiue, T. Sasaki, Structural study of a series of layered rare-earth hydroxide sulfates, Inorg. Chem., 50 (2011) 6667-6672.
[31] M. Hämmer, H.A. Höppe, Crystalline orthorhombic $Ln[CO_3][OH]$ (Ln=La, Pr, Nd, Sm, Eu, Gd) compounds hydrothermally synthesised with CO_2 from air as carbonate source, Z. Naturforsch., 74 (2019) 59-70.
[32] Z. Luo, F. Li, Q. Zhu, X. Li, X. Sun, J.-G. Li, Sulfidization-free synthesis of well dispersed $(Gd,La)_2O_2S:Pr^{3+}$ nanopowders and the effect of La^{3+} on structure and luminescence, J. Mater. Res. Technol., 18 (2022) 4216-4227.
[33] Z. Xu, Q. Zhu, X. Sun, J.-G. Li, A novel precursor route for $Y_2Mo_4O_{15}:Yb^{3+},Ho^{3+}$ phosphor and investigation of up-conversion luminescence, Adv. Powder Technol., 32 (2021) 1276-1286.
[34] X. Shi, J.-G. Li, X. Wang, Q. Zhu, B.N. Kim, X. Sun, Facile hydrothermal crystallization of $NaLn(WO_4)_2$ (Ln=La-Lu, and Y), phase/ morphology evolution, and photoluminescence, Sci. Technol. Adv. Mat., 18 (2017) 741-754.
[35] D. Sordelet, M. Akinc, Preparation of spherical, monosized Y_2O_3 precursor particles, J. Colloid Interface Sci., 122 (1988) 47-59.
[36] B. Aiken, W.P. Hsu, E. Matijević, Preparation and properties of monodispersed colloidal particles of lanthanide compounds: III, yttrium(III) and mixed yttrium(III)/cerium(III) systems, J. Am. Ceram. Soc., 71 (1988) 845-853.
[37] L. Hu, R. Ma, T.C. Ozawa, T. Sasaki, Synthesis of a solid solution series of layered $Eu_xGd_{1-x}(OH)_{2.5}Cl_{0.5} \cdot 0.9H_2O$ and its transformation into $(Eu_xGd_{1-x})_2O_3$ with enhanced photoluminescence properties, Inorg. Chem., 49 (2010) 2960-2968.
[38] L. Hu, R. Ma, T.C. Ozawa, F. Geng, N. Iyi, T. Sasaki, Oriented films of layered rare-earth hydroxide crystallites self-assembled at the hexane/water interface, Chem. Commun. , (2008) 4897-4899.
[39] Q. Zhu, J.-G. Li, C. Zhi, R. Ma, T. Sasaki, J.X. Xu, C.H. Liu, X.D. Li, X.D. Sun, Y. Sakka, Nanometer-thin layered hydroxide platelets of $(Y_{0.95}Eu_{0.05})_2(OH)_5NO_3 \cdot xH_2O$: exfoliation-free synthesis, self-assembly, and the derivation of dense oriented oxide films of high transparency and greatly enhanced luminescence, J. Mater. Chem. C, 21 (2011) 6903-6908.
[40] F. Geng, Y. Matsushita, R. Ma, H. Xin, M. Tanaka, F. Izumi, N. Iyi, T. Sasaki, General synthesis and structural evolution of a layered family of $Ln_8(OH)_{20}Cl_4 \cdot nH_2O$ (Ln = Nd, Sm,

Eu, Gd, Tb, Dy, Ho, Er, Tm, and Y), J. Am. Chem. Soc., 130 (2008) 16344-16350.
[41] X. Wu, J.-G. Li, Q. Zhu, W. Liu, J. Li, X. Li, X. Sun, Y. Sakka, One-step freezing temperature crystallization of layered rare-earth hydroxide ($Ln_2(OH)_5NO_3{\cdot}nH_2O$) nanosheets for a wide spectrum of Ln (Ln = Pr-Er, and Y), anion exchange with fluorine and sulfate, and microscopic coordination probed via photoluminescence, J. Mater. Chem. C, 3 (2015) 3428-3437.
[42] M. Machida, K. Kawamura, K. Ito, K. Ikeue, Large-capacity oxygen storage by lanthanide oxysulfate/oxysulfide systems, Chem. Mater., 17 (2005) 1487-1492.
[43] X. Wang, J.-G. Li, M.S. Molokeev, Q. Zhu, X. Li, X. Sun, Layered hydroxyl sulfate: Controlled crystallization, structure analysis, and green derivation of multi-color luminescent $(La,RE)_2O_2SO_4$ and $(La,RE)_2O_2S$ phosphors (RE = Pr, Sm, Eu, Tb, and Dy), Chem. Eng. J., 302 (2016) 577-586.
[44] L. Hu, R. Ma, T.C. Ozawa, T. Sasaki, Oriented monolayer film of Gd_2O_3:0.05Eu crystallites: quasi-topotactic transformation of the hydroxide film and drastic enhancement of photoluminescence properties, Angew. Chem. Int. Ed. , 48 (2009) 3846-3849.
[45] P. Scherrer, Estimation of the size and internal structure of colloidal particles by means of röntgen, Göttinger Nachrichten Math. Phys., 2 (1918) 96-100.
[46] J.-G. Li, X. Li, X. Sun, T. Ikegami, T. Ishigaki, Uniform colloidal spheres for $(Y_{1-x}Gd_x)_2O_3$ (x = 0–1): Formation mechanism, compositional impacts, and physicochemical properties of the oxides, Chem. Mater., 20 (2008) 2274-2281.
[47] T.P. Gompa, A. Ramanathan, N.T. Rice, H.S. La Pierre, The chemical and physical properties of tetravalent lanthanides: Pr, Nd, Tb, and Dy, Dalton. Trans., 49 (2020) 15945-15987.
[48] A.M. Srivastava, Aspects of Pr^{3+} luminescence in solids, J. Lumin., 169 (2016) 445-449.
[49] G. Blasse, G.J. Dirksen, Long-range energy transfer from Gd^{3+} to Pr^{3+}, J. Solid State Chem., 73 (1988) 599-602.
[50] Y. Sun, H. Zou, B. Zhang, X. Zhou, Y. Song, K. Zheng, Z. Shi, Y. Sheng, Luminescent properties and energy transfer of Gd^{3+}/Eu^{3+} co-doped cubic $CaCO_3$, J. Lumin., 178 (2016) 307-313.
[51] Y.-C. Li, Y.-H. Chang, Y.-S. Chang, Y.-J. Lin, C.-H. Laing, Luminescence and energy transfer properties of Gd^{3+} and Tb^{3+} in $LaAlGe_2O_7$, J. Phys. Chem. C, 111 (2007) 10682-10688.
[52] X. Wang, X. Wang, Z. Wang, Q. Zhu, G. Zhu, C. Wang, S. Xin, J.-G. Li, Photo/cathodoluminescence and stability of Gd_2O_2S:Tb,Pr green phosphor hexagons calcined from layered hydroxide sulfate, J. Am. Ceram. Soc., 101 (2018) 5477-5486.
[53] Y. Song, H. You, Y. Huang, M. Yang, Y. Zheng, L. Zhang, N. Guo, Highly uniform and monodisperse $Gd_2O_2S:Ln^{3+}$ (Ln = Eu, Tb) submicrospheres: Solvothermal synthesis and luminescence properties, Inorg. Chem., 49 (2010) 11499-11504.
[54] H. Yamada, A. Suzuki, Y. Uchida, M. Yoshida, H. Yamamoto, Y. Tsukuda, A scintillator Gd_2O_2S:Pr ,Ce ,F for X-ray computed tomography, J. Electrochem. Soc., 136 (1989) 2713-2716.
[55] X. Wang, J.-G. Li, Q. Zhu, X. Li, X. Sun, Y. Sakka, Facile and green synthesis of $(La_{0.95}Eu_{0.05})_2O_2S$ red phosphors with sulfate-ion pillared layered hydroxides as a new type of precursor: controlled hydrothermal processing, phase evolution and photoluminescence, Sci.

Technol. Adv. Mater., 15 (2014) 014204.
[56] X. Wang, Q. Meng, M. Li, X. Wang, Z. Wang, Q. Zhu, J.-G. Li, A low temperature approach for photo/cathodoluminescent Gd_2O_2S:Tb (GOS:Tb) nanophosphors, J. Am. Ceram. Soc., 102 (2019) 3296-3306.
[57] G. Blasse, G.J. Dirksen, F. Zonnevijlle, The luminescence of some lanthanide decatung-states and other polytungstates, J. Inorg. Nucl. Chem., 43 (1981) 2847-2853.
[58] G. Blasse, Energy transfer between inequivalent Eu^{2+} ions, J. Solid State Chem., 62 (1986) 207-211.
[59] R.N. Wenzel, Resistance of solid surfaces to wetting by water, Ind. Eng. Chem., 28 (1936) 988-994.
[60] A.B.D. Cassie, S. Baxter, Wettability of porous surfaces, Trans. Faraday Soc., 40 (1944) 546-551.

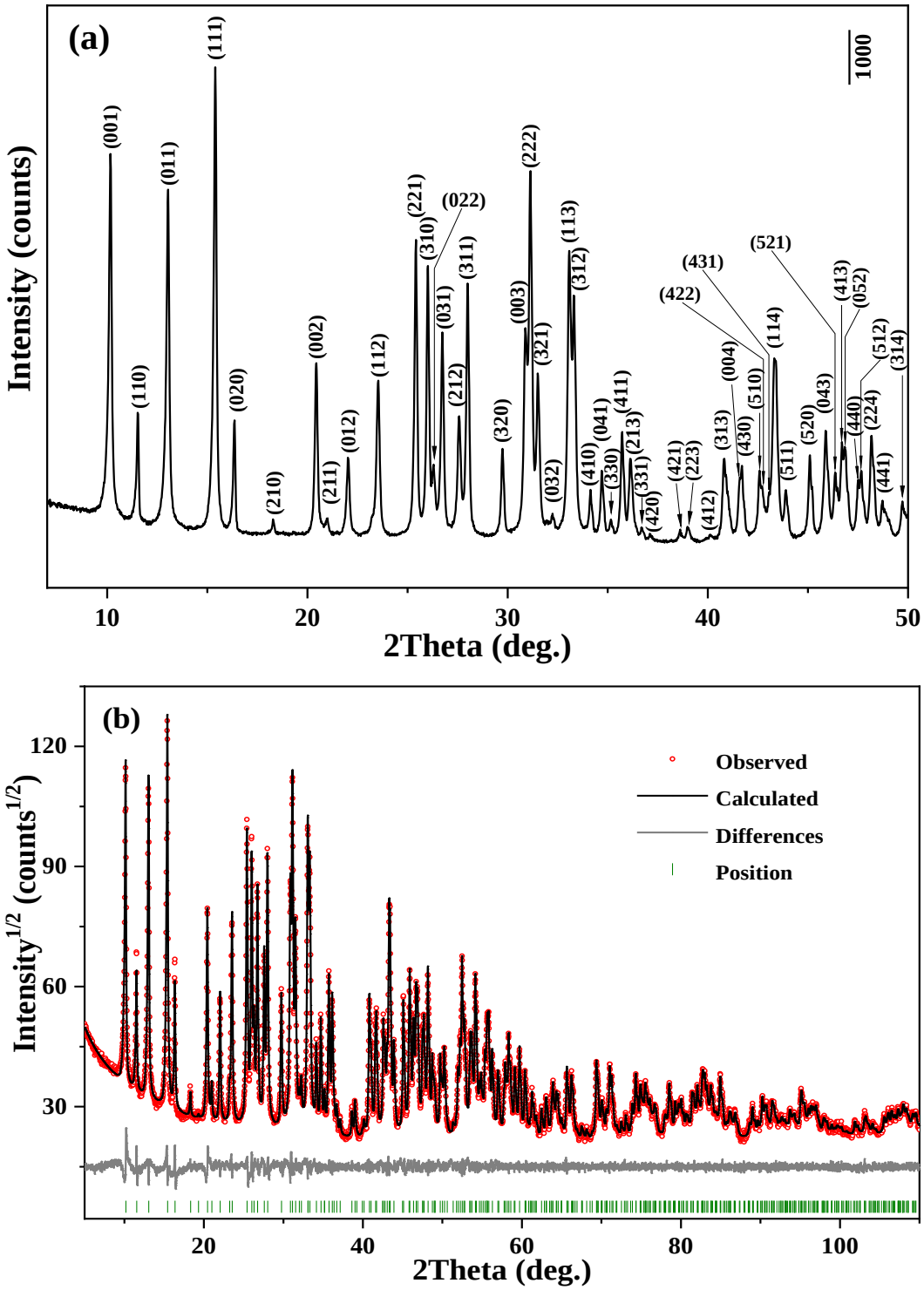

Fig. 1. Indexation of the XRD pattern of precursor powder for 2θ = 5-50° (a) and the results of Pawley refinement of the XRD pattern (b).

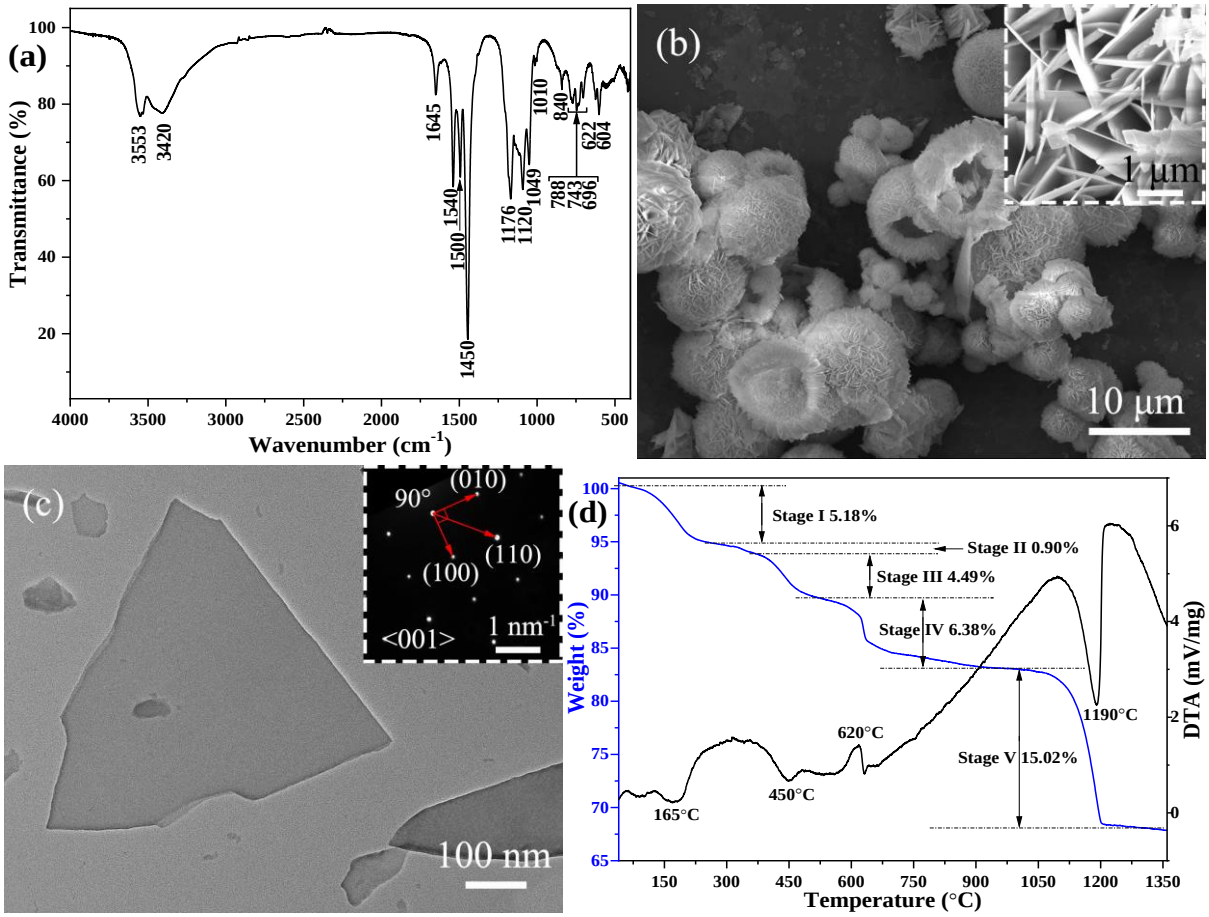

Fig. 2. FTIR spectrum (a), FE-SEM morphology (b), TEM morphology (c) and TG/DTA curves (d) of the precursor powder. The inset in (b) is a closer view and that in (c) is the SAED pattern.

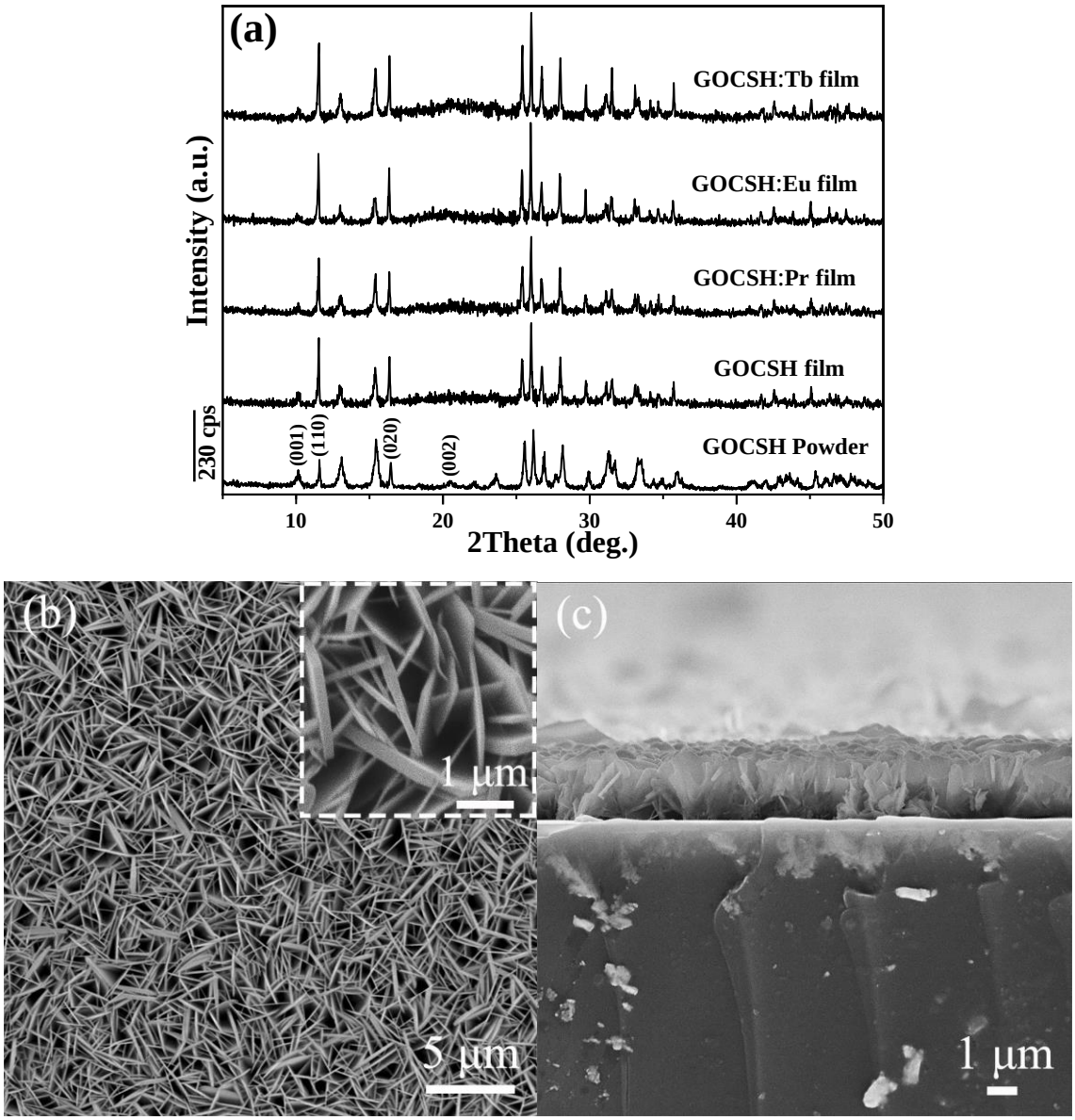

Fig. 3. XRD patterns of the precursor films deposited at 110 °C, with that of the GOCSH powder included for comparison (a), and FE-SEM morphologies of the GOCSH film observed from the surface (b) and cross section (c). The inset in (b) is a closer view.

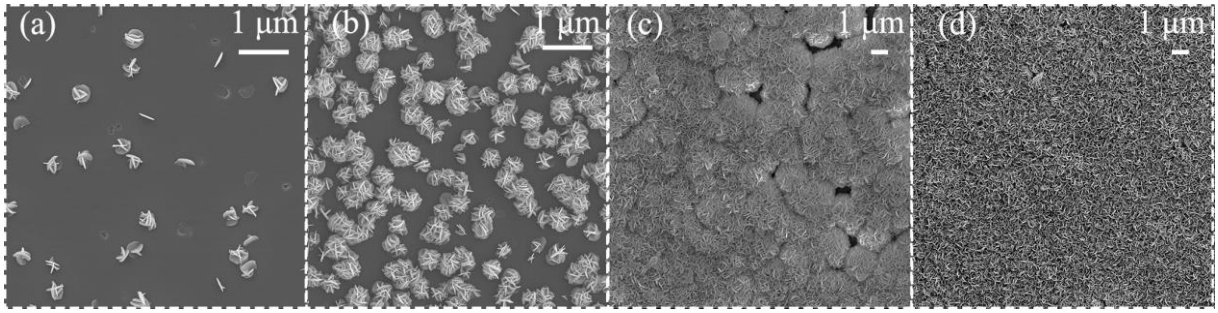

Fig. 4. FE-SEM morphologies of the GOCSH films after deposition at 110 °C for 30 min (a), 60 min (b), 90 min (c) and 120 min (d).

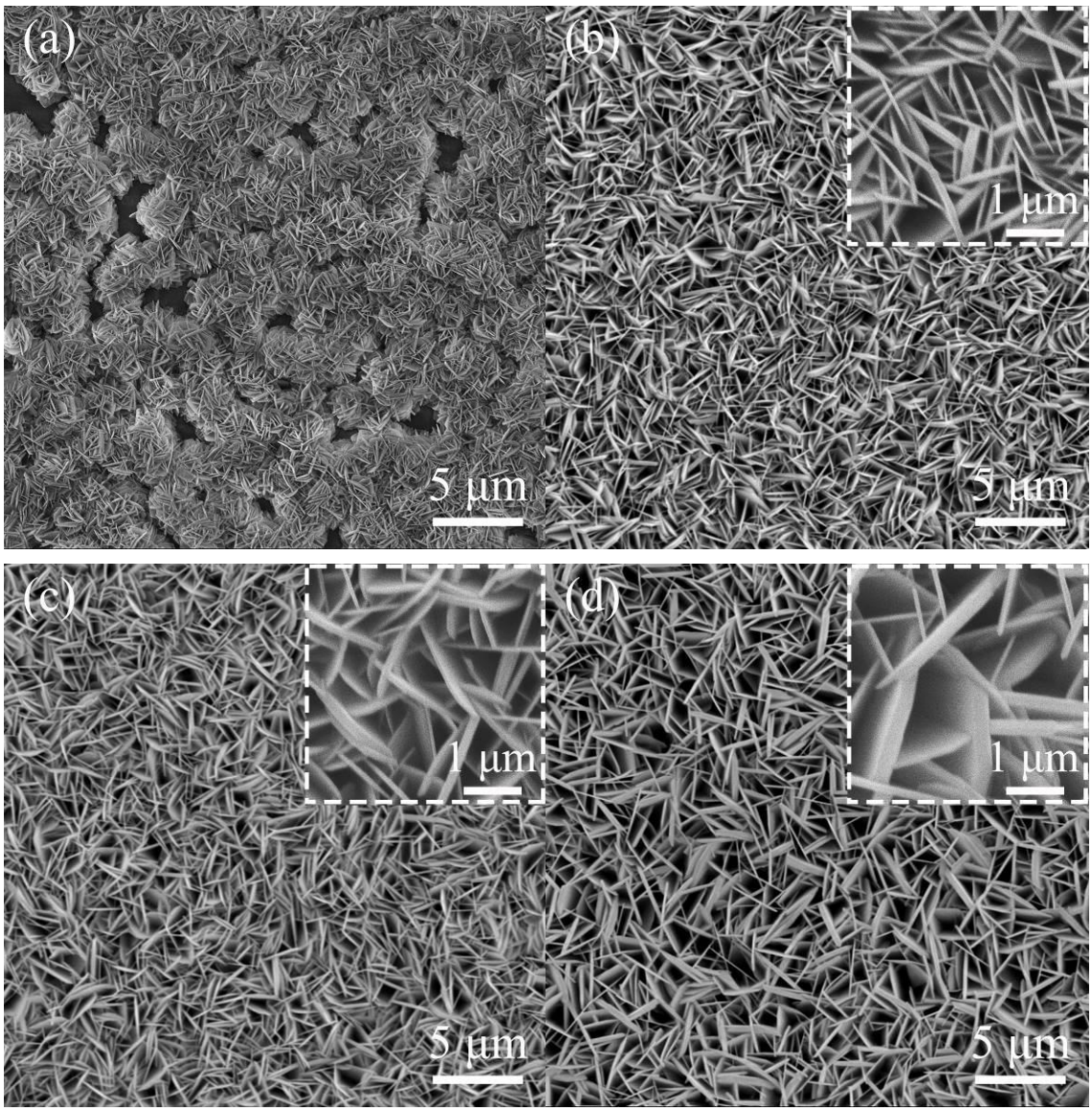

Fig. 5. FE-SEM morphologies of the GOCSH films prepared at 100 ℃ (a), 120 ℃ (b), 130 ℃ (c) and 140 ℃ (d). The insets in (b), (c) and (d) are closer views.

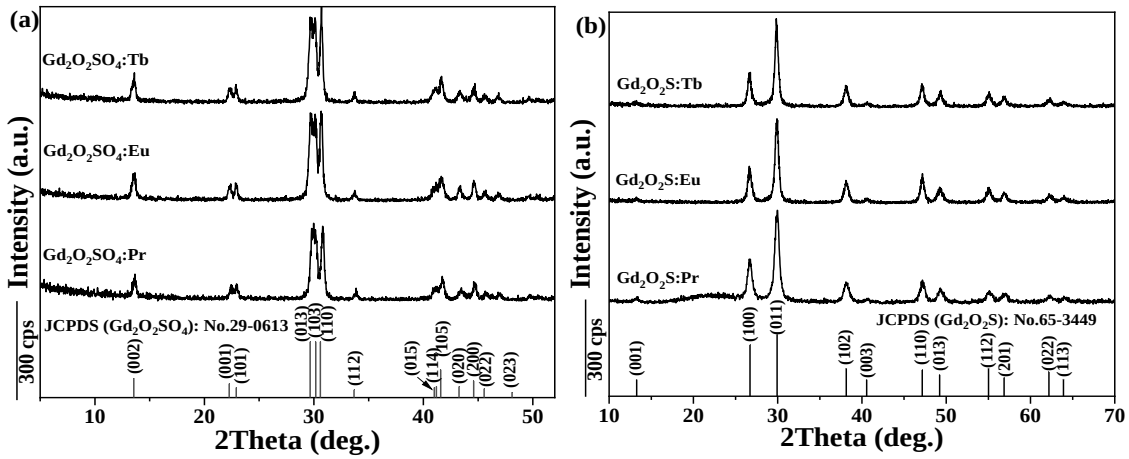

Fig. 6. XRD patterns of the products obtained by annealing the GOCSH:Ln films at 800 ℃ in air (part a) and in H_2 (part b).

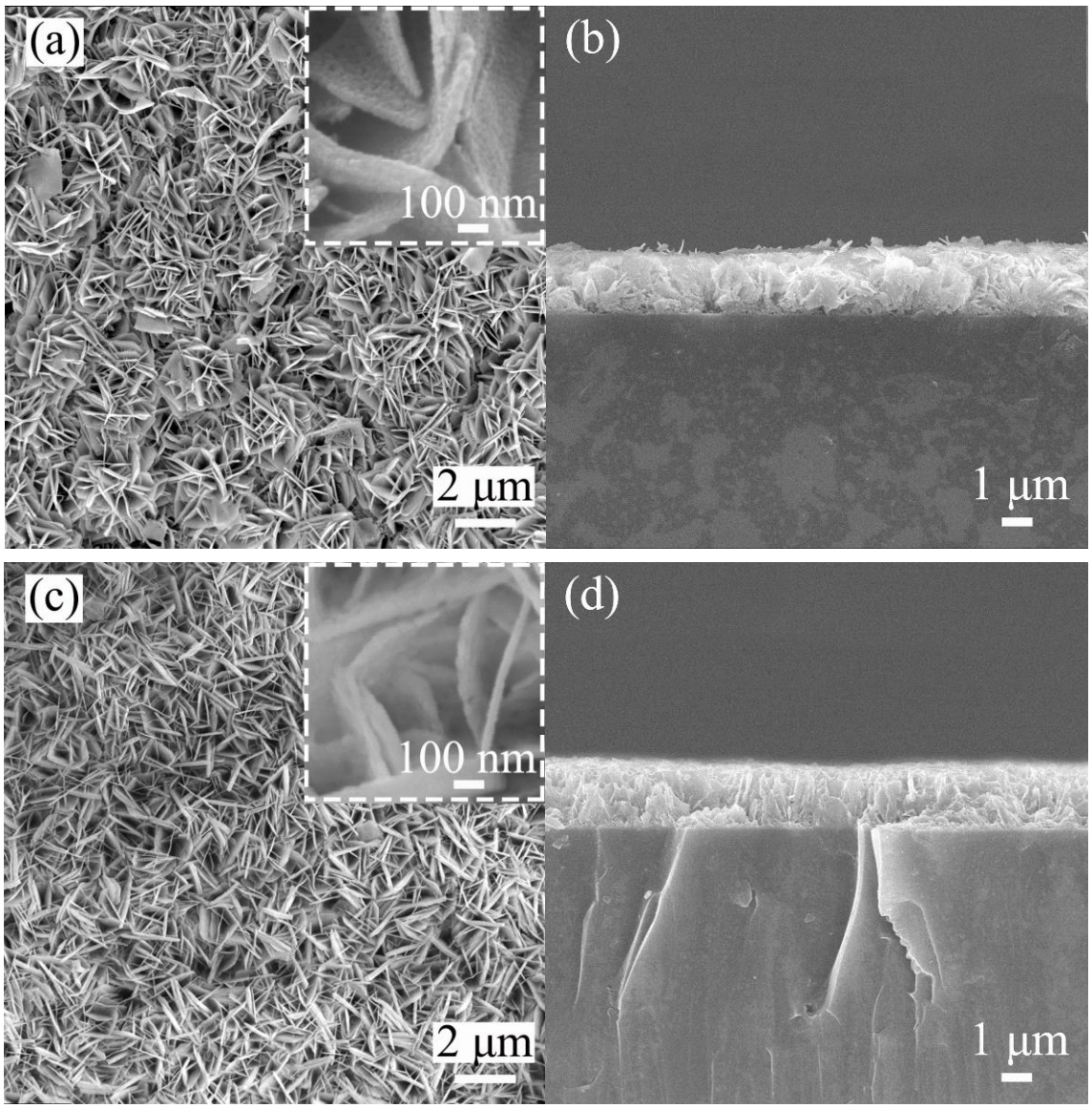

Fig. 7. FE-SEM morphologies of the 800 °C annealed $Gd_2O_2SO_4$:Eu (a, b) and Gd_2O_2S:Pr (c, d) films, where the insets in (a) and (c) are closer views.

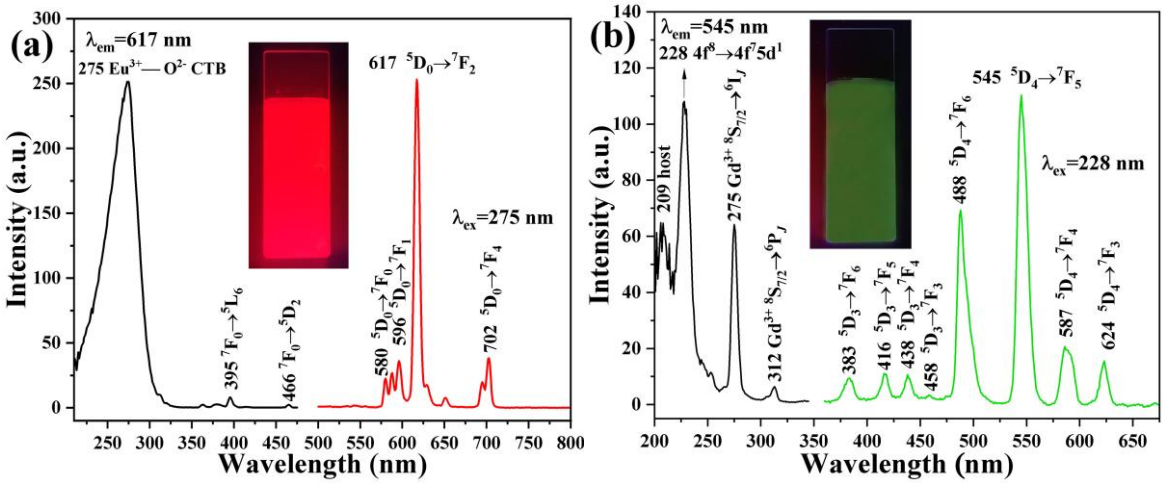

Fig. 8. PLE (left) and PL (right) spectra of the $Gd_2O_2SO_4$:Eu (a) and $Gd_2O_2SO_4$:Tb (b) films. The insets are digital photographs taken for the appearance of luminescence under 254 nm UV irradiation.

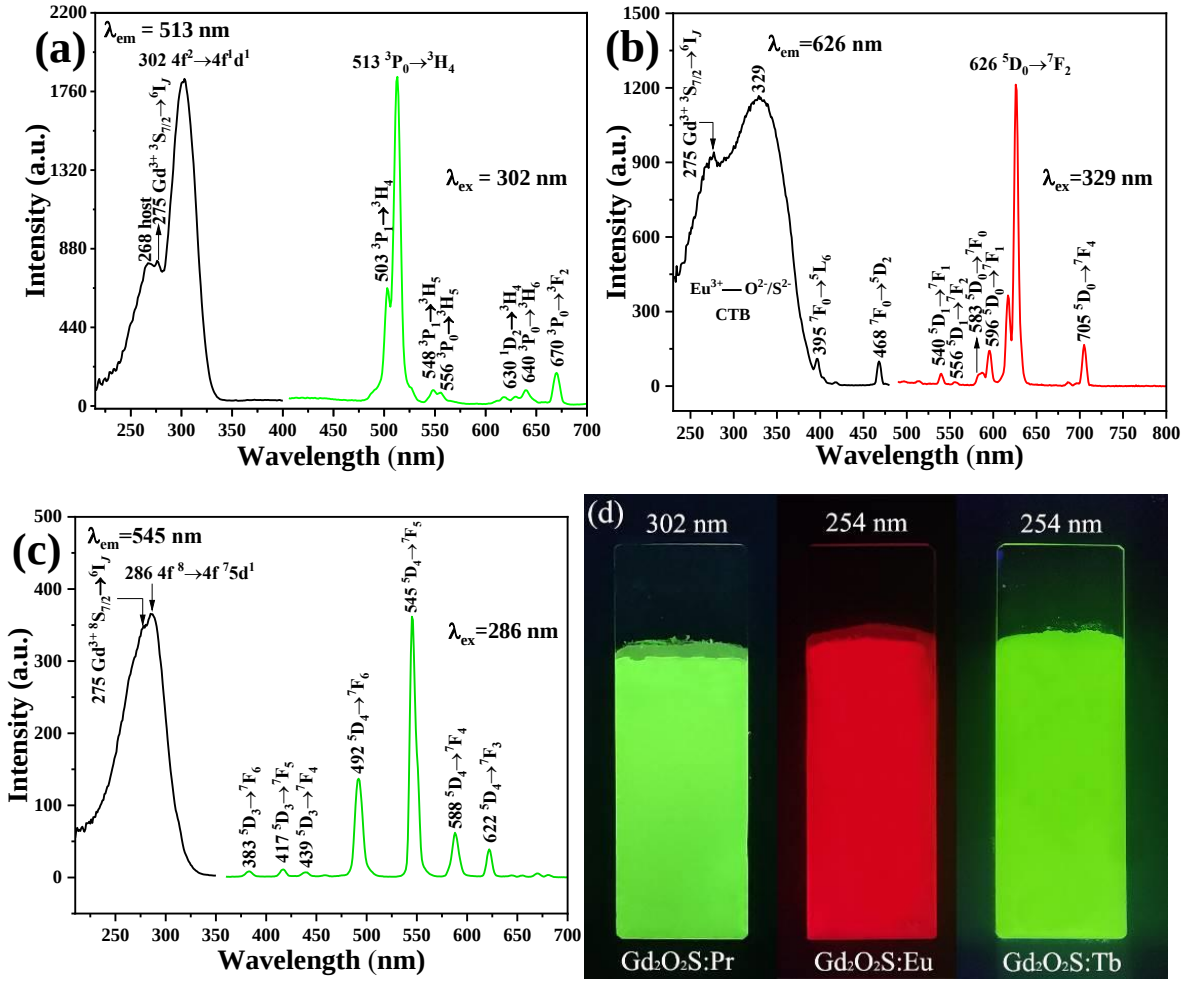

Fig. 9. PLE (left) and PL (right) spectra of the Gd_2O_2S:Pr (a), Gd_2O_2S:Eu (b) and Gd_2O_2S:Tb (c) films. Part (d) is a digital photograph showing the appearance of film luminescence under UV irradiation.

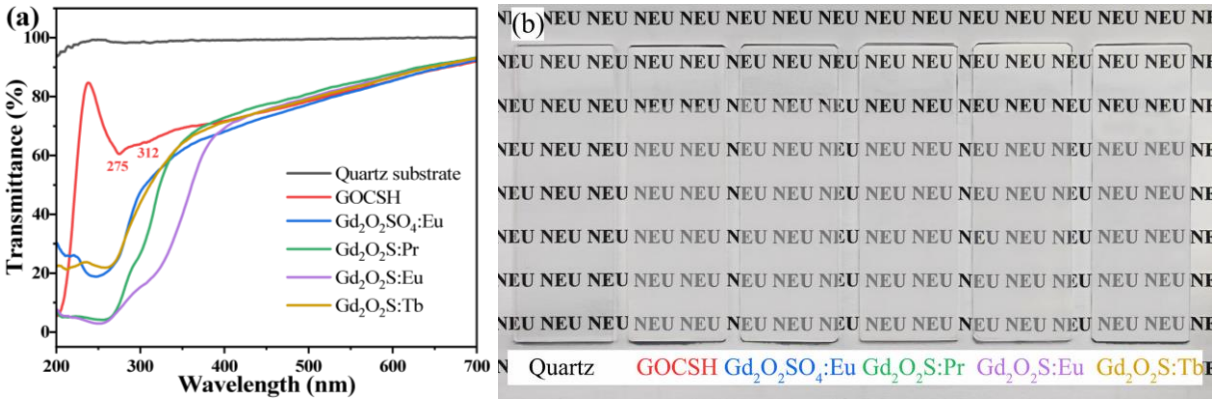

Fig. 10. Transmittance spectra of the typical films and bare quartz (a) and a photograph showing the appearance of light transmission (b).

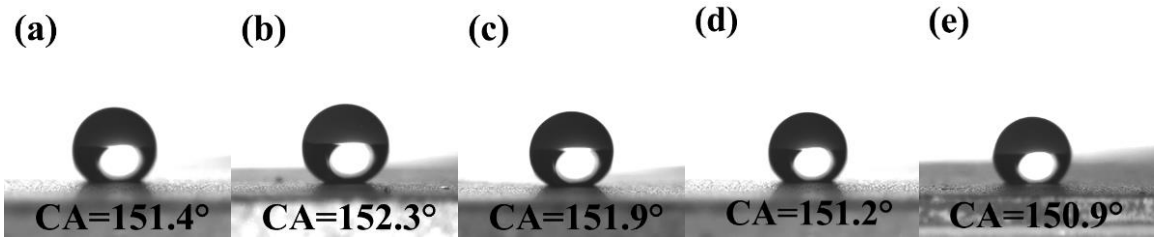

Fig. 11. Water wettability test of the films, with parts (a)-(e) for GOCSH, $Gd_2O_2SO_4$:Eu, Gd_2O_2S:Pr, Gd_2O_2S:Eu and Gd_2O_2S:Tb, respectively.

ORCID Information

Fan Li https://orcid.org/0000-0001-6779-6179

Minghui Jin https://orcid.org/0000-0003-2446-9332

Zhuowei Li https://orcid.org/0000-0003-2374-112X

Xuejiao Wang https://orcid.org/0000-0003-4327-2340

Qi Zhu https://orcid.org/0000-0001-5513-6309

Ji-Guang Li https://orcid.org/0000-0002-5625-7361

CRediT author statement

Fan Li: Formal analysis, Data curation, Writing-original draft. **Minghui Jin:** Data curation. **Zhuowei Li:** Data curation. **Xuejiao Wang:** Formal analysis. **Qi Zhu:** Resources, Supervision. **Ji-Guang Li:** Conceptualization, Supervision, Validation, Writing-review & editing.

Declaration of interests

☒The authors declare that they have no known competing financial interests or personal relationships that could have appeared to influence the work reported in this paper.

☐The authors declare the following financial interests/personal relationships which may be considered as potential competing interests: